学位論文

Ultrafast spin dynamics induced by pulsed terahertz wave in canted antiferromagnet

(傾角反強磁性体におけるテラヘルツ波パルス誘起超高速スピンダイナミクスの研究)

平成 25 年 12 月博士（理学）
申請

東京大学大学院理学系研究科
物理学専攻

山口 啓太

Abstract

Exploitation of the spin degree of freedom is one of the topics that are currently drawing intense attention. Recent development of femtosecond laser has provided a means to excite spin systems in an ultrafast timescale. Not only it is of interest in applicative sense such as ultrafast spintronics device and optical memory, the ultrafast dynamics of the spin system itself is one of the many interesting topics that are yet to be fully explored. In this thesis, ultrafast spin dynamics excited by the magnetic field component of pulsed terahertz waves is studied. This thesis focuses on the ultrafast spin dynamics in orthoferrite $RFeO_3$ which is a canted antiferromagnet where antisymmetrically ordered iron ion spins are slightly canted, giving rise to a small ferromagnetic moment. Orthoferrites are known to possess two antiferromagnetic resonance modes in the sub-THz region, namely F mode and AF mode resonance, and the dynamics of these two resonance modes were observed.

Transmission type terahertz time domain spectroscopy (THz-TDS) experiment with orthoferrite $YFeO_3$ confirmed that the two antiferromagnetic resonances can be accessed with the magnetic field component of the THz pulse. The precessing motion of the spins were observed through magnetic dipole emission which is also known as free induction decay (FID) signals. Double pulse THz excitation was tested and it was verified that coherent control of spin precession can be performed with the THz pulse. At the same time, energy transfer between the THz photon system and the spin system was directly observed.

Using the samples $ErFeO_3$ and $DyFeO_3$ that are known to show spin reorientation phase transitions where the equilibrium orientation of the iron ion spins rotates 90 degree were observed with THz-TDS experiment. It was shown that spin configuration can be determined from the result of THz-TDS, and this is applicable for detection of ultrafast spin reorientation. To demonstrate this, visible pump- THz pulse probe experiment was conducted. As a result, ultrafast heating of the rare-earth $4f$ electron temperature was observed through gradual change of the magnetic resonant frequencies.

High electric and magnetic field amplitude THz pulse of about 400 kV/cm and 0.13 T generated from $LiNbO_3$ was used to pump the Fe^{3+} spin precession in $ErFeO_3$ and $DyFeO_3$. They were monitored with Faraday rotation of visible probe pulses. In $DyFeO_3$ a result which suggests reorientation temperature shift due to the THz magnetic field was obtained. The result obtained from $ErFeO_3$ showed splitting of the F mode resonance which, to the best of the author's knowledge, has never been reported up until now. A theoretical model where Dzyaloshinskii-Moriya interaction plays an important role is proposed. The proposed mechanism was confirmed to reproduce the experimental result reasonably well. Other peculiar phenomena which seems to be the strong excitation effects are also introduced.

Contents

Chapter1

Introduction

Terahertz (THz) wave is an electromagnetic wave with its oscillation frequency ranging from 0.1 to 10 THz. This frequency range corresponds to the intermediate region of the light and the radio wave, also known as the far infrared ray or the submillimeter wave [1]. This region contains numbers of interesting and characteristic excitations such as free carrier absorption in semiconductors, phonon, superconductivity gap, rotational level of gas molecules, and soft mode of dielectrics. However, historically, researches in the THz region have been delayed mainly due to the lack of efficient generation and detection techniques. The development of a stable femtosecond laser has enabled pulsed THz wave generation with the photoconductive antennas [2] and triggered intensive researches on THz spectroscopy and imaging.

An example of a pulsed THz wave, hereafter referred to as a THz pulse, used for the THz time domain spectroscopy (TDS) is shown in Fig. 1.1. The temporal waveform of the THz electric field component shows that the THz pulse can be observed as picosecond order single cycle electromagnetic transient (1.1(a)). As the Fourier spectrum of the THz pulse (Fig. 1.1(b)) describes, THz pulse is composed of electromagnetic waves with a broad range of frequency, typically up to several THz.

THz-TDS is a very useful tool for investigating various materials. Unlike the ordinary spectroscopic methods in the optical region where the intensity of the electromagnetic waves is measured, THz-TDS measures the amplitude and the phase of the electromagnetic waves at the same time. Therefore, information such as complex permittivity, complex refractive index, and complex conductivity can be obtained through direct computation without de-

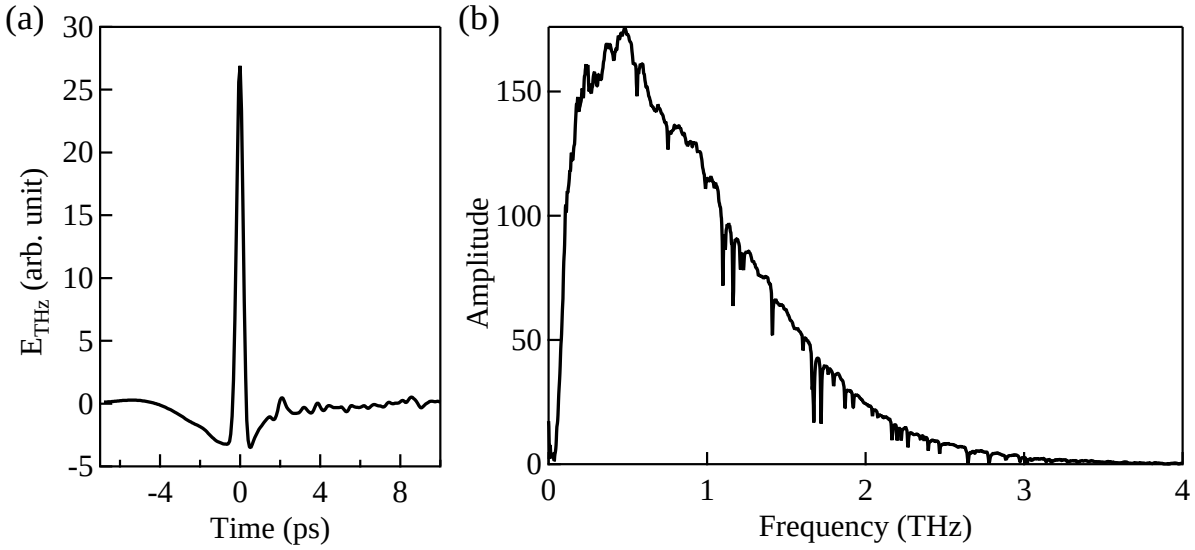

FIG. 1.1 (a)Temporal waveform of pulsed THz wave generated from photoconductive antenna. (b) Fourier spectrum of the temporal wave form in (a).

pending on Kramers-Kronig Transformation. Moreover, owing to the very short pulse width (less than 1 ps), THz-TDS method enables observation of ultrafast dynamics of excited phenomena with femtosecond-order time resolution. In addition, recent developments on intense THz pulse generation methods such as tilted pulse front phase matching in $LiNbO_3$, and THz generation from two-color pulse excited air plasma have realized THz pulses with their electric field strength up to 1 MV/cm [3–9]. Such high intensity THz pulse can cause nonlinear effects in materials such as semiconductors and thus, opened a new field of research concerning on excitation and manipulation of materials with THz pulses [10].

For a long time, majority of the researches using optical pulses and THz waves have concentrated strictly on the ”electric” interaction with materials and the magnetic field components of the electromagnetic waves have been neglected. However, magnetic field component of THz pulses has a potential to directly manipulate spin systems in ultrafast time scale. In this thesis, excitation and manipulation of materials with the magnetic field component of THz pulses are studied.

The following chapters are presented as follows. Chapter 2 introduces the general backgrounds of this thesis: concept of ultrafast spin excitations and properties of the rare-earth orthoferrites, the samples used in this research. After that, the purpose of this research is

summarized. Chapter 3 is devoted to the explanation of the experimental methods. Chapters 4, 5, and 6 will describe the results obtained from the experiments. Chapter 4 focuses on the experimental results obtained from room temperature experiment conducted on $YFeO_3$. Both the results from single pulse THz excitation and double pulse excited coherent control of spin precession are presented. Chapter 5 is on the experiment performed with $ErFeO_3$ and $DyFeO_3$ that are known to show temperature induced spin reorientation transition. A novel method for detecting the reorientation is introduced. The result of visible laser pump-THz pulse probe experiment on these samples are also described. Chapter 6 focuses on spin dynamics induced by high intensity THz pulse. Several new phenomena that were not observed in the past experiments are introduced. Lastly, chapter 7 summarizes the result of this research.

Chapter2

Background

In this chapter, the background informations on ultrafast excitation of the electron spin system is introduced. Then, the effect of the THz pulses on the ordered spin systems, and means of detecting such ultrafast spin dynamics are described. In the section after that, details on the orthoferrite $RFeO_3$ (R: rare-earth), the sample used in this research, are introduced. In the third section, the purpose of this research is summarized.

2.1 Ultrafast Excitation of the Spin System

2.1.1 Ultrafast Excitation of the Spins with Visible Laser

Developments on methods for exploiting the spin degrees of freedom are currently receiving intense attention and various approaches are being made. These research field known as spintronics generally aims to control the electron spins by means of the electronic methods such as spin-polarized current injections. Motivated by the rapid progress in the femtosecond laser spectroscopy, completely different method for manipulating the spin systems, namely, ultrafast optical excitation of the spin systems, has been developed and number of studies have been made. Because ultrafast optical control of spins can manipulate spin systems within subpicosecond timescale, this technique is highly promising for realization of unprecedentedly fast optical memory, spintronics, and quantum computing.

One typical example of optical spin excitation is optical spin injection into semiconductors, where the angular momentum of the circularly polarized light is passed on to the photoexcited carriers and their spins are aligned. Study on this subject dates back to the research reported

by Lampel [11] in 1968 which succeeded in observing the production of polarized electron spins in silicon by circularly polarized light. After this report, number of researches on optical injection of spins were conducted on samples such as bulk semiconductors, heterostructures, and quantum dots [12].

Recently, ultrafast optical spin excitation in strongly magnetic substances such as ferromagnets and antiferromagnets are receiving intense attention. One example of this is the experiment performed by Kimel *et al.* [13], which is shown in Fig. 2.1. In this example, circularly polarized visible laser is used for inducing transient magnetization along the direction of propagation via effect known as the inverse Faraday effect [14]. The figure shows that the magnetization caused by the inverse Faraday effect induces coherent precessional motion of Fe^{3+} spins which can be observed as oscillation in Faraday rotation angle of visible probe laser. By changing the helicity of the circularly polarized laser, precession with opposite phase is induced. The significance of the inverse Faraday effect is that it transfers angular momentum of the light pulses to the electron spins through Raman process without involving photoexcited carriers. With a combination with spatial pulse shaping, inverse Faraday effect can also be applied to control the spin wave emission [15]. However, although real electronic excitations do not take place, this effect is mediated by excited states of electrons through perturbation caused by the visible laser. Thus, inverse Faraday effect occurs as a result of a dielectric interaction between the light and the matter.

Majority of other reports on demonstrations of ultrafast optical control of spin systems in magnets also use indirect excitations of the spins that occur as a result of dielectric interaction with optical pulses such as electronic excitations [16–18], inverse Faraday effect [19–26], inverse Cotton-Mouton effect [22–24], magnetic difference frequency generations [27, 28], optical Stark effect [29], and thermal excitations [20, 21, 26, 30]. Since the spins are excited through indirect process, their efficiency is not high and most of the optical energy is not transferred to the spin system. In addition, detection method of the spin dynamics in most cases, namely Faraday rotation or magneto-optical Kerr rotation, are also indirect and monitors the spins through fluctuation of dielectric constants. While these detection methods are very useful for studying ultrafast spin dynamics, when these techniques are used for realization of applicative devices, the extra perturbation on the spins and the extra unwanted heat

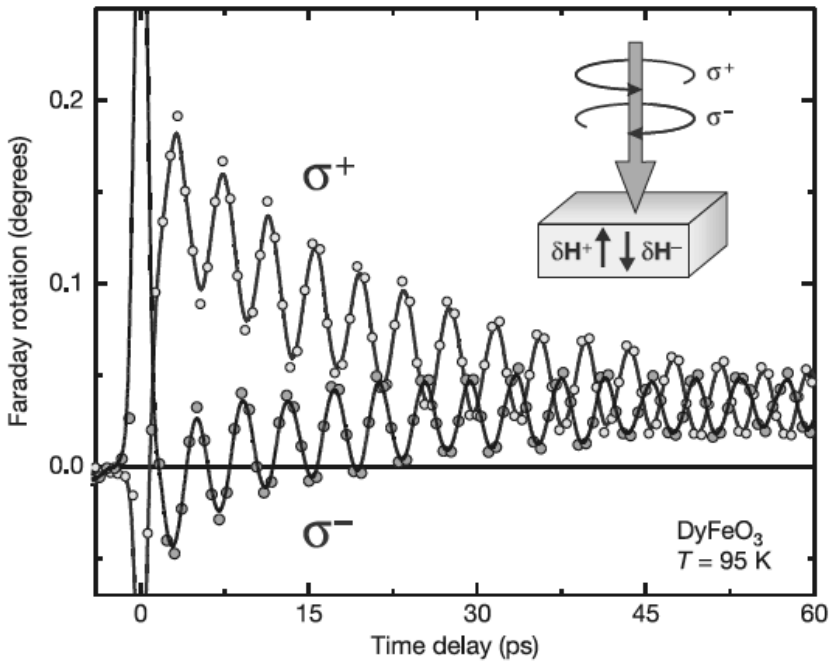

FIG. 2.1 Ultrafast optical excitation of spins in $DyFeO_3$ with the inverse Faraday effect [13].

generation may become a problem. The reason these researches rely on indirect excitation of spins is because the the visible pulse laser cannot couple directly to the resonance of the spins. This mismatch of the energy makes it impossible for the magnetic field component of the light pulses to interact directly with the spins.

THz pulses, on the other hand, have photon energy equivalent to that of the spin resonance, which means that THz pulses are ideal for direct ultrafast excitation of spin systems. In addition to its efficiency, direct excitation of the spins with the THz waves do not require existence of any electronic excitations. This ability enables an unique advantage of realizing excitation of spin system in ultrafast timescale without causing any other unwanted excitations such as electronic excitations. Not only this phenomenon is interesting in physical point of view, this is also advantageous for applications such as ultrafast memory device whose major reason for the limit of the operation speed is expected to be generation of unwanted heat.

Prior to this study, ultrafast spin excitation with THz pulses was demonstrated with ferromagnetic resonance in ε-iron oxide nanoferromagnets [31]. Although this particular ferro-

magnet has very high resonant frequency of about 0.1 THz, ferromagnets commonly have low resonant frequency compared to that of antiferromagnets. This is because the antiferromagnetic resonant frequency ω is proportional to $\sqrt{H_A H_{ex}}$, where H_A is the anisotropy field and H_{ex} is the effective exchange magnetic field, whereas the ferromagnetic resonant frequency is proportional to the effective anisotropy field H_A applied to the spins. Since in most materials, H_A is smaller than 1T and H_{ex} is about 100 T [30], resonant frequency of antiferromagnets become larger, typically up to 1 THz.

One of the approaches that can be taken for realization of ultrafast magnetic devices is to utilize the magnetic resonance (precession motion) of the spins. Therefore, in an applicative point of view, materials with high resonant frequencies are more suitable. Also, owing to the recent progress of millimeter and THz wave technologies, demands on materials that can be used as wave absorbers required for millimeter wireless communications are high [32]. In addition, ultrafast spin dynamics in antiferromagnets are intriguing subject in a physical point of view.

This thesis focuses on the ultrafast spin excitation dynamics on antiferromagnets with THz pulses, which, to the best of the author's knowledge, has not been reported before starting this research. The remainder of this section is devoted to the basic idea of THz induced ultrafast spin excitation and the detection method of such ultrafast dynamics.

2.1.2 Ultrafast Excitation of Spin System with THz Pulse

Here, interaction between the THz pulse and the spins is discussed. The interaction between the THz electric field component and the spins is expected to be negligibly small compared to the direct interaction between the magnetic field component and the spins. Therefore, the incident THz pulse can be treated as external magnetic field applied to the spins.

The magnetic momentum of an electron with angular momentum $\boldsymbol{S}$ is given by

$$\boldsymbol{M} = -\gamma \boldsymbol{S} \tag{2.1}$$

where γ is the gyromagnetic constant of spin. The gyromagnetic constant of an isolated electron spin is $\gamma = 1.76 \times 10^{11}$ rad $\mathrm{T}^{-1}\mathrm{s}^{-1}$. When magnetic field $\boldsymbol{H}$ is applied to a spin, torque $\boldsymbol{T} = \boldsymbol{M} \times \boldsymbol{H}$ is exerted to the spin. Using the relation $d\boldsymbol{S}/dt = \boldsymbol{T}$ and equation (2.1),

the equation of motion for the electron spin magnetic momentum

$$\frac{d\boldsymbol{M}}{dt} = -\gamma \boldsymbol{M} \times \boldsymbol{H} \tag{2.2}$$

is obtained. When considering spins in a strongly magnetic substances, that is ferromagnet or antiferromagnet, not only external magnetic field but also effective magnetic field due to effects such as exchange interaction and magnetic anisotropy constitutes the magnetic field $\boldsymbol{H}$ in equation (2.2). In the actual experiments, damping of the motion of the magnetic momentum must also be taken in to account. For this purpose, instead of eq. (2.2), Landau-Lifshitz-Gilbert equation

$$\frac{d\boldsymbol{M}}{dt} = -\gamma \boldsymbol{M} \times \boldsymbol{H} + \eta\gamma \boldsymbol{M} \times \frac{d\boldsymbol{M}}{dt} \tag{2.3}$$

is used. The damping parameter η is often replaced with $\eta = \alpha/M\gamma$ where α and M represents the dimensionless damping parameter and the magnitude of the magnetic momentum, respectively [33].

Using the equation (2.3), we will see how the magnetic moment reacts to the THz magnetic field component. Presupposing that the effective magnetic field

$$\boldsymbol{H_{effective}} = \begin{pmatrix} 0 \\ 0 \\ H_0 \end{pmatrix}, \tag{2.4}$$

and the THz magnetic field

$$\boldsymbol{H_{THz}} = \begin{pmatrix} H_{THz}(t) \\ 0 \\ 0 \end{pmatrix}, \tag{2.5}$$

eq. (2.2) can be transformed into

$$\frac{dM_x}{dt} = -\frac{\omega_0}{1+\alpha^2} M_y - \frac{\alpha\omega_0}{M(1+\alpha^2)} M_x M_z + \frac{\alpha\omega_x}{M(1+\alpha^2)} (M_y^2 + M_z^2), \tag{2.6}$$

$$\frac{dM_y}{dt} = \frac{\omega_0}{1+\alpha^2} M_x + \frac{\omega_x}{1+\alpha^2} M_z - \frac{\alpha\omega_0}{M(1+\alpha^2)} M_y M_z - \frac{\alpha\omega_x}{M(1+\alpha^2)} M_x M_y, \tag{2.7}$$

$$\frac{dM_z}{dt} = -\frac{\omega_x}{1+\alpha^2} M_y - \frac{\alpha\omega_0}{M(1+\alpha^2)} (M_x^2 + M_y^2) - \frac{\alpha\omega_x}{M(1+\alpha^2)} M_x M_z. \tag{2.8}$$

Here, $\omega_0 = \gamma H_0$, and $\omega_x = \gamma H_{THz}$.

For calculating the motion of the magnetic moment, the fitted curve of the waveform in Fig. 1.1 (a) with a pair of gaussian functions $A_1 \exp(-\frac{(t-t_1)^2}{\Delta t_1^2}) - A_2 \exp(-\frac{(t-t_2)^2}{\Delta t_2^2})$ was used as the incident THz pulse. The result of the fitting is shown in Fig. 2.2(a). The values of

each fitting parameters were as follows: $A_1 = 9.2A_2$, $\Delta t_1 = 0.226$ ps, $\Delta t_2 = 1.9$ ps, and $t_1 - t_2 = 0.42$ ps. The integrated values of each gaussians are roughly identical (20.7 for the first gaussian pulse and 19 for the second gaussian). This is consistent with the fact that integration of any propagating electromagnetic waves must become zero.

The calculated motion of the normalized magnetic moment with its initial condition

$$\boldsymbol{M}(0) = \begin{pmatrix} 0 \\ 0 \\ 1 \end{pmatrix} \tag{2.9}$$

is shown in Fig. 2.2(b). The magnitude of the effective magnetic field H_0 was selected so that $\omega_0 = 1$ THz. The value of the damping constant used here is $\alpha = 0.02$. As Fig. 2.2(b) describes, THz magnetic field is expected to excite damped oscillation in x axis and y axis components of the magnetic moment. Because the phase of the oscillations in the x and y direction differ by $\pi/2$, as a whole, the magnetic moment exhibits circular motion inside x-y plane. These oscillations can be fitted with $\cos(\phi+\omega t)\exp(-t/\tau)$ and since $\omega = 1$ THz $(= \omega_0)$ and $\tau = 7.9$ ps $(= 1/\alpha\omega_0)$ reproduce this motion very well, this excited motion corresponds to precession motion of the spins caused by the magnetic resonance which originates from the effective magnetic field. Looking at the magnetization dynamics in z axis direction, we notice that introduction of the THz magnetic field results in sudden decrease of the magnetization in this direction which relaxes after several picosecond. Considering all these results together, we can see that in the framework of the Landau-Lifshitz-Gilbert equation, the magnetic field component of the THz pulse instantaneously tilts the spins out of its equilibrium orientation (Fig.2.3). After the occurrence of this tipping, the tilted spins start to precess around the effective magnetic field.

At first glance, this result may seem inconsistent because the integrated value of the THz magnetic pulse is zero. As previously mentioned, the THz magnetic pulse used here can be separated into a pair of half cycle gaussian pulses. Figure 2.4 shows how each half cycle pulses affect the motion of M_x. From this figure, it can be observed that the half cycle pulse 1 (pulse with larger amplitude and shorter temporal width) causes most of the oscillation observed in Fig. 2.2. On the other hand, the contribution of the half cycle pulse 2 with smaller amplitude and broader width is negligibly small. Therefore, the THz magnetic field is expected to work effectively as a half cycle pulse and this is the reason why single cycle THz

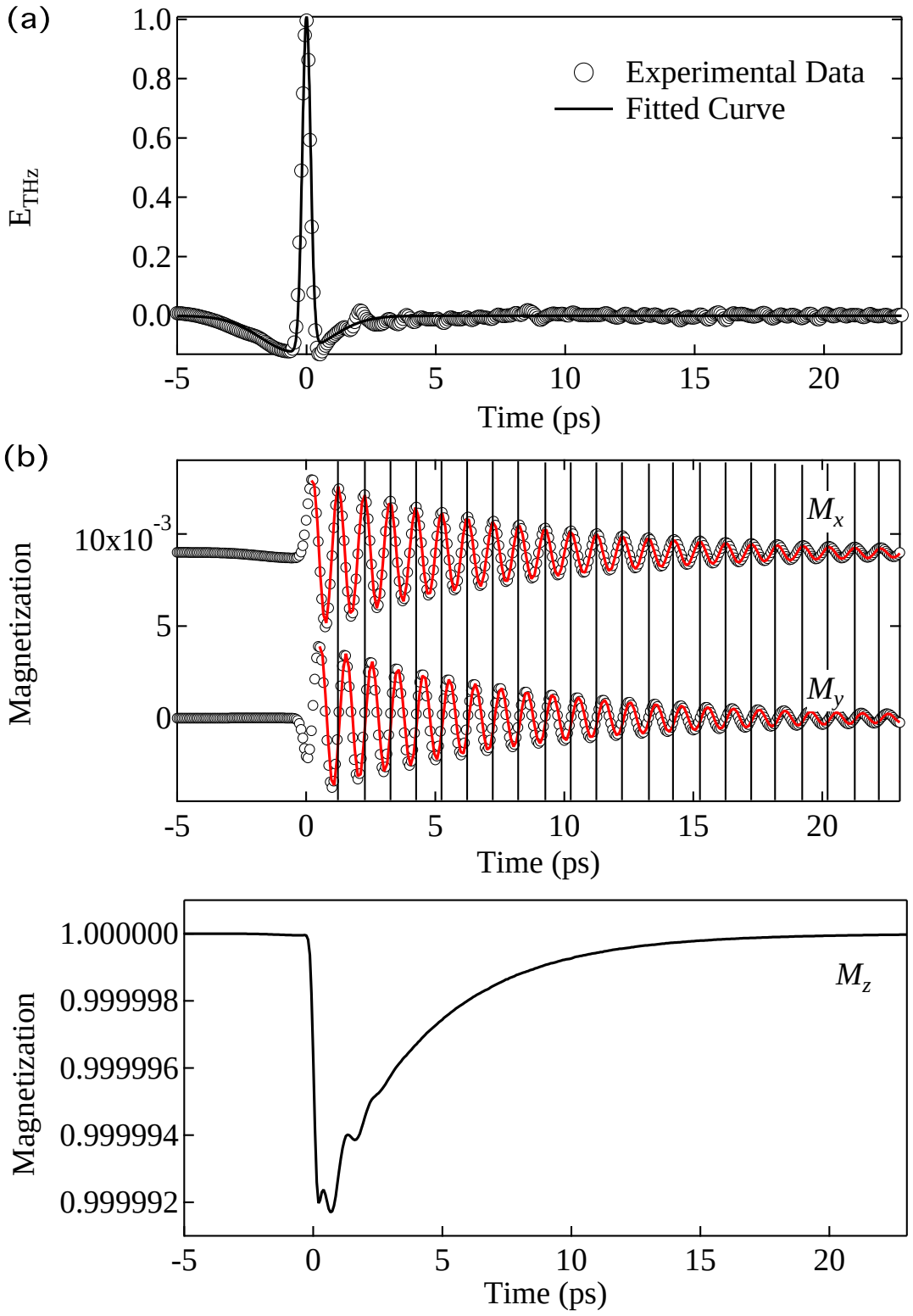

FIG. 2.2 The calculated magnetization dynamics obtained from the Landau-Lifshitz-Gilbert equation. (a) Incident THz pulse used for the calculation. (b) Magnetization dynamics calculated from the LLG equation for the x axis component and the y axis component of the magnetization. The red solid lines show the result of the curve fitting. (c) Calculated magnetization dynamics along the z axis. The amount of the magnetization decrease is determined by the amplitude of the oscillations in presupposed in (b)

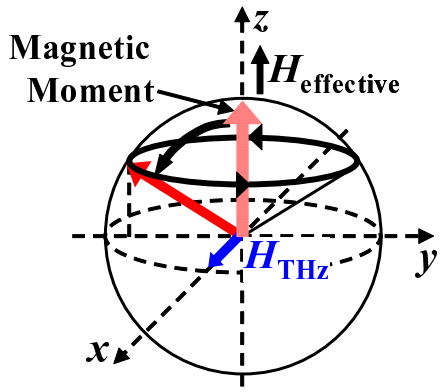

FIG. 2.3 Illustration showing the magnetization dynamics induced by the THz pulse. The magnetic moment is instantaneously tilted by the THz magnetic field and begins precession motion around the z axis.

pulse can excite the spin precession motion. This behavior is similar to the requirement of impulsive coherent phonon excitation experiment where the exciting impulse must be shorter than half the period of the phonon frequency.

Thus, simulation with the Landau-Lifshitz-Gilbert equation predicts that excitation of spin system with pulsed THz wave results in impulsive excitation of spin precession whose oscillation frequency is determined by the effective magnetic field inside the sample. In addition, it was also confirmed that the magnetic component of the THz pulse should work as a half cycle magnetic pulse against the spin system.

2.1.3 Detection of the Spin Precession through Free Induction Decay Signal

As shown in the previous section, excitation of spins in a magnetic materials with a THz pulse is expected to induce coherent precession motion of magnetization with a frequency corresponding to its magnetic resonant frequency. When an oscillating magnetic dipole exists, electromagnetic emission is generated [34]. The polarization of such far field emission from a magnetic dipole oscillating along $\boldsymbol{n}$ is $\boldsymbol{E} \perp \boldsymbol{n}$ and $\boldsymbol{B} \parallel \boldsymbol{n}$. When the magnetic dipole is

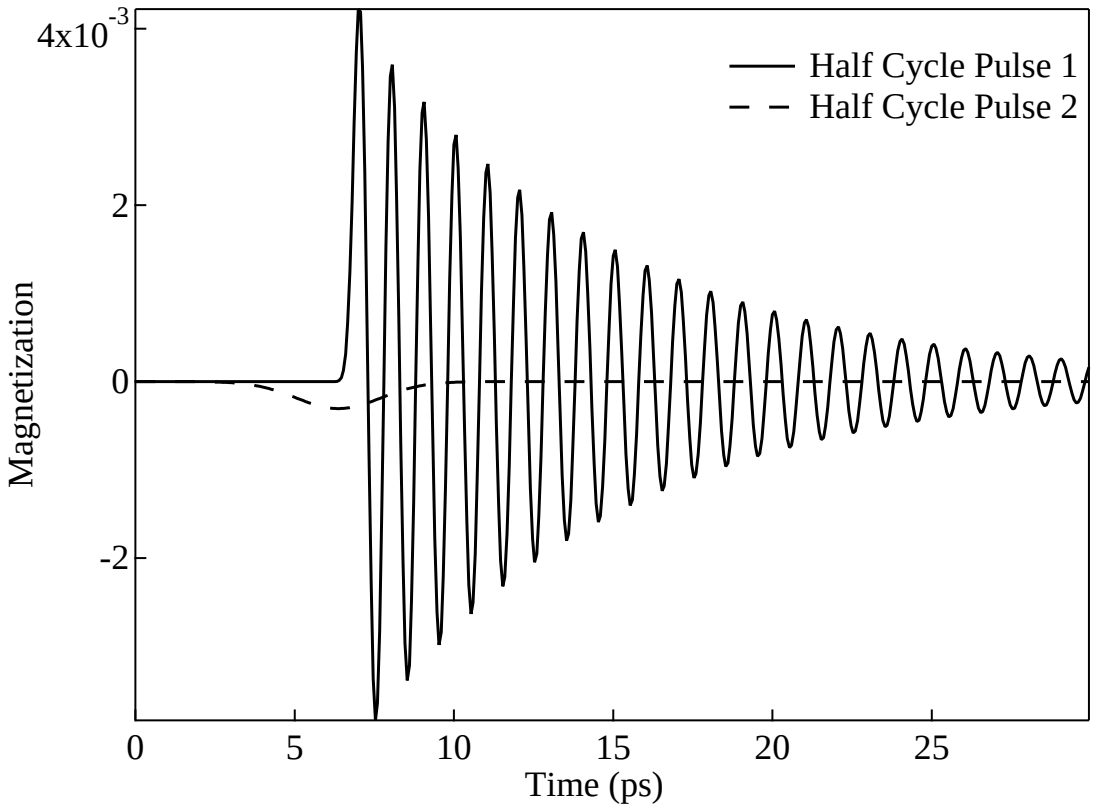

FIG. 2.4 Motion of the magnetic mmoment induced by two types of half cycle magnetic field pulses that forms the THz pulse shown in Fig.2.2(a). The narrow half cycle pulse (pulse 1) is responsible for excitation of the oscillation. The effect of the broad half cycle pulse (pulse 2) is negligible compared to the half cycle pulse 1.

placed at the origin, the amplitude of the emission at point $\boldsymbol{R}$ is

$$E_{\perp} \propto \frac{-1}{c^2 R}[\frac{d^2 M(t)}{dt^2}]\sin\theta, \tag{2.10}$$

$$B_{\parallel} \propto \frac{1}{c^2 R}[\frac{d^2 M(t)}{dt^2}]\sin\theta, \tag{2.11}$$

where c is the velocity of light, R is the distance from the dipole, and θ is the angle between $\boldsymbol{R}$ and $\boldsymbol{n}$.

As an example, Fig.2.5 shows the emission from the x axis component oscillation obtained in the previous section. Here, emission which propagates along the z axis direction is considered. The figure shows that the emission shows damped oscillation with its frequency equivalent to that of the precession motion. Such emission is often referred to as the free induction decay (FID) signal. Since the FID signal can be detected with the THz-TDS method, it is useful for observing THz pulse induced ultrafast spin dynamics.

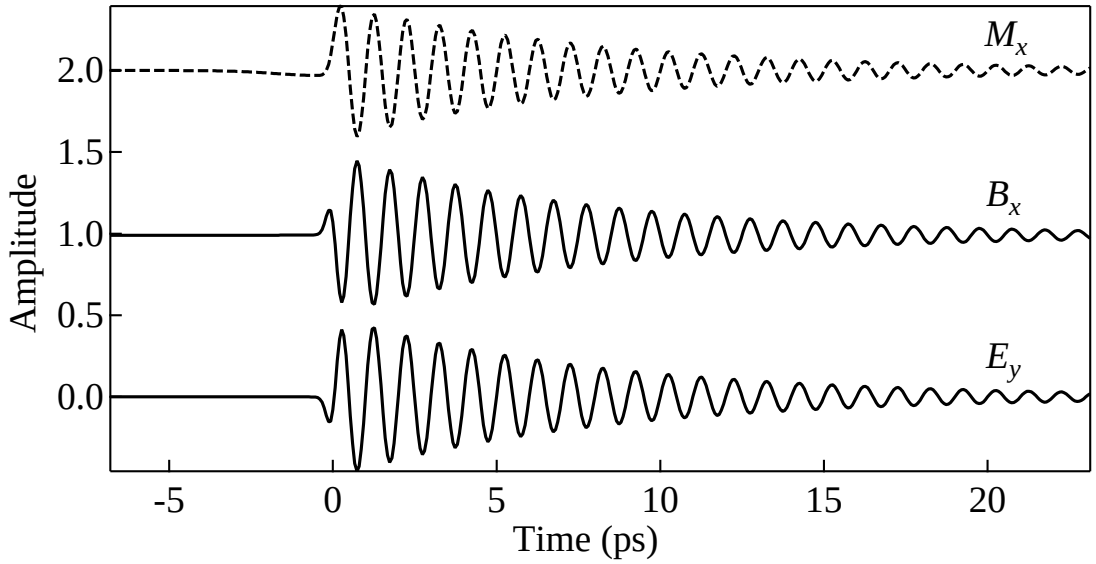

FIG. 2.5 Magnetic dipole radiation emitted from the oscillation of the magnetization in the x axis direction. The motion of the magnetization shown in Fig.2.2 is used for deriving the waveform of the emission.

This detection method through FID signals does not require introduction of additional probe pulse to the spin systems and therefore the dynamics of the spins can be observed without altering their state. This point is especially advantageous for applicative usage of the ultrafast spin excitation for memory devices. However, as eqs. (2.10) and (2.11) describes, since the amplitude of the emission toward the direction parallel to the oscillating dipole (θ=0 direction) is zero, information on the motion of the magnetic moment parallel to the incident THz wave vector can not be obtained. Therefore, usage of FID emission is limited to observation of in-plane magnetization dynamics.

2.1.4 Detection of the Spin Precession through Faraday Rotation of Visible Probe Pulse

To study magnetization dynamics in a thin sample, instead of using FID emission, observation with Faraday effect is suitable. When a linearly polarized light transmits through a magnetized substance, the polarization of the light is known to rotate. In the case where the magnetization is parallel to the wave vector of the transmitting light, this phenomenon is known as the Faraday effect [35–37].

Phenomenologically, the Faraday effect can be explained as follows. To simplify the explanation, we consider isotropic medium where the dielectric tensor can be written as

$$\varepsilon = \begin{bmatrix} \varepsilon_{xx} & 0 & 0 \\ 0 & \varepsilon_{xx} & 0 \\ 0 & 0 & \varepsilon_{xx} \end{bmatrix}. \tag{2.12}$$

Introduction of a magnetization M along z axis alters the dielectric tensor and in this case, it can be written as

$$\varepsilon = \begin{bmatrix} \varepsilon_{xx} & \varepsilon_{xy} & 0 \\ -\varepsilon_{xy} & \varepsilon_{xx} & 0 \\ 0 & 0 & \varepsilon_{zz} \end{bmatrix}. \tag{2.13}$$

Following the relation derived by Onsager,

$$\varepsilon_{ij}(-M) = \varepsilon_{ji}(M), \tag{2.14}$$

the diagonal matrix element of the dielectric tensor and the off-diagonal element can be expanded in the following manner.

$$\varepsilon_{xx}(M) = \varepsilon_{xx}^{(0)} + \sum_n \varepsilon_{xx}^{(2n)} M^{2n}/(2n)! \tag{2.15}$$

$$\varepsilon_{xy}(M) = \sum_n \varepsilon_{xy}^{(2n+1)} M^{2n+1}/(2n+1)! \tag{2.16}$$

$$\varepsilon_{zz}(M) = \varepsilon_{zz} + \sum_n \varepsilon_{zz}^{(2n)} M^{2n}/(2n)! \tag{2.17}$$

Considering an electromagnetic wave propagating along z axis of this medium, two circular polarization with opposite helicities

$$\boldsymbol{E}_{\pm} = \frac{E_0}{\sqrt{2}}(\boldsymbol{x} + i\boldsymbol{y}) \exp(-i\omega(t - \frac{N_{\pm}}{c}z)) \tag{2.18}$$

become the eigenvector of the characteristic equation. The complex refractive index for these two polarizations are

$$N_{\pm} = \sqrt{\varepsilon_{xx} \pm i\varepsilon_{xy}}. \tag{2.19}$$

Owing to this difference of refractive index between the two circular polarization, the polarization of the linearly polarized light transmitted through this medium is rotated. This rotation angle which is often referred to as the Faraday rotation angle can be given by

$$\theta_F = -\frac{\omega(n_+ - n_-)}{2c} l \tag{2.20}$$

where l is the thickness of the medium. Since Faraday rotation is usually measured in an optical region where the medium is transparent, $\kappa = 0$ and $(n_+ - n_-)$ can be replaced with $-\mathrm{Im}\,\varepsilon_{xy}/n$. By neglecting the higher order terms of M, from equation (2.16), $\mathrm{Im}\,\varepsilon_{xy} = \mathrm{Im}\,\varepsilon_{xy}^{(1)} M$. Therefore, the Faraday rotation angle becomes

$$\theta_F = \frac{\omega\,\mathrm{Im}\,\varepsilon_{xy}^{(1)} M}{2cn} l. \tag{2.21}$$

It can be seen that the amount of Faraday rotation angle is proportional to the amplitude of the magnetization parallel to the wave vector of the transmitting light. If there is a fluctuation of the magnetization ΔM along the z axis, such motion can be detected as the fluctuation of the Faraday rotation $\Delta\theta_F \propto \Delta M$. Therefore, the Faraday rotation of the visible probe pulse can be used as the alternative way to detect ultrafast spin dynamics induced by THz pulse. In fact, this method is widely used in the visible laser ultrafast spin excitation experiments.

Although the observation of spin dynamics with the Faraday effect is limited to a thin sample where the probe pulse can transmit through, this method has several advantages when compared to the method using the FID signal. First, this method enables visualization of magnetization dynamics in the direction parallel to the propagation of the incident THz pulse, which cannot be observed with THz FID signal. Another point is that the spin dynamics can be spatially resolved in a resolution which is much higher than the FID method. This is because the resolution of the FID signal is regulated by the wavelength of the FID emission which is in submillimeter range in this research. On the other hand, the resolution of the detection method with Faraday rotation is limited by the diffraction limit of the visible probe pulse and enables highly spatially resolved observation of spin dynamics. Therefore, for studying ultrafast spin dynamics, observation with the Faraday effect can be used as a complementary approach to the observation method with FID signal.

2.2 Rare-earth Orthoferrite $RFeO_3$

In this research, a group of chemical compounds known as orthoferrite are used as the samples. The formula of the orthoferrites are $RFeO_3$ where R is a rare-earth. The crystal structure of an orthoferrite is shown in Fig.2.6. $RFeO_3$ has orthorhombic and has distorted perovskite

structure. It belongs to the space group number 62, Pnma (Pbnm). There are four iron ion sublattices and four rare-earth ion sublattices in a unit cell. Below the Néel temperature T_N of about 600 K, the nearest neighbor iron ion sublattice spins order antiferromagnetically. In addition, due to antisymmetric exchange (Dzyaloshinskii-Moriya interaction) between the Fe^{3+} spins, the spins are ordered into canted antiferromagnetic structure. This canting gives rise to a weak ferromagnetic moment. For this reason, $RFeO_3$ is called weak ferromagnet or canted antiferromagnet. Owing to this weak ferromagnetic moment, orthoferrites possess a unique antiferromagnetic resonance mode which behaves similarly to that of the ferromagnetic resonance. Except for a very low temperature region of about few Kelvin, magnetic rare-earth ion spins are paramagnetic [38–43].

2.2.1 Spin Configuration in Orthoferrite

Here, following the notation used by Bertaut [44], the configuration of the Fe^{3+} spins in orthoferrites are reviewed. Instead of considering four separate sublattice spins, the following set of linear combinations of these spins are used.

$$\boldsymbol{F} = \boldsymbol{S_1} + \boldsymbol{S_2} + \boldsymbol{S_3} + \boldsymbol{S_4} \tag{2.22}$$

$$\boldsymbol{G} = \boldsymbol{S_1} - \boldsymbol{S_2} + \boldsymbol{S_3} - \boldsymbol{S_4} \tag{2.23}$$

$$\boldsymbol{C} = \boldsymbol{S_1} + \boldsymbol{S_2} - \boldsymbol{S_3} - \boldsymbol{S_4} \tag{2.24}$$

$$\boldsymbol{A} = \boldsymbol{S_1} - \boldsymbol{S_2} - \boldsymbol{S_3} + \boldsymbol{S_4} \tag{2.25}$$

The labels 1, 2, 3 and 4 correspond to the Fe^{3+} sublattices labeled in Fig.2.6. Considering the transformation properties of each base vector components under symmetry operations of the space group Pbnm, four possible spin configurations are derived. These four configurations are as follows:

$\Gamma_1(A_xG_yC_z)$ where

$$s_{1x} = -s_{2x} = -s_{3x} = s_{4x},\ s_{1y} = -s_{2y} = s_{3y} = -s_{4y},\ s_{1z} = s_{2z} = -s_{3z} = -s_{4z},$$

$\Gamma_2(F_xC_yG_z)$ where

$$s_{1x} = s_{2x} = s_{3x} = s_{4x},\ s_{1y} = s_{2y} = -s_{3y} = -s_{4y},\ s_{1z} = -s_{2z} = s_{3z} = -s_{4z},$$

$\Gamma_3(C_xF_yA_z)$ where

$$s_{1x} = s_{2x} = -s_{3x} = -s_{4x},\ s_{1y} = s_{2y} = s_{3y} = s_{4y},\ s_{1z} = -s_{2z} = -s_{3z} = s_{4z},$$

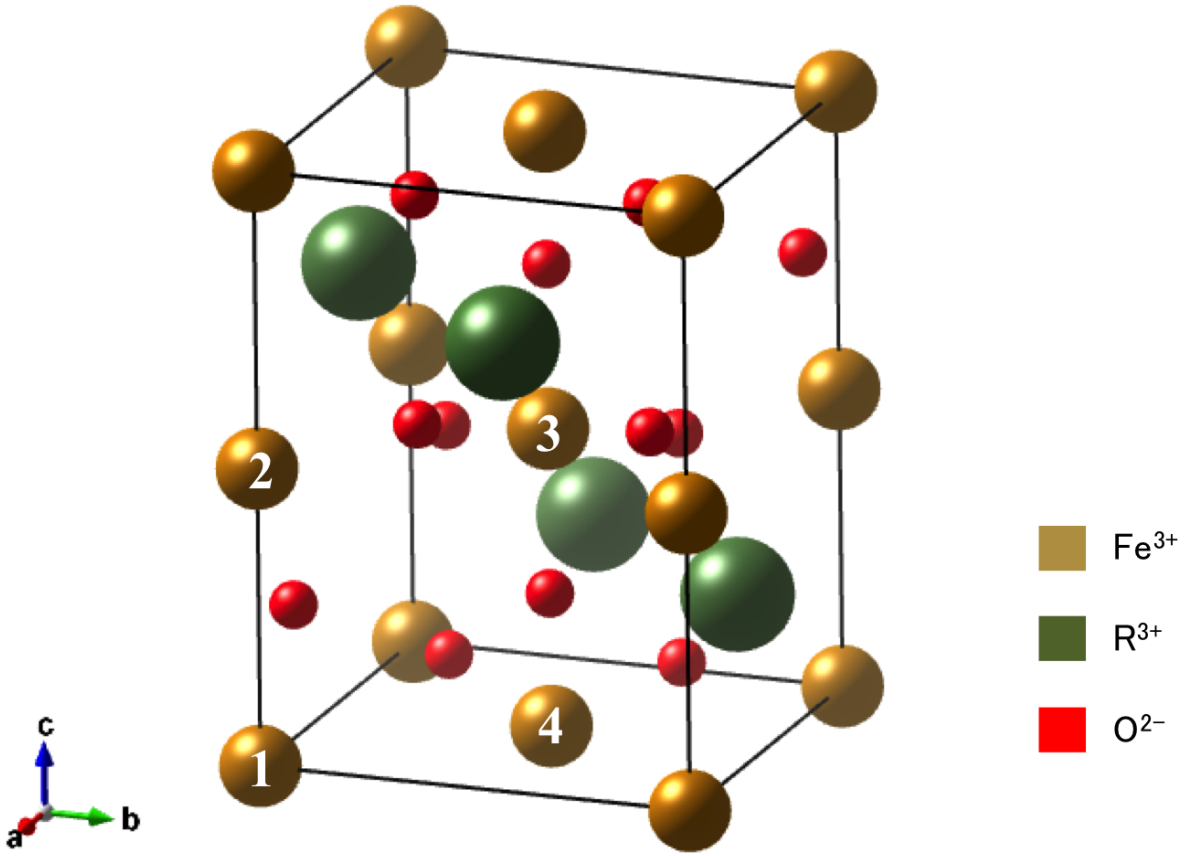

FIG. 2.6 Crystallographic structure of the unit cell of the orthoferrite. This structure belongs to the space group Pbnm. The four sublattice Fe^{3+} ion sites are labeled 1, 2, 3, and 4.

$\Gamma_4(G_xA_yF_z)$ where

$$s_{1x} = -s_{2x} = s_{3x} = -s_{4x},\ s_{1y} = -s_{2y} = -s_{3y} = s_{4y},\ s_{1z} = s_{2z} = s_{3z} = s_{4z}.$$

In this thesis, the crystallographic axes a, b and c are chosen as the axes x, y and z, respectively.

As mentioned before, in the orthoferrites, the interaction between the nearest neighbor Fe^{3+} spins are antiferromagnetic. Therefore, the nearest neighbors such as 1 and 2, 1 and 4, 3 and 2, and 3 and 4 in Fig.2.6 should be aligned antiparallel to each other [45]. For this reason, configuration Γ_3 is ruled out as an equilibrium spin configuration in orthoferrites. All of the other configurations, namely Γ_1, Γ_2, Γ_4 are allowed in orthoferrites and these three types of

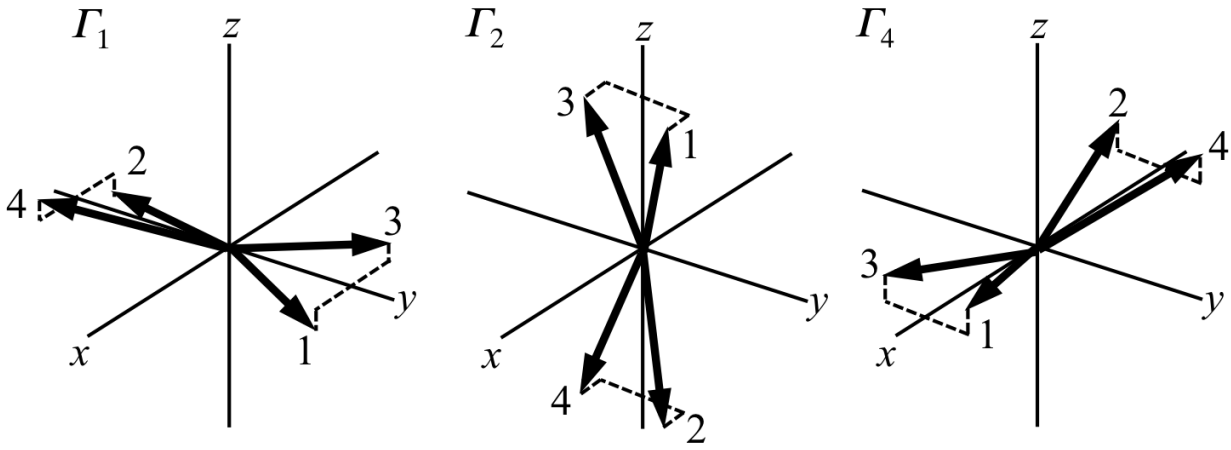

FIG. 2.7 Equilibrium Fe^{3+} spin configurations allowed in the orthoferrites. Indices 1, 2, 3, and 4 corresponds to the iron ion spin sublattices shown in Fig.2.6.

configurations are illustrated in Fig.2.7.

The most commonly observed phase in the orthoferrites are Γ_4 phase, where each sublattice spins align in an antiferromagnetic fashion along the x axis [45–47]. In addition, an overt canting inside the x-z plane and a hidden canting inside x-y plane exist. This overt canting gives rise to the weak ferromagnetic moment along the z axis direction. The overt canting angle (the angle between the spin and x-y plane) and the hidden canting angle (the angle between the spin and the x-z plane) in orthoferrite $YFeO_3$ are 0.75 degree and 1.25 degree, respectively [48]. In all types of orthoferrites where the rare-earth ions are nonmagnetic ions, the spin configuration of Fe^{3+} spins below the Néel temperature is always Γ_4.

In some orthoferrites where the rare-earth ions are magnetic, temperature induced phase transition between Γ_4 and Γ_2, or Γ_4 and Γ_1 are known to occur [46, 47]. These phase transitions are known as the spin reorientation transitions. In both types of the phase transitions, the spin configuration just below the Néel temperature is Γ_4. These phase transitions can be interpreted as follows. As the temperature is lowered, the magnitude of the paramagnetic R^{3+} magnetizations start to increase. Then, the interaction between the rare-earth spins and iron spins will also increase. When this interaction becomes larger than the single ion anisotropy of the iron ion spins, the equilibrium orientation of the iron spins changes. Therefore, R^{3+} spins play a vital role in the spin reorientation transition and this is the reason why no such

transition occurs in orthoferrites with nonmagnetic rare-earth ions.

The transition between Γ_4 and Γ_2 is called the rotational type spin reorientation because the spin configuration in this type of transition is known to change continuously from Γ_4 to Γ_2 and vice versa. In this rotational reorientation, two different transition temperature, T_1 and T_2 are known to exist. As the temperature is lowered, the easy axis of the spins in Γ_4 configuration starts to rotate at a temperature T_2. When the angle of this rotation reaches 90 degree and the spin configuration becomes Γ_2 at another temperature T_1, the rotation stops. Owing to this phase transition, the direction of the weak ferromagnetic moment also rotates from z axis in Γ_4 phase to x axis in Γ_2 phase. This type of spin reorientation is known to appear in orthoferrites where the rare-earth are Nd, Sm, Tb, Ho, Er, Tm, and Yb.

The another type of the spin reorientation from Γ_4 to Γ_1 is known as the abrupt type spin reorientation for this reorientation occurs abruptly at the transition temperature T_r. Because Γ_1 phase has no macroscopic magnetization, abrupt type transition from Γ_4 phase to Γ_1 phase results in disappearance of the weak ferromagnetic moment. This type of spin reorientation transition is quite rare in the orthoferrites and only $DyFeO_3$ is known to show this phase transition.

2.2.2 Magnetic Resonance Modes in Orthoferrite

Next, we will focus on magnetic resonance in orthoferrites. With the commonly used two sublattice approximation $\boldsymbol{s_1} = \boldsymbol{s_3}$, and $\boldsymbol{s_2} = \boldsymbol{s_4}$, the Hamiltonian of the Fe^{3+} spins in the Γ_4 configuration can be written as

$$H = 2JZ\boldsymbol{s_1} \cdot \boldsymbol{s_2} + D(s_{1x}s_{2z} - s_{1z}s_{2x}) - A_x(s_{1x}^2 + s_{2x}^2) - A_y(s_{1y}^2 + s_{2y}^2) - A_z(s_{1z}^2 + s_{2z}^2) \quad (2.26)$$

where J is the exchange constant, D is the Dzyaloshinskii constant, A_x, A_y, A_z are the anisotropy constant, and $Z = 6$ is the number of the nearest neighbor Fe^{3+} spins.

The equations of motion for $\boldsymbol{s_1}$ and $\boldsymbol{s_2}$ are obtained by

$$\dot{\boldsymbol{s}}_{\boldsymbol{i}} = -i[\boldsymbol{s}_{\boldsymbol{i}}, H]. \quad (2.27)$$

Substituting $s_{1x} = 1$ and $s_{2x} = -1$, and ignoring the higher order terms of s_{iy} and s_{iz}, the equation of motion can be written as

$$\begin{pmatrix} \dot{s}_{1y} \\ \dot{s}_{2y} \\ \dot{s}_{1z} \\ \dot{s}_{2z} \end{pmatrix} = \begin{pmatrix} 0 & 0 & 12J + 2(A_x - A_z) & 12J \\ 0 & 0 & -12J & -12J - 2(A_x - A_z) \\ -12J - 2(A_x - A_y) & -12J & 0 & 0 \\ 12J & 12J + 2(A_x - A_y) & 0 & 0 \end{pmatrix} \begin{pmatrix} s_{1y} \\ s_{2y} \\ s_{1z} \\ s_{2z} \end{pmatrix} + constant \tag{2.28}$$

From the eigenvalues of this matrix, two different resonant frequencies

$$\omega_1 \propto 2\sqrt{12J(A_x - A_z)} \tag{2.29}$$

$$\omega_2 \propto 2\sqrt{12J(A_x - A_y)} \tag{2.30}$$

are obtained. Here, because $J \gg A$, terms on the order of A^2 were dropped. The resonance modes with resonant frequencies ω_1 and ω_2 are often referred to as the quasiferromagnetic mode (F mode) and quasiantiferromagnetic mode (AF mode), respectively [49–51]. The motion of sublattice spins and macroscopic magnetization is shown in Fig.2.8. As shown in the figure, F mode magnetic resonance involves precession motion of the macroscopic weak ferromagnetic moment and this is the reason this resonance mode is called quasiferromagnetic. AF mode on the other hand, does not involve precession of the macroscopic moment. This mode can be observed as the fluctuation motion of the macroscopic magnetic moment. As described in the figure, the motion of each sublattice spins are highly elliptic [45]. Therefore, the resultant precession of the weak ferromagnetic moment in F mode resonance is also elliptic.

These two modes are optically active and can be excited with application of oscillating magnetic field. The F mode resonance couples to the oscillating magnetic field perpendicular to the weak ferromagnetic moment (magnetic field inside *ab* plane in Γ_4 phase), and the AF mode is excited by oscillating magnetic field parallel to the macroscopic moment (along *c* axis in Γ_4 phase) [45, 52]. Herrmann's theoretical work has shown that in the Γ_1 phase where no macroscopic magnetization exists, F mode is excited by oscillating magnetic field along *a* axis, and AF mode is excited by magnetic field along *c* axis [45].

From the spectroscopic measurement using tunable monochromatic oscillator called the backward-wave oscillators (BWO), the resonant frequencies of the two magnetic resonance

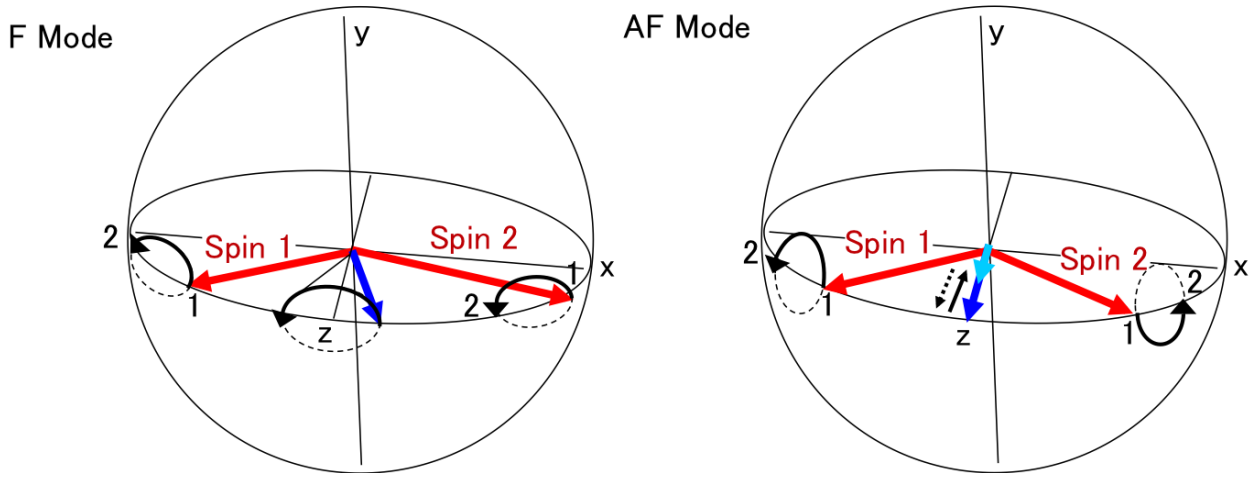

FIG. 2.8 Antiferromagnetic magnetic resonance mode in Γ_4 phase orthoferrites. The blue arrow pointing toward the z axis is the weak ferromagnetic moment due to the canting of Fe^{3+} spins.

modes in orthoferrites are known to exist in the sub-THz region [49], and this makes it suitable for excitation of the magnetic resonance with THz pulses.

2.3 Purpose of this Research

This research focuses on how the antiferromagnetic spin systems react to the magnetic field component of the THz pulse. One of the main purpose is to investigate whether ultrafast excitation of the spin precession motion can be conducted in an analogous manner with that in the ferromagnetic spin systems. Such antiferromagnetic spin manipulation with THz pulse has not been reported prior to this research, and insights gained through this research on the applicability of the THz magnetic pulse to spin excitation is expected to open up a new way for the researches on the ultrafast spin excitations.

Another main purpose of this research is to observe characteristic behaviors of the spins that are unique to the orthoferrite $RFeO_3$ by using THz pulse excitation. As stated in the previous section, the Fe^{3+} spins in orthoferrites show various characteristic behaviors such as separation into four sublattices, macroscopic magnetization due to the canting, and spin reorientation transition caused by the rare-earth magnetization. Owing to such complex spin characteristics, some undiscovered responses of the spin systems may perhaps be observed, especially with strong excitation of the spins with high intensity THz pulse.

Chapter3

Experimental Method

In this chapter, experimental method of THz time domain spectroscopy (TDS) is described. As it was shown in 1.1(a), the generated THz pulses are generally single cycle electromagnetic waves with picosecond order duration. In order to record the electric field component amplitude of the THz pulse, femtosecond visible laser is used as a gate pulse (Fig. 3.1). By doing so, the THz amplitude at a certain point of time can be measured with femtosecond order precision. The whole temporal waveform of the THz pulse can be obtained by varying the optical path difference between the THz pulse and the gate pulse.

In the following sections, details in generation and detection methods of the THz pulse are discussed.

3.1 Terahertz Generation and Detection with Photoconductive Antennas

One of the generation method used in this research is to use emission from biased photoconductive antennas. The antennas used here are composed of low temperature grown GaAs substrate with a pair of electrodes deposited on its surface. Typically, the distance between the two electrodes are about 5 μm (Fig.3.2). When the femtosecond laser pulse excites the biased antenna, the generated free carrier is accelerated by the bias electric field, resulting in induction of transient current $I(t)$. Owing to the existence of a time varying current, electromagnetic wave with its electric field component $E \propto dI(t)/dt$ is generated. Sharp rise of the photoexcited carriers due to the femtosecond laser and fast decay (~0.5 ps) of the car-

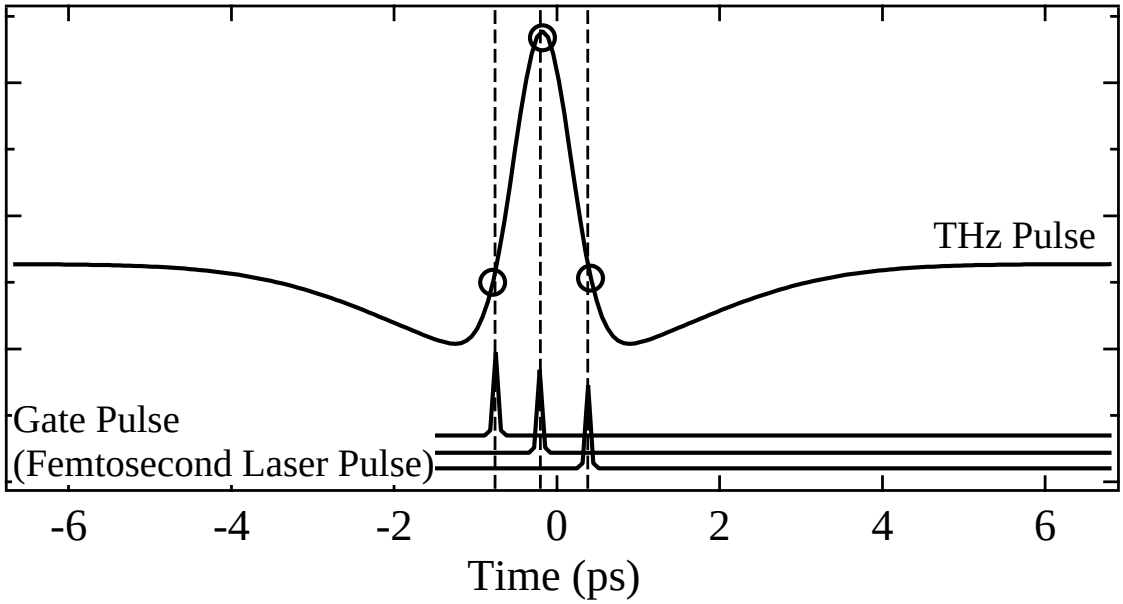

FIG. 3.1 Concept of the THz TDS method. The femtosecond gate pulse detects the THz electric field with femtosecond order time resolution and records the time evolution of the THz pulse.

riers due to defects in the LT grown GaAs substrate result in emission of picosecond order electromagnetic wave which coincides with the previously mentioned THz pulse.

The detection of the THz pulse with a photoconductive antenna is the inverse process of the generation method. When the THz pulse enters the antenna, the electric field component of the THz pulse acts as a bias field of the antenna. Thus, when a femtosecond gate pulse excites the antenna and generates free carriers, a transient current proportional to the THz electric field component is induced. By recording these signals for each point of time, the temporal waveform shown in Fig. 1.1(a) can be obtained. The time resolution for detection of the THz pulse is regulated by the life time of the photoexcited carriers as well as the temporal width of the incident gate pulse. Therefore, the carrier life time must be suppressed in order to achieve high time resolution and this is the reason why low temperature grown GaAs substrate is used for the photoconductive antennas.

Since the pulse energy required to operate photoconductive antennas can be supplied by a femtosecond oscillator which has high repetition rate of about 80 MHz, quite high signal to noise ratio of about 10^3 (in electric field amplitude) can be easily achieved. However, it

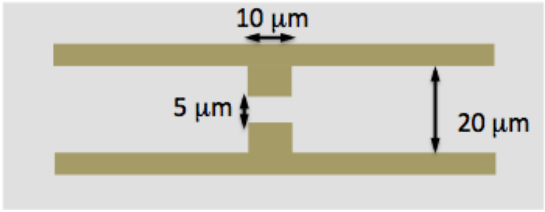

FIG. 3.2 Schematic of electrodes in a dipole type photoconductive THz antenna.

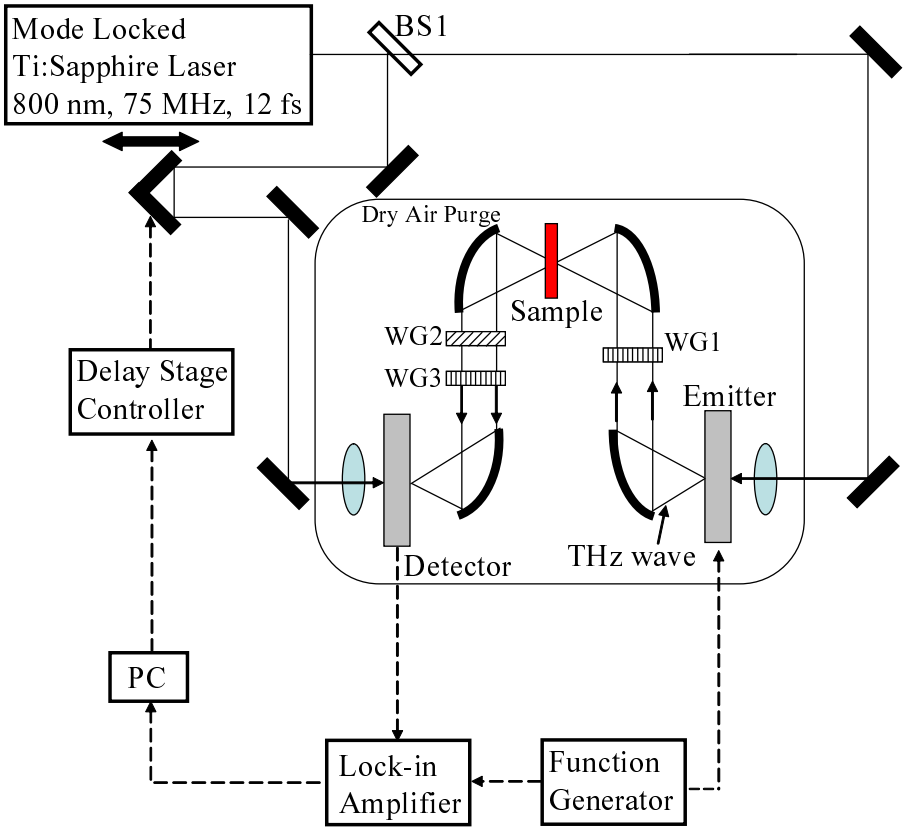

FIG. 3.3 THz-TDS system with photoconductive antennas used for this research. BS and WG stands for beam splitter and wire grid polarizer, respectively.

should be noted that the peak strength of the THz electric field generated with this method is in the order of 10 V/cm which is quite low compared to the recently established high intensity THz generation methods. Therefore, the method described above is suitable for observing fundamental linear response of the materials in the THz region.

The schematic of the actual antenna based THz-TDS system used for this research is shown in Fig.3.3. Mode locked Ti:sapphire laser (center wavelength: 800 nm, repetition rate: 75 MHz, and temporal width: 12 fs) is separated by a beam splitter (BS1 in Fig.3.3) and each

beams are focused onto the emitter antenna and the detector antenna. For the antennas, dipole type antennas (Hamamatsu Photonics K.K.) were used. The fluence of the incident laser pulses are 15 mW for the emitter and 10 mW for the detector. In order to record the detector signal with lock-in detection, the emitted THz pulse was modulated by applying a sinusoidal bias with peak to peak value of 20 V and 51 kHz frequency to the emitter. The temporal waveform of the THz pulse can be measured by scanning the arrival time of the pumping pulse at the detector with the delay stage. The THz temporal waveform and the spectra in Fig.1.1 was obtained with this measurement system.

In this system, the emitted THz pulse is linearly polarized with its electric field component parallel to the horizontal direction. Hereafter, this polarization which is parallel with the THz pulse will be referred to as the parallel polarization and the polarization perpendicular to this direction will be called as the perpendicular polarization. To collimate and focus the THz pulse, off-axis paraboloid mirrors were used. The optical elements WG1-3 denote wire grid polarizers that work as a polarizing plate for THz waves. The polarization of WG1 and WG3 were fixed so as to make sure that the antennas emit and detect the horizontal electric field only. WG2 was used mainly for measuring the vertical component of the transmitted THz pulse. By measuring the THz signal for +45 degree polarization $(E_{parallel} + E_{perpendicular})/\sqrt{2}$ and -45 degree polarization $(E_{parallel} - E_{perpendicular})/\sqrt{2}$ and calculating the difference between the two signals, the perpendicular polarization component can be measured without rotating the emitter or the detector.

This THz-TDS method was used for obtaining all of the results introduced in chapter 4, and most of the results in chapter 5.

3.2 Terahertz Generation and Detection through Nonlinear Optical Effect

3.2.1 Generation Method

Another major method for THz generation is through second order nonlinear optical effect. When an optical pulse is emitted into a crystal which has no inversion symmetry, second order nonlinear polarization occurs. This polarization gives rise to emission of electromagnetic

field with frequencies that differ from that of the incident optical pulse: namely, sum frequency generation and difference frequency generation. Since the femtosecond visible laser is composed of light with broad range of frequency, the frequency of emission generated from the difference frequency generation reaches the THz region. In the following manner, this generation mechanism can also be interpreted as the optical rectification of the incident optical pulse. Electric field component of an ultrafast optical pulse can be represented as

$$E(t) = E_0(t)e^{i\omega t} \tag{3.1}$$

where ω is the center frequency of the optical pulse, and $E_0(t)$ is the envelope of the pulse. The nonlinear polarization corresponding to the optical rectification in this case is

$$P^{(0)}(t) = \frac{1}{2}\varepsilon_0\chi^{(2)}|E_0(t)|^2 \tag{3.2}$$

where $\chi^{(2)}$ is the second order nonlinear susceptibility of the nonlinear optical crystal. This time varying electrical polarization with its time duration in the range of 10 - 100 fs produces THz pulse. Along with high susceptibility (or electro-optic coefficient), phase matching between the group velocity of the pumping optical pulse and the phase velocity of the generated THz pulse is necessary for efficient THz pulse generation. Owing to high electro-optic coefficient and phase matching characteristics suitable for excitation with Ti:Sapphire femtosecond laser (central wavelength at around 800 nm), ZnTe is one of the most commonly used nonlinear crystal for THz generation through optical rectification. The electric field amplitude of the generated THz pulse from 2 mm thick ZnTe with 1 kHz Ti:Sapphire amplifier (pulse energy $\sim$ 1 mJ) at focal point reaches 10 kV/cm [53].

Compared to ZnTe, the nonlinear susceptibility of $LiNbO_3$ is more than twice as large [8]. In addition, large band gap of $LiNbO_3$ suppresses THz absorption due to carrier generated by two photon absorption which is one of the major concerns in THz generation with ZnTe. For these reasons, $LiNbO_3$ possesses a potential for high intensity THz pulse generation. However, $LiNbO_3$'s large difference of the group velocity of optical pulse and the THz phase velocity makes it impossible to realize collinear phase matching. To overcome this issue, THz pulse generation with an optical pulse with tilted pulse front was proposed by Hebling *et al.* [7]. Following the Huygens' principle, THz pulse emitted from the tilted optical pulse propagates in the direction perpendicular to the pulse front. In such situation, the phase

matching condition is loosened to

$$v_{vis}^{gr} \cos\gamma = v_{THz}. \tag{3.3}$$

Here, γ represents the tilting angle of the pulse front. Therefore, by changing the tilting angle γ, phase matching condition can be fulfilled with $LiNbO_3$. It has been reported that intense THz pulse with its electric field amplitude reaching 1.2 MV/cm can be generated with this method [9].

3.2.2 Detection Method

THz pulse electric field can also be detected with nonlinear optical effect. This method, known as electro-optic (EO) sampling, utilizes the change of the refractive index induced by the electric field of THz pulse (Pockels effect). Electro-optic coefficient r_{ijk} is defined by

$$\begin{pmatrix} \Delta(1/n^2)_{11} \\ \Delta(1/n^2)_{22} \\ \Delta(1/n^2)_{33} \\ \Delta(1/n^2)_{23} \\ \Delta(1/n^2)_{31} \\ \Delta(1/n^2)_{12} \end{pmatrix} = \begin{pmatrix} r_{111} & r_{112} & r_{113} \\ r_{221} & r_{222} & r_{223} \\ r_{331} & r_{332} & r_{333} \\ r_{231} & r_{232} & r_{233} \\ r_{311} & r_{312} & r_{313} \\ r_{121} & r_{122} & r_{123} \end{pmatrix} \begin{pmatrix} E_1 \\ E_2 \\ E_3 \end{pmatrix}, \tag{3.4}$$

where $\Delta(1/n^2)_{ij}$ is the fluctuation of ijth component of the refractive index tensor due to the Pockels effect, and E_k is the external electric field (THz electric field component in this case). The commonly used EO crystals ZnTe and GaP crystals are isotropic crystals. In an isotropic crystal, all EO coefficients except for $r_{231}(= r_{41}) = r_{312} = r_{123} \neq 0$ are zero.

When a THz pulse and an optical probe pulse are incident on a (110) plane of these crystals with THz electric field component along $[1\bar{1}0]$ direction, index tensor for the optical probe pulse becomes

$$\begin{pmatrix} 1/n^2 & 0 & -r_{41}E_{THz}/\sqrt{2} \\ 0 & 1/n^2 & r_{41}E_{THz}/\sqrt{2} \\ -r_{41}E_{THz}/\sqrt{2} & r_{41}E_{THz}/\sqrt{2} & 1/n^2 \end{pmatrix}. \tag{3.5}$$

By transforming the coordinate in the following manner: $[001] \rightarrow x'$, $[1\bar{1}0] \rightarrow y'$, and $[110] \rightarrow z'$, the index ellipsoid can be orthogonalized to

$$(1/n^2 + r_{41}E_{THz})\left(\frac{x'-y'}{\sqrt{2}}\right)^2 + (1/n^2 - r_{41}E_{THz})\left(\frac{x'+y'}{\sqrt{2}}\right)^2 + \frac{z'^2}{n^2} = 1. \tag{3.6}$$

By ignoring the higher order terms of E_{THz}, the refractive indices become

$$n_{x'-y'} = n - \frac{1}{2}n^3 r_{41} E_{THz}, \tag{3.7}$$

$$n_{x'+y'} = n + \frac{1}{2}n^3 r_{41} E_{THz}, \tag{3.8}$$

$$n_{z'} = n. \tag{3.9}$$

Thus, THz electric field amplitude can be detected from the difference in the refractive indices between $x' - y'$ direction and $x' + y'$ direction.

In the actual measurement, the polarization of the incident optical probe was set parallel to the THz electric field (parallel to y' direction). A quarter wave plate was inserted after the EO crystal so that the probe pulse would become circularly polarized when no THz electric field is applied. Balance detection between the x' polarization and y' polarization yields

$$\Delta I = I_{x'} - I_{y'} = I_0 \sin \frac{2\pi n^3 r_{41} L E_{THz}}{\lambda}, \tag{3.10}$$

where I_0 is the incident optical probe intensity, L is the thickness of the EO crystal, and λ is the wavelength of the probe pulse in the vacuum.

3.2.3 THz TDS System Using Nonlinear Optical Effect

Generation and Detection with ZnTe

The actual THz-TDS system used in this research is shown in Fig.3.4. Femtosecond laser pulses generated from Ti:sapphire amplifier (Spitfire, Spectra Physics, 1 kHz repetition, 1 mJ/ pulse) was used for THz generation and detection. Here, (110) ZnTe with thickness of 1 mm and 2 mm were used as emitter and detector, respectively. Because the pumping pulse entering the emitter ZnTe is focused shortly before hitting the ZnTe crystal, vacuum cell is placed at the focal point so as to avoid generation of air plasma. The pumping pulse is modulated by optical chopper and the THz electric field amplitude obtained from balance detection of photodetectors 1 and 2 was detected with a lock-in amplifier. The THz temporal waveform and Fourier spectrum obtained with this system are shown in Fig.3.5. The peak electric field amplitude at the focal point was approximately 2 kV/cm. Few results described in chapter 5 were obtained with this system.

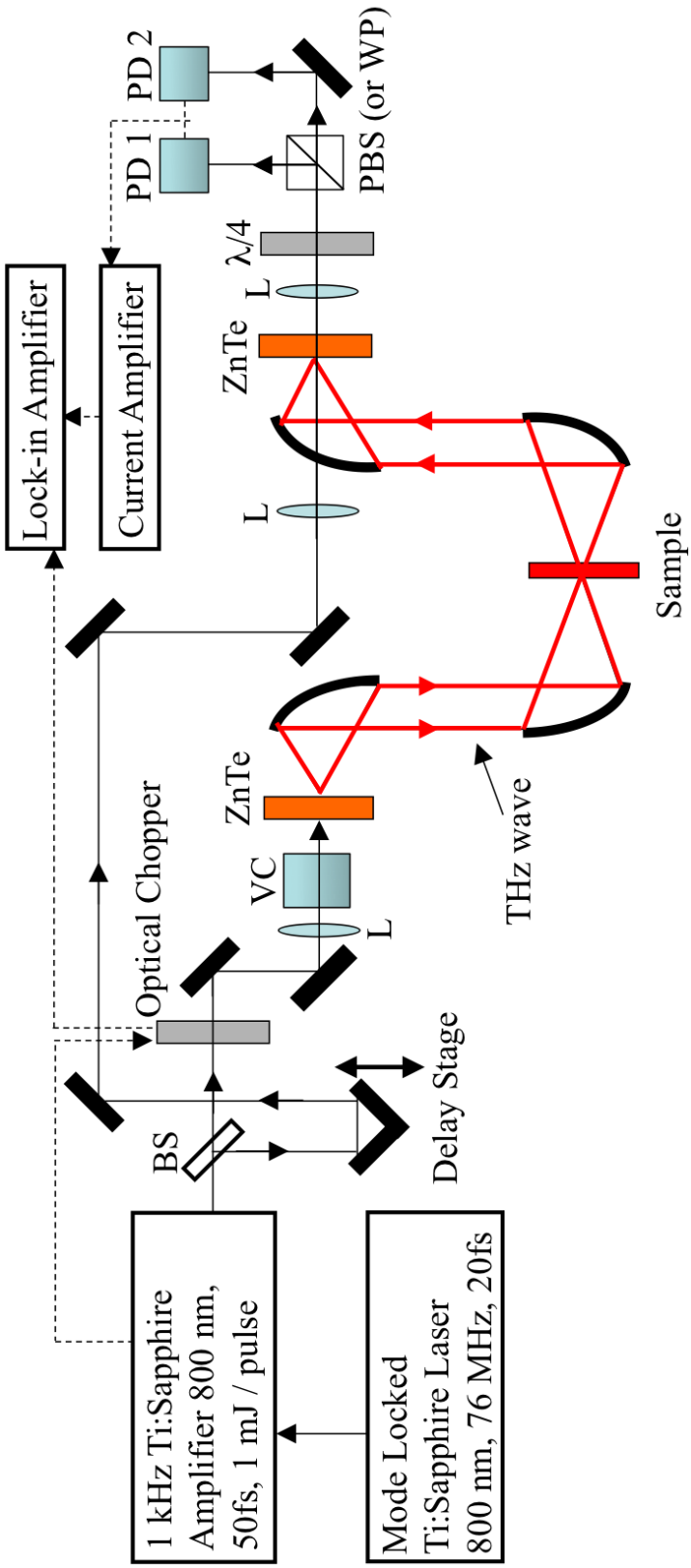

FIG. 3.4 THz-TDS system using optical rectification for generating the THz pulse and EO sampling for detection. (110) ZnTe is used for generation and detection. The meaning of the symbols are as follows. BS: beam splitter, L: lens, VC: vacuum cell, $\lambda/4$: quarter wave plate, PBS: polarizing beam splitter, WP: Wollaston prism, PD: photo detector.

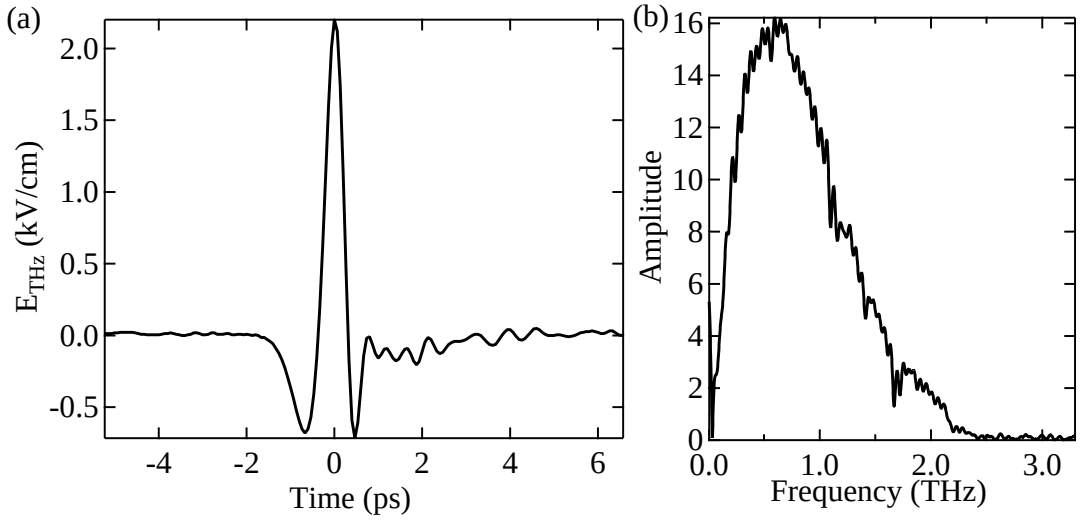

FIG. 3.5 (a)THz temporal waveform obtained from the TDS system shown in Fig.3.4. (b) Fourier spectrum of the waveform in (a).

Generation with $LiNbO_3$

For generation of high intensity THz pulse, instead of the system shown in Fig.3.4, THz generation with $LiNbO_3$ was used. As described in Fig. 3.6, the pulse front of the Ti: sapphire pumping pulse (Legend Elite, Coherent, 1 kHz repetition rate, 4 mJ/pulse) was titled by gratings. The generated THz pulse was transferred to the (110) GaP EO crystal with off-axis paraboloidal mirrors. Since the generated THz pulse is collimated in this case, the THz beam was expanded by a pair of paraboloidal mirrors that has short (10 mm) and long (101.6 mm) focal length. After expanding the beam diameter, THz beam was focused onto the GaP crystal with f = 50.4 mm paraboloidal mirror. As a result, THz pulse with electric field component of about 400 kV/cm, magnetic field component of about 0.13 T was obtained. The temporal waveform and the spectra of the THz pulse generated from this system is shown in Fig.3.7. Since the waveform in this figure was measured with diamond window cryostat, the peak value is reduced down to 70% of the value without a cryostat. The fringes in the THz spectra are due to the multiple reflection inside the diamond window. The THz wave generated from this system was used to obtain the results covered in chapter 6.

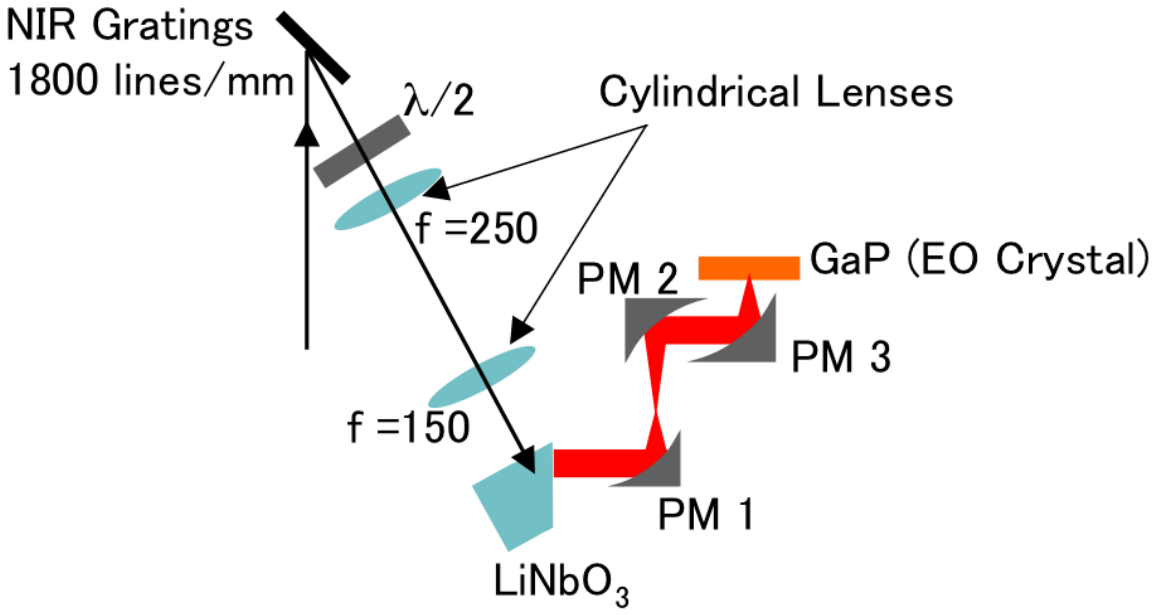

FIG. 3.6 THz generation with $LiNbO_3$. The pulse front tilting is realized by using gratings. The collimated THz emitted from the $LiNbO_3$ crystal is transferred by paraboloidal mirrors (PM) to an EO crystal GaP. The focal length of PM 1, PM 2, PM 3 were 10 mm, 101.6 mm, and 50.4 mm, respectively.

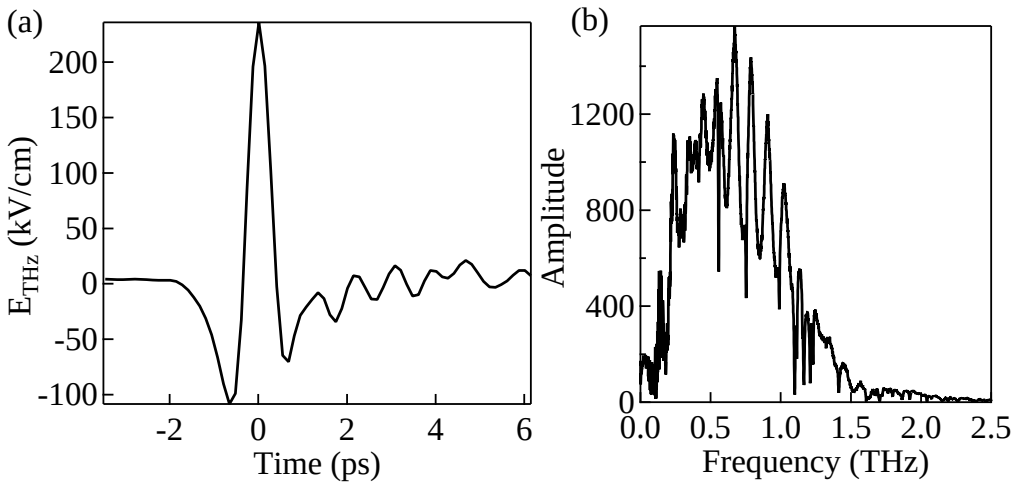

FIG. 3.7 (a)THz temporal waveform generated from $LiNbO_3$. (b) Fourier spectra of the waveform shown in (a).

3.3 Sample Preparation

In this thesis, the result of the experiments with single crystal $YFeO_3$, $ErFeO_3$, and $DyFeO_3$ and sintered pellet sample of $ErFeO_3$ are discussed.

The single crystal samples were grown with a method known as the Floating Zone (FZ) method where focused light of halogen lamps are used to melt the compressed rod of the raw material powders. Here, FZ furnace with four lamps were used. The parameters for growing the single crystal (growth rate of 4-6 mm/hour, oxygen atmosphere with flow rate of 2 l/min) were determined by referring to the references [54, 55]. As the lamps, four sets of lamps with 500 W output were used. The output power required for melting the samples varied for all three types of samples. Output power required for melting $YFeO_3$, $ErFeO_3$ and $DyFeO_3$ were 1.2 kW, 1.4 kW, and 1.3 kW, respectively. For stable growth of single crystal, sintering of the sample with a FZ furnace prior to starting the crystal growth was found to be highly effective. This sintering was performed with output power of approximately 1 kW. Interestingly, sintering with a similar temperature condition with a muffle furnace turned out to be ineffective.

The orientation of the crystallographic axes in the single crystal was investigated by X-ray Laue pattern, and plate type samples with desired surface direction were cut out from the single crystal rod.

The $ErFeO_3$ pellet sample was prepared using pellet die with 6 mm diameter. The pellet was sintered in a muffle furnace at 1500 °C for 4 hours. The thickness of the pellet was 1.6 mm.

Figure3.8 shows the microscopic image of the magnetic domains structure in $YFeO_3$ (001) single crystal at room temperature. Before applying external magnetic field to polarize the sample, two types of domains that are pointing toward and away can be seen. These two domains were distinguished by the Faraday rotation angle of the transmitted light. This image shows that the magnetic domains in this sample is quite large (100 to 200 μm in width). When the external magnetic field is applied, the figure shows that the domain structure completely disappears and the domain of the sample becomes uniform. After magnetizing the sample with sufficiently high magnetic field of about 10 mT, the domains were still uniformly ordered

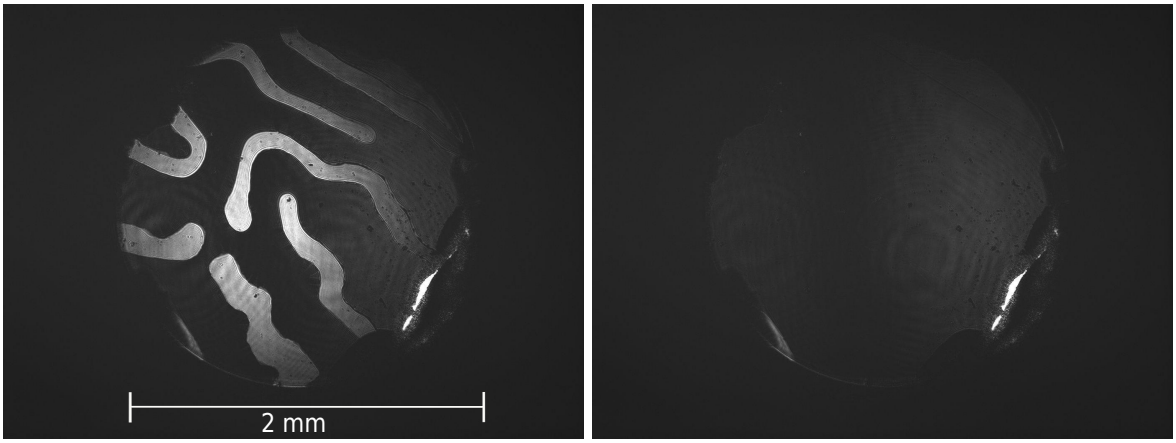

FIG. 3.8 Microscopic image of the magnetic domain structure of (001) $YFeO_3$ single crystal observed by Faraday rotation. The thickness of the sample was 100μm. The image on the left shows the domain structure before applying the magnetic field. The image on the right shows the domain structure after magnetizing the sample with external magnetic field.

even after removing the magnetic field. Domain size in $ErFeO_3$ was also confirmed to be as large as that of $YFeO_3$.

Chapter4

Excitation of $YFeO_3$ with Single and Double Pulses of THz Wave

4.1 Excitation of Spin Precession with Single THz Pulse

For the purpose of confirming how the spins react to the THz magnetic field, transmission-type THz-TDS measurements were performed on the single crystal $YFeO_3$ samples. The flat plate samples were cut out from the single crystal rod and the flat surfaces were polished. Samples with (100) surface, (010) surface and (001) surface were prepared for this experiment and their thicknesses are 1.7 mm, 1.5 mm, and 1.4 mm, respectively.

4.1.1 Excitation of Coherent Precession Motion within the Incident Polarization

Figure 4.1 shows the temporal waveforms of the THz pulse before and after transmitting the (100) plane surface sample. The transmitted THz pulses are followed by damped oscillations. These oscillations are the free induction decay signals emitted from the oscillating magnetizations. The figure clearly shows that the frequency of the oscillation varies with the polarization of the incident THz pulse. The oscillation with $H_{THz} \parallel b$ axis polarized THz pulse is much slower than the oscillation excited with $H_{THz} \parallel c$ axis polarization. Both oscillations can be can be fitted with $\cos(\phi + \omega t)\exp(-t/\tau)$. The frequency for $H_{THz} \parallel b$ is 0.299 THz which is equivalent to the resonant frequency of the F mode antiferromagnet resonance [49] and the relaxation time of the oscillation is approximately 40 ps. On the other

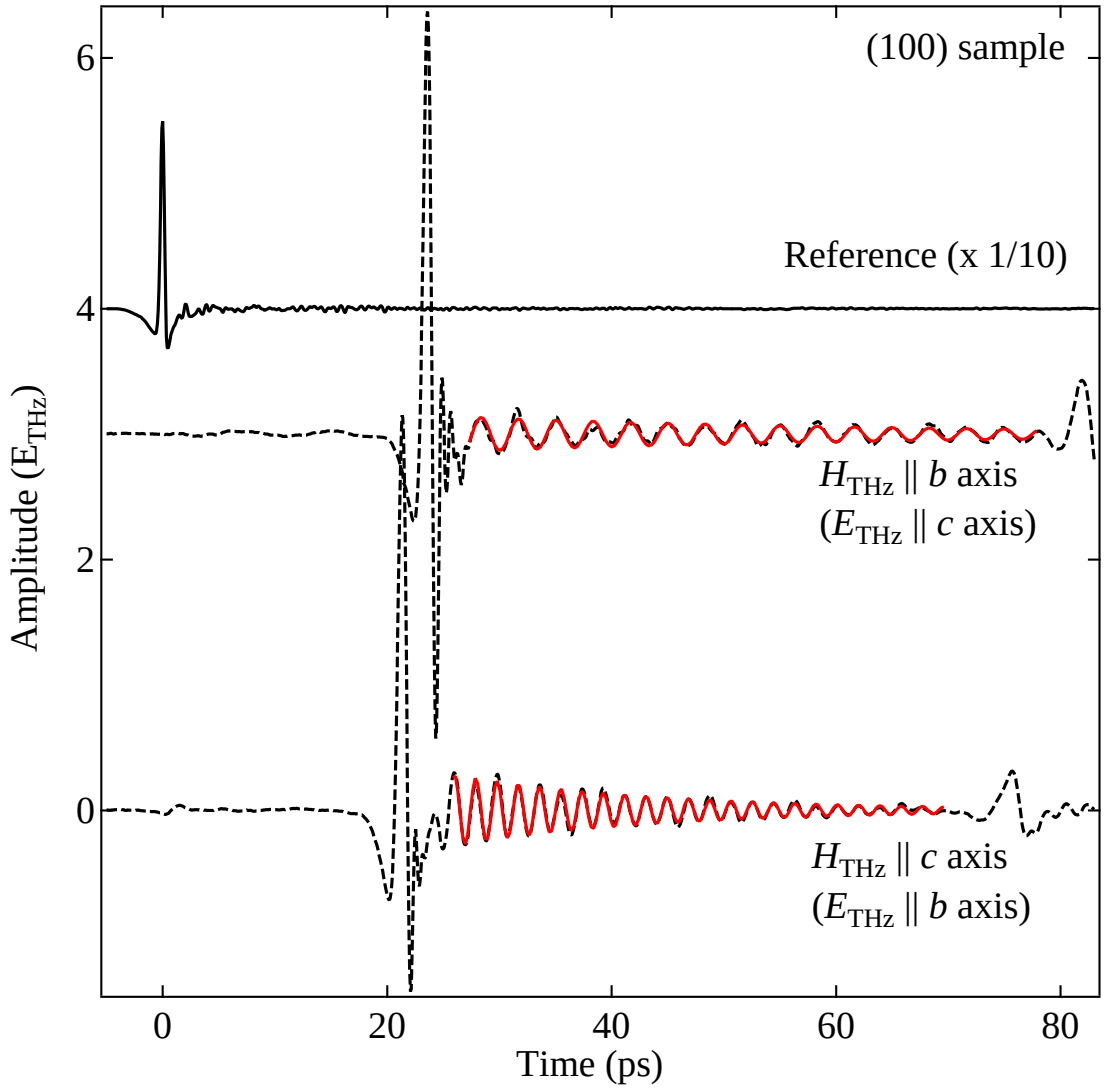

FIG. 4.1 Temporal THz waveforms obtained by THz-TDS experiment with (100) plane single crystal $YFeO_3$. The dashed lines show the experimental data and the red solid lines show the fitted curve of the oscillatory components.

hand, the frequency of the oscillation for $H_{THz} \parallel c$ is 0.53 THz and this coincides with the frequency of the AF mode resonance. The relaxation time in this case is about 20 ps. Similar behavior was also confirmed with the measurements on (010) sample and (001) sample (Fig.4.2). The measurements with these three samples can be summarized as follows: the frequency of the excited oscillations depend only on the direction of the magnetic field component of the THz pulse with respect to the crystal axis and they are completely independent of the direction of the THz electric field component. To sum up, excitation with the THz

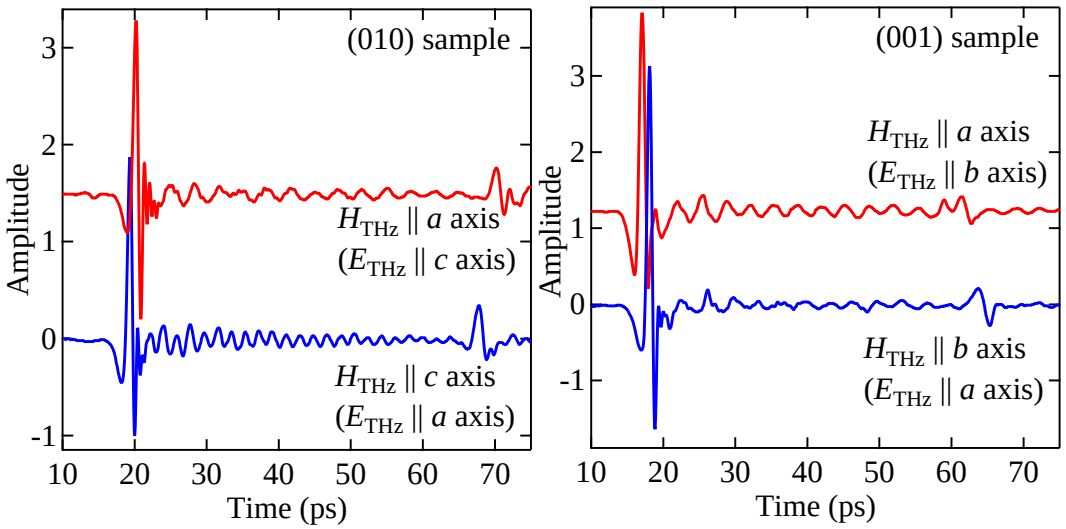

FIG. 4.2 Temporal THz waveforms obtained by THz-TDS experiment with (010) and (001) plane single crystal $YFeO_3$. The reference pulse with its peak at 0 ps is omitted from the figure.

magnetic field component parallel to the *a*-*b* plane of the $YFeO_3$ crystal results in excitation of the F mode resonance whereas excitation with the magnetic field component parallel to the *c* axis results in excitation of the AF mode resonance. These excitation conditions of antiferromagnetic modes are identical to the excitation conditions with monochromatic magnetic field where magnetic field perpendicular to the weak ferromagnetic moment excites the F mode and magnetic field parallel to the magnetization excites the AF mode [45, 52].

Thus, it was confirmed that THz pulse magnetic field component interacts with the spins and excites precession motion of the spins whose oscillation frequency is determined by the effective magnetic field intrinsic to the targeted spin system. This result is consistent with the prediction obtained from the Landau-Lifshitz-Gilbert equation and justifies the application of this equation for considering the interaction of the THz pulse magnetic field component with the spin system. Therefore, in the point of view of the ultrafast interaction with the THz pulse and the spin system, the energy of the incident THz pulse is passed on to the spin system within 1 ps and this energy is subsequently consumed by FID emission or some other energy dissipation paths such as spin-lattice relaxation.

To supplement, the delay of the transmitted main peak of the THz pulse with respect to

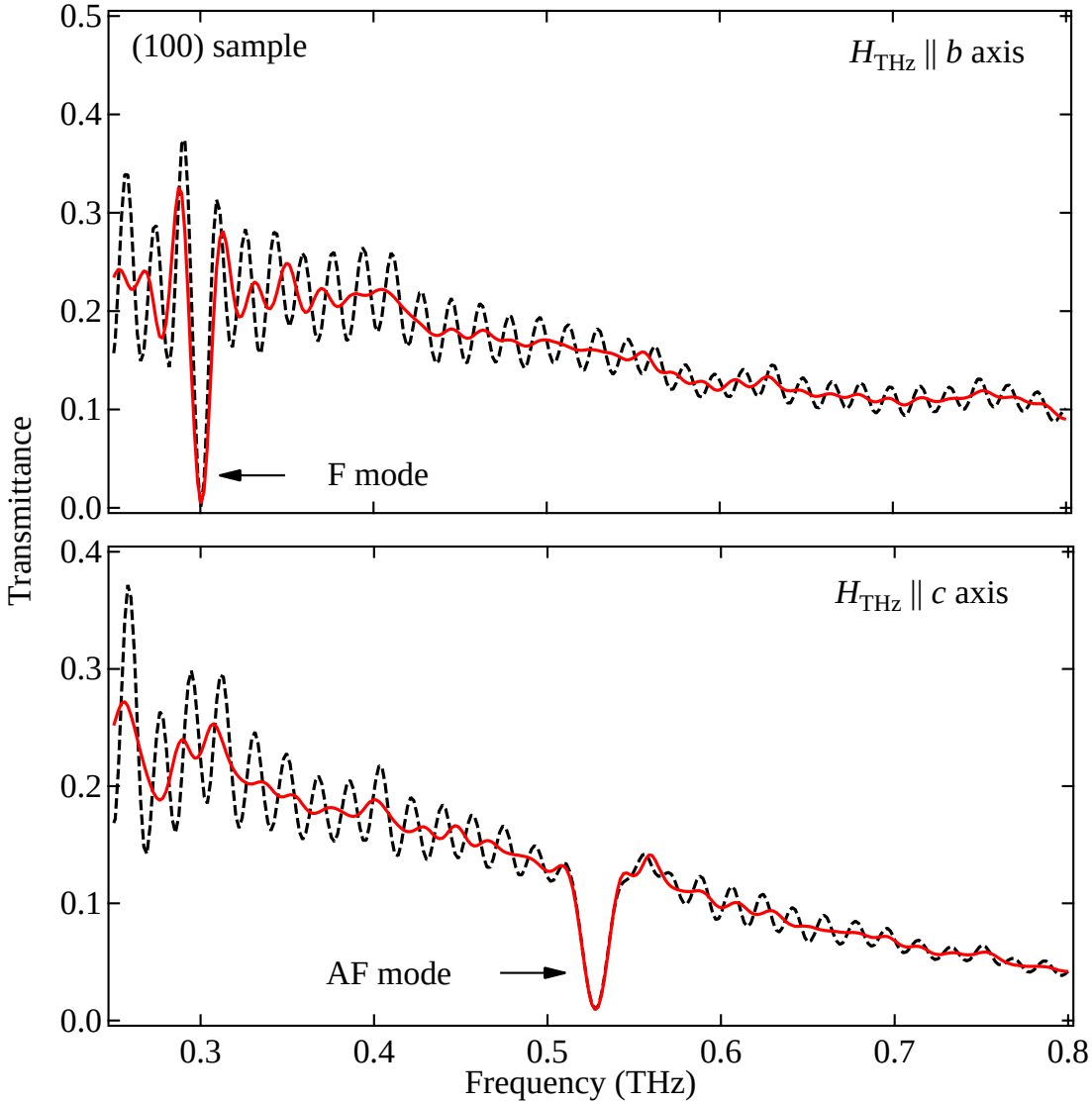

FIG. 4.3 THz transmittance spectra of (100) $YFeO_3$ sample obtained from Fourier transformation of temporal waveforms in Fig.4.1

the reference pulse is due to high refractive index of the $YFeO_3$ single crystal. As the fact that the amount of the delay from the reference depends on the polarization of the THz pulse shows, $YFeO_3$ is a birefringent substance. The refractive index derived from this experiment for THz wave with its electric field component parallel to each axes are $n_a = 4.9$, $n_b = 4.6$, and $n_c = 5.1$. Owing to this high refractive index, THz reflection at the surface of the samples are also quite large and replica of the THz main pulse due to the multiple reflection inside the sample can be observed at around 80 ps in Fig.4.1.

It is also worth noting that by computing the Fourier spectra of the temporal waveforms in Fig.4.1, transmittance spectra shown in Fig.4.3 can be obtained. The black dashed lines show the Fourier spectra calculated with the whole time range shown in Fig.4.1. The existence of the multiple reflection gives rise to the periodical fringes in the spectra. The red solid lines show the spectra computed without the multiple reflection and most of the fringes no longer exist. Beside the fringes, quite narrow dips can be seen. The central frequencies of the dips are equivalent to the resonant frequencies of the excited magnetic resonance modes: 0.299 THz for $H_{THz} \parallel b$ and 0.53 THz for $H_{THz} \parallel c$. This fact maintains that the impulsive excitation of the coherent spin precession with the THz magnetic field can also be interpreted as the absorption of THz electromagnetic waves due to the magnetic resonance modes in the THz region.

4.1.2 Observation of Elliptic Emission from the F Mode Resonance

As stated in chapter 2, the F mode resonance of an orthoferrite can be viewed as an elliptic precession motion of the macroscopic magnetization. In the case of $YFeO_3$, this motion takes place inside the (001) plane. Therefore, when exciting the spins in (001) sample with a THz pulse, FID emission can also be observed in the perpendicular polarization. As a total, FID emission with elliptic polarization is expected to be observed.

The result of the measurement performed for confirming this is shown in Fig.4.4. The (001) sample was excited with THz pulse with $H_{THz} \parallel a$ axis polarization. The perpendicular polarization was measured by subtracting the -45 degree polarization signal from the +45 degree polarization signal. Here, static external magnetic field of approximately 0.1 T was applied along the c axis of the sample (Faraday configuration) in order to remove the magnetic domain structure of the sample. Without lining up the magnetic domains uniformly, FID emission in the perpendicular polarization from the domains with the macroscopic magnetization toward [001] direction cancels out with that of the domains with $[00\bar{1}]$ macroscopic magnetization.

The perpendicular polarization in Fig.4.4 shows oscillation due to the FID emission which is similar to the emission in the parallel polarization. The largest difference between the two polarization is that the THz main pulse does not overlap with the FID signal at the time

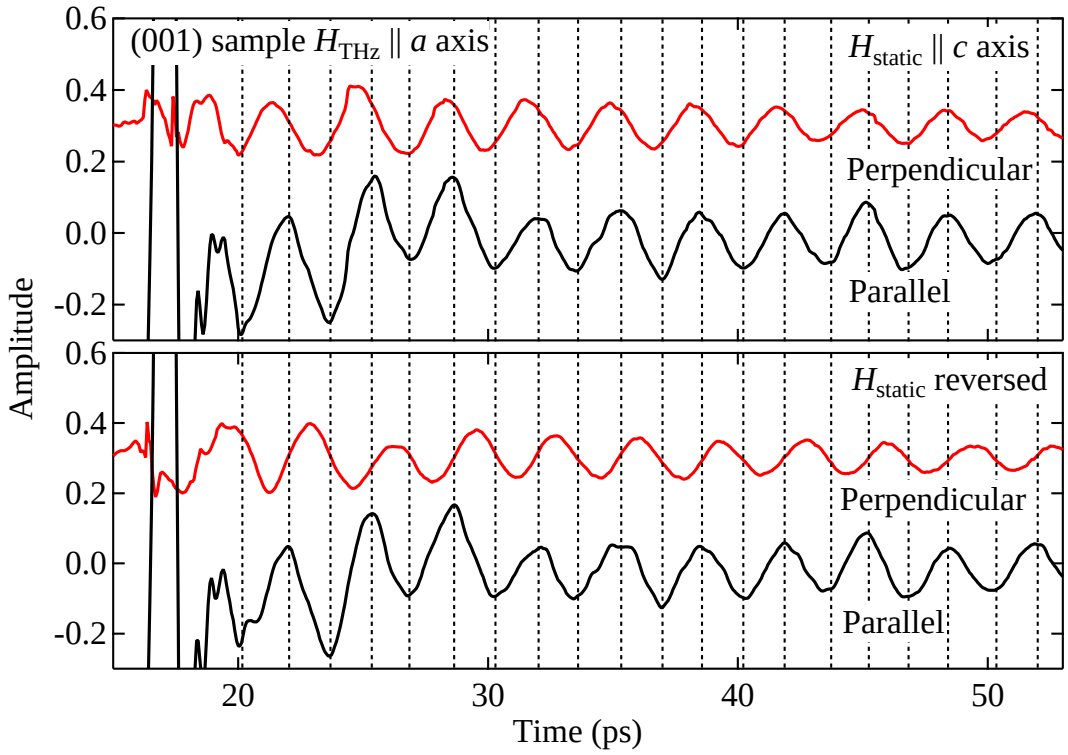

FIG. 4.4 The temporal waveform of THz-TDS with (001) $YFeO_3$ sample in the perpendicular polarization and parallel polarization. A static magnetic field is applied along c axis in order to remove the magnetic domain structure.

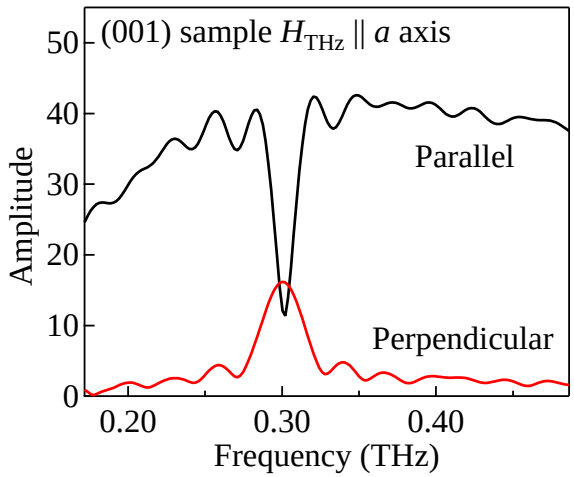

FIG. 4.5 The Fourier spectra of the transmitted THz waveforms in Fig.4.4

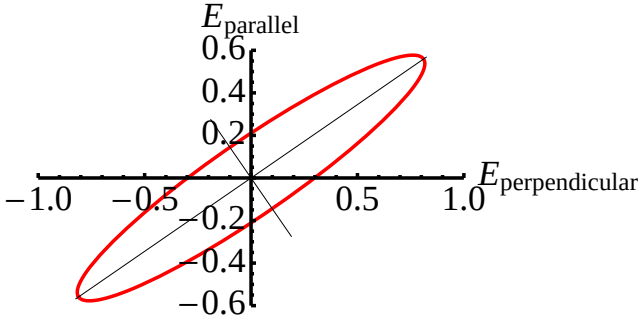

FIG. 4.6 Two dimensional trajectory of the emission from (001) $YFeO_3$ sample with $\omega = \omega_F$.

origin. The spectra in Fig.4.5 shows that the perpendicular polarization possesses a peak at the resonant frequency of the F mode resonance and this supports the interpretation that the oscillation in this polarization is also FID signal of the precessing magnetization.

It should be pointed out that the phase difference of the two polarization is not precisely $\pi/2$. Figure 4.6 shows the two dimensional trajectory of the FID emission calculated by using the ellipticity and the principal axis direction of this signal at $\omega = \omega_F$. The ellipticity η and the angle α of the long axis with respect to the incident polarization can be computed in the following procedure. First, the electric field component of the signal at frequency ω can be represented as

$$\begin{pmatrix} E_{Parallel}(\omega) \\ E_{Perpedicular}(\omega) \end{pmatrix} = \begin{pmatrix} a\cos(\omega t + \delta_1(\omega)) \\ b\cos(\omega t + \delta_2(\omega)) \end{pmatrix}, \tag{4.1}$$

where a and b is the amplitude and δ_i is the initial phase. Using this expression, η and α can be calculated from [34]

$$\eta = \tan\left(\frac{1}{2}\sin^{-1}\left(\frac{2ab\sin(\delta_2 - \delta_1)}{a^2 + b^2}\right)\right) \tag{4.2}$$

$$\alpha = \frac{1}{2}\tan^{-1}\left(\frac{2ab\cos(\delta_2 - \delta_1)}{b^2 - a^2}\right) \tag{4.3}$$

The trajectory in Fig.4.6 shows that the FID emission is highly elliptic and the principal axis deviates largely from the parallel polarization. While the ellipticity can be attributed to the elliptic nature of the precession of the F mode resonance which was explained in chapter 2, the rotation of the principal axis is mainly due to the birefringence of the single crystal.

When the direction of the dominant magnetic domain is reversed by changing the direction of the static magnetic field, the helicity of the elliptic emission is expected to be reversed.

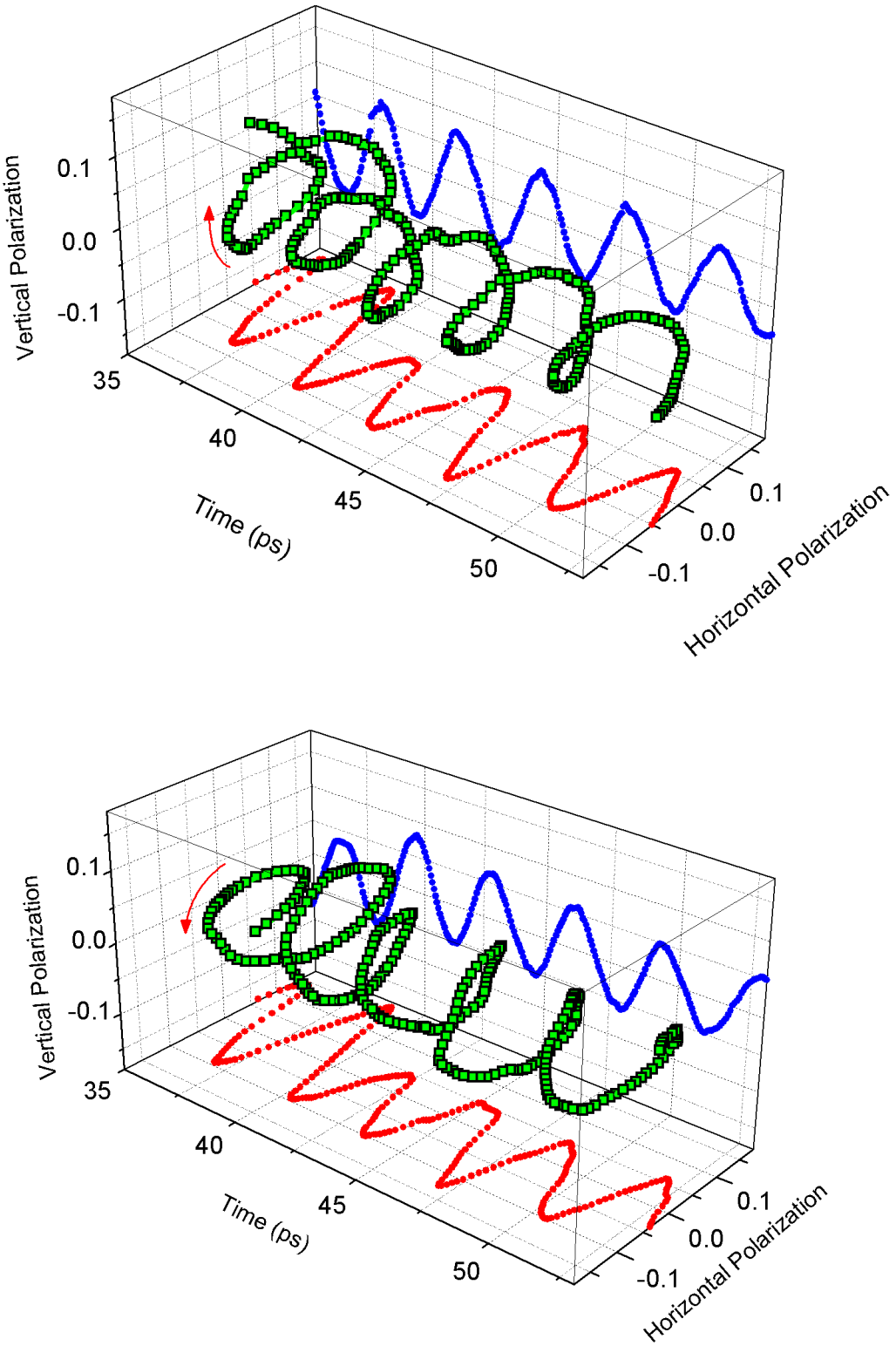

FIG. 4.7 Three dimensional plot of the waveforms in Fig. 4.4. The emission from the F mode resonance is observed as elliptic radiation. Inversion of the helicity of the elliptic emission owing to the reversed magnetic poles can also be seen.

In Fig.4.4, it can be seen that the phase of the oscillation in the perpendicular polarization is reversed when the static magnetic field is applied to the opposite direction. By plotting these FID signal data as three dimensional plot, the helicity inversion of the emitted FID signal due to reversed magnetic domains is clearly observed (Fig.4.7). For the ease to see, the phase shift owing to the birefringence was compensated in this figure with a phase offset of -0.34π in the the perpendicular polarization. The amount of the offset was estimated from the thickness of the sample and the difference of the refractive indices between the two polarizations.

4.2 Coherent Control of Spin Precession with THz Double Pulse

4.2.1 Background

Owing to the rapid advancements in the femtosecond laser spectroscopy, numbers of researches on coherent control of oscillations in quantum mechanical systems have been reported. Real time dynamical behaviors of the coherent control have been observed with various targets including nuclear wave packets in molecules, electronic wave packets in atoms [56], and elementary excitations in condensed matter such as phonons [57–59], excitons [60], and magnons [16–19, 26, 29]. Not only these researches provide a deeper understanding of the wave nature of matter and realize an otherwise unattainable state of matter, coherent control has a potential to play an important role in applications such as information processing and storage mediated by quantum systems [56].

Commonly, phonon system is selected as a target for the coherent control experiments. The so-called coherent phonon experiment is conducted by a pair of the femtosecond laser pulses. The first pulse is used to excite the coherent oscillation of the phonons. The second laser pulse which is temporally delayed with respect to the first pulse is used to control the coherent oscillation excited by the previous pulse. The oscillation can be either completely cancelled or amplified twice the initial amplitude, depending on the time interval of the two pulses [57–59]. Coherent control of spin precessions can be performed in this fashion as well. In these coherent control experiments, there still remains a discussion whether they are really coherent manipulation of the oscillator rather than superposition of the two separately

excited states with inverted phases [19].

The most straight forward way to determine the correct answer for this question is to examine the behavior of the second excitation pulse. For example, if the double pulse excitation of the oscillation is truly a coherent phenomenon, when the oscillations caused by the two pulses interact destructively, energy given from the first pulse to the oscillator is expected to be transferred back to the second pumping pulse. However, experimental proofs for such energy conservation between photons and elementary excitations has not been reported for a long time. This is because in the preceding experiments with visible light, the energy incident on the sample is many orders of magnitude larger than that stored in the elementary excitation system. For this reason, even if the energy transfer from the elementary excitation to the incident light pulse exists, significant change in the exciting pulse may not be observed. In addition, observation of energy conservation is not guaranteed in the coherent control experiment which incorporates intermediate excitation such as electronic excitation. In such cases, although the energy of the coherent oscillation may be returned to the electron system, the excited electrons do not necessarily transfer their energy back to the incident light pulse owing to the existence of the additional energy dissipation channels. To sum up, in order to observe the energy transfer from the coherent oscillation to the excitation light pulse, selection of the appropriate elementary excitation which interacts directly with the incident excitation pulse is required. Since precession motions of the spins in this study are excited and monitored through the THz waves coupled directly with the magnetic moments in the sample, insight into the conservation of energy is expected to be obtained.

In this section, for the purpose of demonstrating THz pulse excited coherent control of spins, double pulse excitation of the precession motion of the spins in a single crystal $YFeO_3$ is performed. The experiment conducted here also aimed to obtain the proof of the energy transfer between the spin system and the THz photon system. The coherent control method used in this section is not limited to spin precessions and application of the method to other types of coherent oscillations such as coherent phonons is expected to be possible. Part of the results shown here are published in references [61, 62]. In addition, roughly at the same time, a similar experiment on antiferromagnet NiO [63] was reported by Kampfrath *et al*.

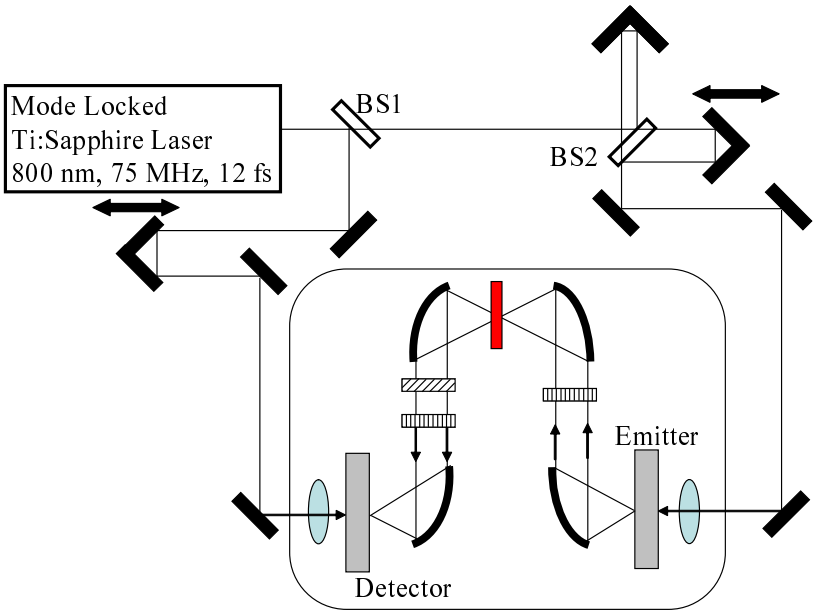

FIG. 4.8 Double pulse THz TDS system with Michelson-type interferometer.

4.2.2 Experimental Setup

As in the previous section, the Transmission type THz-TDS measurements at room temperature were conducted with dipole type photoconductive antennas. The following two methods that temporally divide the pumping visible pulse of the emitter antenna were tested for preparing the double THz pulses required for the coherent control of the spins.

The first method is to separate the two pulses by spatially splitting the pumping laser beam in its cross section with a pair of hemicircular shaped mirrors. The pair of mirrors was put with their edge close together and the laser beam was reflected in the proximity of these edges so each mirror reflects some portion of the incoming laser beam. The time delay between the two pulses was adjusted by moving one of the two mirrors back and forth. By changing the cross sectional area of the laser reflected by each mirror, amplitude ratio between the two pulses was adjusted.

The alternative way to prepare the THz double pulse is to separate the pumping pulse with Michelson-type interferometer. This is described in Fig.4.8. The above two methods did not show any significant difference in the result of this experiment.

As the samples, [001] plane sample and [100] plane samples were used. All of the experi-

ments discussed in this section were performed at room temperature.

4.2.3 Result and Discussion

Using the [001] sample of $YFeO_3$ single crystal as a target, double pulse coherent control of the F mode resonance was conducted. The sample was set so that electric and magnetic field components of the THz pulse is along the *b* axis and *a* axis, respectively. As explained before, to remove the domain structure inside the sample, static external magnetic field of approximately 0.1 T was applied perpendicular to the sample surface.

The result of this measurement is shown in Figs.4.9 and 4.10. In these figures, temporal waveforms with double pulse temporal separation $4T_F \leq \Delta t \leq 4.5T_F$ (T_F=3.3 ps is the temporal period of the F mode reosonance) is compared with the result of the single pulse excitation experiment. It can be recognized from the figure that when the second pulse excitation takes place at $\Delta t = 4T_F$, the FID amplitude which follows the second pulse is enhanced compared to that of the single pulse excitation. As the time separation Δt increases, the oscillation excited by the two pulses starts to decrease. When the time separation $\Delta t = 4.5T_F$, the oscillation amplitude is minimized. These behaviors are observed not only in the parallel polarization but also in the perpendicular polarization which proves that the precession of the spins are coherently controlled with THz double pulse. Here, the amplitude ratio of the two THz pulses were selected so that the oscillation in $\Delta t = 4T_F$ condition becomes roughly the twice the value of the oscillation generated with single pulse excitation.

Figure 4.11 shows the intensity of the peak at 0.299 THz obtained from Fourier transformation of the oscillation after the second pulse excitation at various Δt (time window from 18 ps to 43 ps in Figs.4.9 and 4.10). These intensity values are normalized by the intensity of the emission obtained with single pulse excitation within the same time window. It can be seen that as the time separation of the two pulses Δt changes, the intensity of the resultant emission changes continuously. The local maximum of the emission is at $\Delta t = 4T_F$ and $5T_F$, and approximately fourfold increase of the emission with respect to the single pulse excitation is observed. The local minimum on the other hand exists at $\Delta t = 4.5T_F$ and in this case, the F mode emission is annihilated. FID emission after double THz pulse excitation computed with the LLG equation also shows similar dependence on the time separation Δt (the theoretical

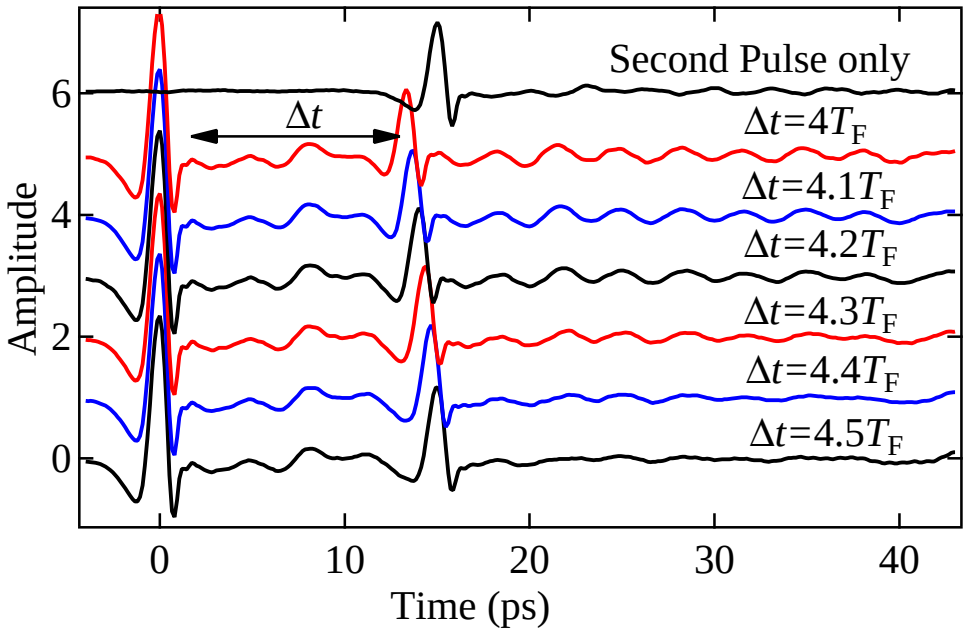

FIG. 4.9 Parallel polarization temporal waveforms of transmitted THz wave through (001) sample of $YFeO_3$. The F mode resonance precession of the spins excited by the $H_{THz} \parallel a$ axis is coherently controlled by the second THz pulse. The value Δt denotes the time separation between the two pulses.

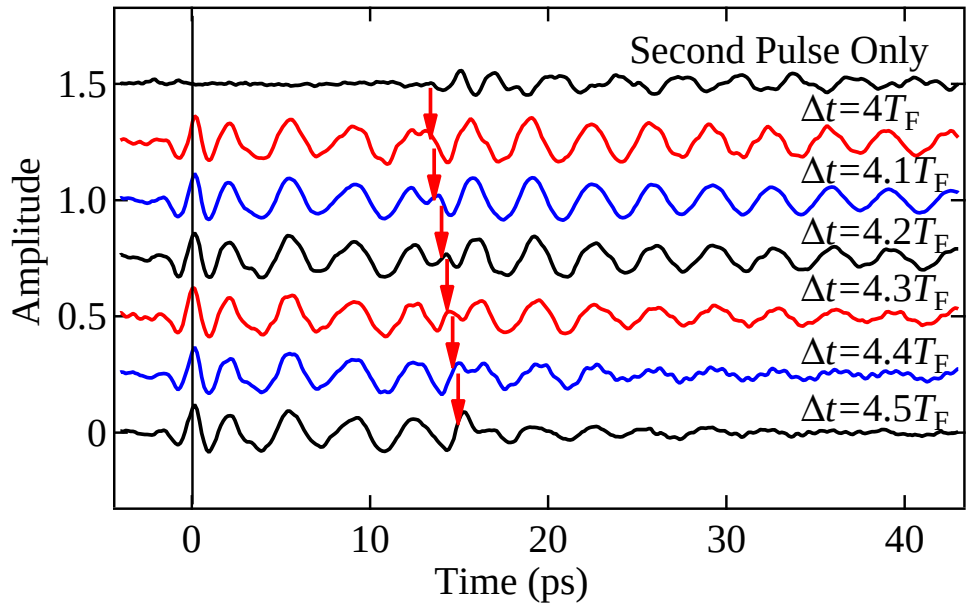

FIG. 4.10 Perpendicular polarization temporal waveforms of transmitted THz wave through (001) sample of $YFeO_3$. The arrows in the figure show the point of time when the second pulse excitation occurs.

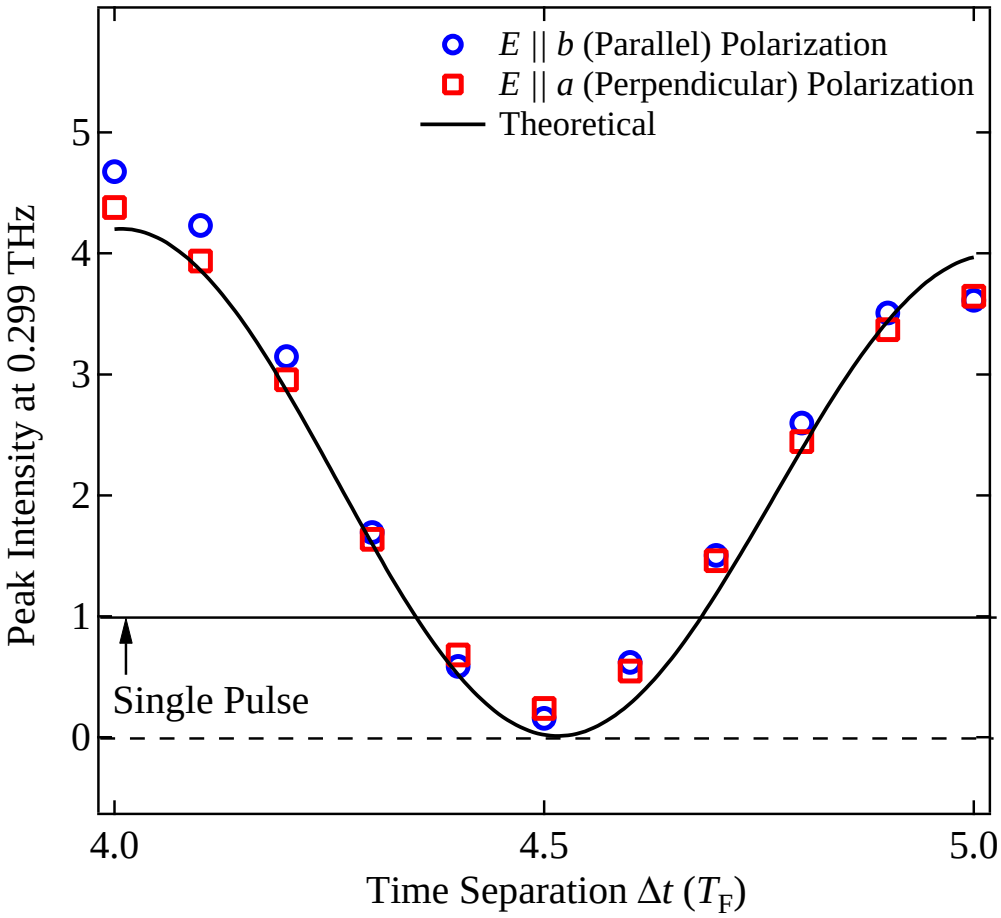

FIG. 4.11 Normalized intensity at 0.299 THz peak obtained by Fourier transformation of the temporal waveforms in $YFeO_3$ after the second THz pulse for various double pulse time separation Δt. The time window of the Fourier transformation is from 18 ps to 43 ps in Figs.4.9 and 4.10.

curve in Fig.4.11). These results match with the result of coherent phonon experiment where maximum amplification of the oscillation can be obtained when Δt is integer multiple of the oscillation period, and complete annihilation can be obtained when Δt is half integer multiple of the oscillation period [57–59]. Note that these amplification and attenuation of the spin precession is not limited to double pulse with time separation between $\Delta t = 4T_F$ and $5T_F$. Similar behavior can also be observed with arbitrary time separation as long as the oscillation excited by the first pulse persists.

Although the amplitude of the oscillation in $\Delta t = 4.5T_F$ is the minimum value, waveforms in Figs. 4.9 and 4.10 show that some portion of the oscillation still exist. This can be attributed to the imprecise choice of the second pulse amplitude. Figure 4.12 shows the improved

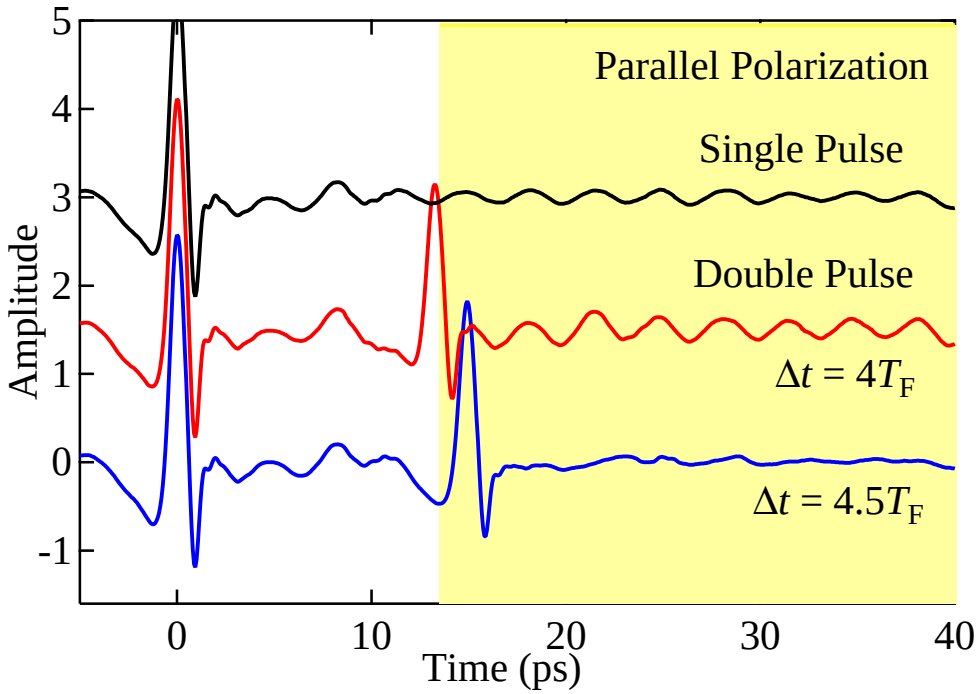

FIG. 4.12 Temporal waveforms of transmitted THz wave through (001) sample of $YFeO_3$. The amplitude ratio between the two pulses are optimized so that the oscillatory component in$\Delta t = 4.5T_F$ completely vanishes.

result of double pulse excitation experiment where the second pulse amplitude was precisely selected so that the oscillation after the second pulse becomes as small as possible.

Next, we will focus on the energy transfer between the THz pulse and the spin system which is expected to take place when the THz pulse instantaneously excites the spins. When the incident THz pulse excites the precession, the energy of the impulsive magnetic field is transferred to the spins. This causes the amplitude of the THz pulse to decrease. In an analogous manner, when the THz pulse interacts with the spins and stops the precession motion, then the energy which would have been consumed as FID emission should be returned to the THz pulse.

A closer inspection of the second THz pulse main peak reveals that the peak amplitude is actually larger for $\Delta t = 4.5T_F$ condition than $\Delta t = 4T_F$ condition (Fig.4.13). This result is consistent with the prediction that the THz pulse used for stopping the spin precession should receive energy from the spin system. Although the peak difference between the two conditions in Fig.4.13 may seem small compared to the amplified spin precession observed

in the $\Delta t = 4T_F$ condition, when viewed in the perspective of the intensity, the difference is quite large. To be specific, the peak intensity value of the second THz pulse for $\Delta t = 4T_F$ and $\Delta t = 4.5T_F$ are approximately 2.7 and 3.3, respectively. The FWHM of these two pulses are slightly different: 0.56 ps for $\Delta t = 4T_F$ and 0.6 ps for $\Delta t = 4T_F$. Therefore, the total energy of the second pulse peaks are $2.7 \times 0.56 = 1.512$ ($\Delta t = 4T_F$) and $3.3 \times 0.6 = 1.98$ ($\Delta t = 4.5T_F$). Hereafter, the total energy of the second pulse at $\Delta t = 4T_F$ will be referred to as $U_{2\mathrm{nd}}$. The above calculation shows that the total energy of the second main pulse in the $\Delta t = 4.5T_F$ condition is approximately 1.3 times larger than $U_{2\mathrm{nd}}$. It can be interpreted that second THz pulse at $\Delta t = 4.5T_F$ received energy equivalent to 30 % of $U_{2\mathrm{nd}}$ from the spin system.

On the other hand, the FID emission is calculated as follows. The amplitude of the FID emission in the parallel polarization right after the second pulse excitation in $\Delta t = 4T_F$ condition is 0.175. The FID energy per half cycle can be calculated by (effective value)$^2 \times T_F/2$. Since the relaxation time of the precession amplitude in this condition was 35 ps, the FID intensity becomes $1/e$ in 17.5 ps, meaning that there are about 10.6 half cycles before the precession decays. Therefore, the total FID energy in the parallel polarization is $\left(0.175/\sqrt{2}\right)^2 \times 3.3\mathrm{ps}/2 \times 10.6 = 0.268$. The FID energy in the perpendicular polarization can be calculated in the same manner and since the intensity of the FID emission in the perpendicular polarization was about half of the FID intensity in the parallel polarization, the total FID energy in $\Delta t = 4T_F$ condition is $0.268 \times 1.5 = 0.402$. This is equivalent to approximately 26.6 % of the THz second pulse total energy in $\Delta t = 4T_F$, $U_{2\mathrm{nd}}$. Since no FID emission remains after the second pulse excitation at $\Delta t = 4.5T_F$, the total FID energy calculated here is the difference of the total FID emission energy between the two cases.

Comparing these two calculated values, it can be seen that the amount of energy collected by the THz pulse at $\Delta t = 4.5T_F$ is comparable to the amount of energy emitted gradually as the FID emission after second pulse excitation at $\Delta t = 4T_F$. Therefore, it was confirmed that the THz pulse actually takes away the energy from the spin system when the spin precession is coherently cancelled.

The method of double pulse coherent control can also be applied for selectively exciting a specific mode of oscillation when more than one mode exists. An example of such experiment

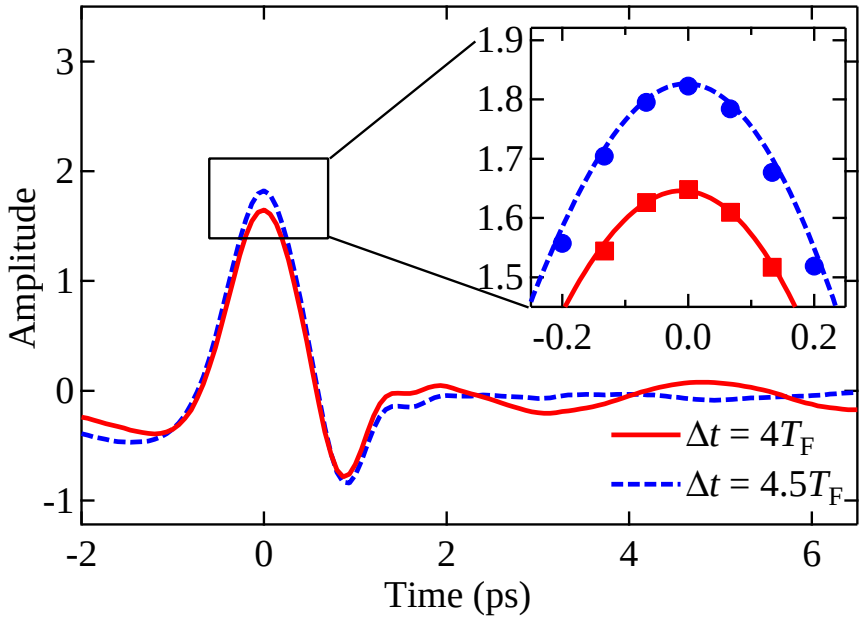

FIG. 4.13 Main peak of the second THz pulses transmitted through $YFeO_3$ in $\Delta t = 4T_F$ and $\Delta t = 4.5T_F$ condition. The inset shows the magnified curves near the peak value of the pulses.

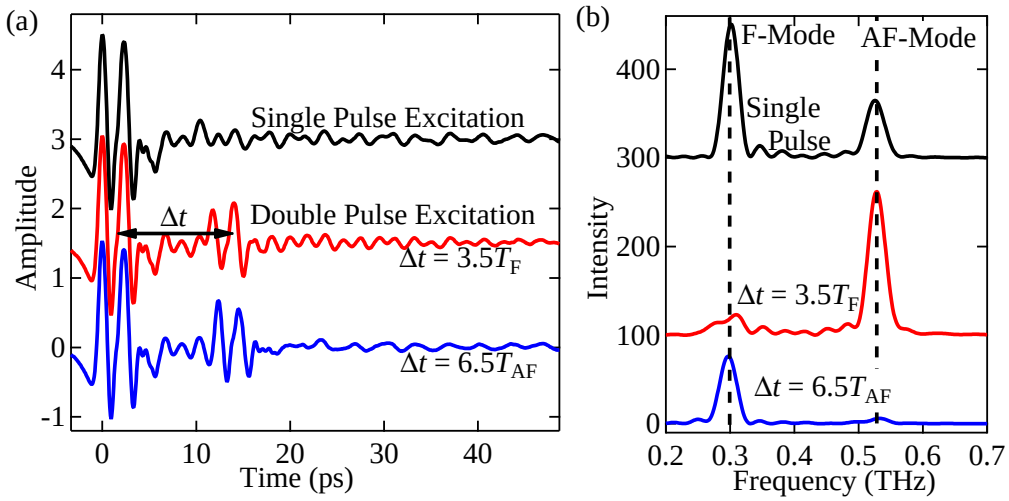

FIG. 4.14 (a) Temporal waveforms of double pulse THz-TDS with (100) plane single crystal $YFeO_3$. The sample was set so that the angle between the H_{THz} and the b axis (and c axis) is 45°. (b) Fourier spectra of the oscillatory components in Fig.4.14(a). The time window from 18 to 48 ps was used.

is demonstrated in Fig.4.14. Here, the orientation of the (100) sample of $YFeO_3$ was selected so that the angle between the THz magnetic field component and the b axis is 45°. In this configuration, single pulse excitation results in excitation of both the F mode and AF mode resonance. Because two types of oscillation exist, the temporal waveform in Fig.4.14(a) shows rather complicated oscillation which follows the THz main peak temporally split due to the birefringence between b axis and c axis. The Fourier spectrum of this oscillation in Fig.4.14(b) reveals that this complicated oscillation is a superposition of the oscillations with frequency of 0.299 THz (F mode) and 0.53 THz (AF mode). The waveforms in Fig.4.14(a) labeled $\Delta t = 3.5T_F (= 6.08T_{AF})$ and $\Delta t = 6.5T_{AF} (= 3.74T_F)$ were obtained by double pulse excitation with time separation of Δt. $T_{AF} = 1.9$ ps is the oscillation period of the AF mode resonance. Here, the double pulse separation was carefully selected so that one of the two modes cancels out completely while the other mode remains to some extent. The FID signals after the double pulse excitation obviously have different appearance compared to that of the single pulse excitation. As it can be observed from the Fourier spectra, F mode resonance is cancelled and only the AF mode oscillation remains when the double pulse time separation is $\Delta t = 3.5T_F$ (Fig.4.14). On the other hand, when the time separation is $\Delta = 6.5T_{AF}$, only the AF mode peak disappears.

Another example of double pulse selective excitation method is shown in Fig.4.15. Here, sintered pellet sample of $ErFeO_3$ is excited with THz pulses. Since the pellet sample is composed of randomly oriented micro crystals, the resonance modes excited by the THz pulse is independent of the polarization. Therefore, the single pulse THz excites both the F mode (0.377 THz) and AF mode (0.673 THz) resonance (Figs. 4.15 (a) and (b)). For this reason, even if the sample is magnetized perpendicular to its surface by an external magnetic field, elliptic emission from F mode resonance is obscured by the coexisting AF mode emission in the parallel polarization (Fig.4.16(a)). However, since as shown in Fig.4.15, the AF mode and F mode can be selectively cancelled by the double pulse excitation method, this obscuring AF mode can be annihilated. By employing the double pulse excitation in order to cancel the AF mode oscillation, the elliptic nature of the remaining F mode resonance emission is clearly resolved in the three dimensional plot (Fig4.16(b)).

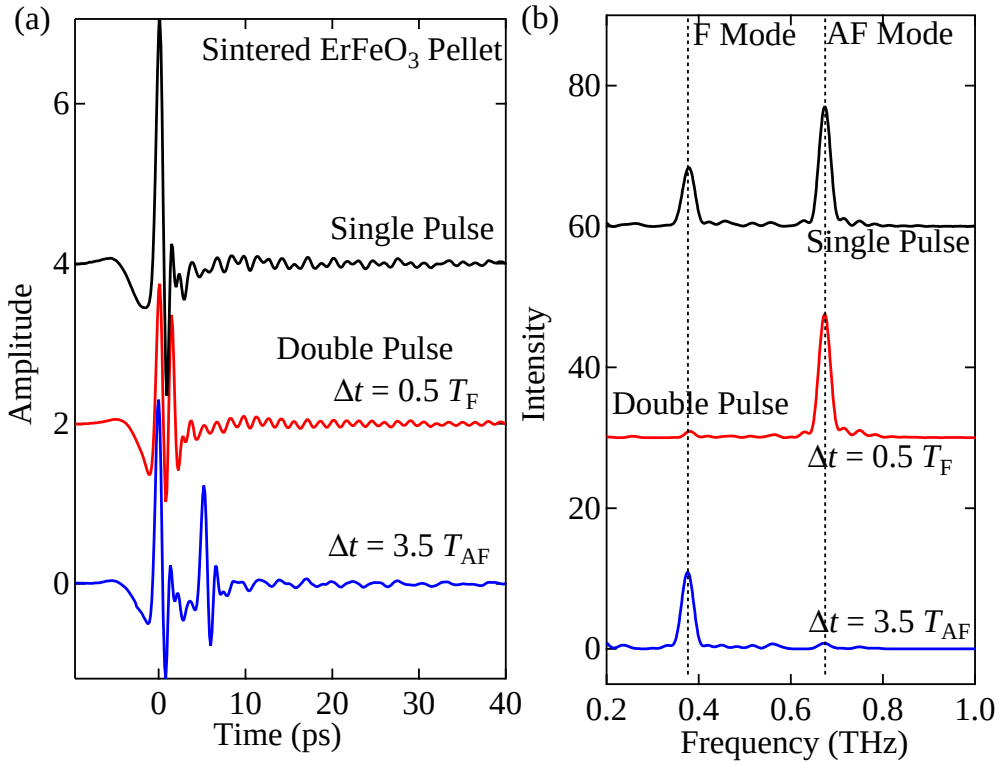

FIG. 4.15 (a) Temporal waveforms of double pulse THz-TDS with a sintered $ErFeO_3$ pellet sample. (b) Fourier spectra of the oscillatory components in Fig.4.15(a). The time window from 10 to 40 ps was used.

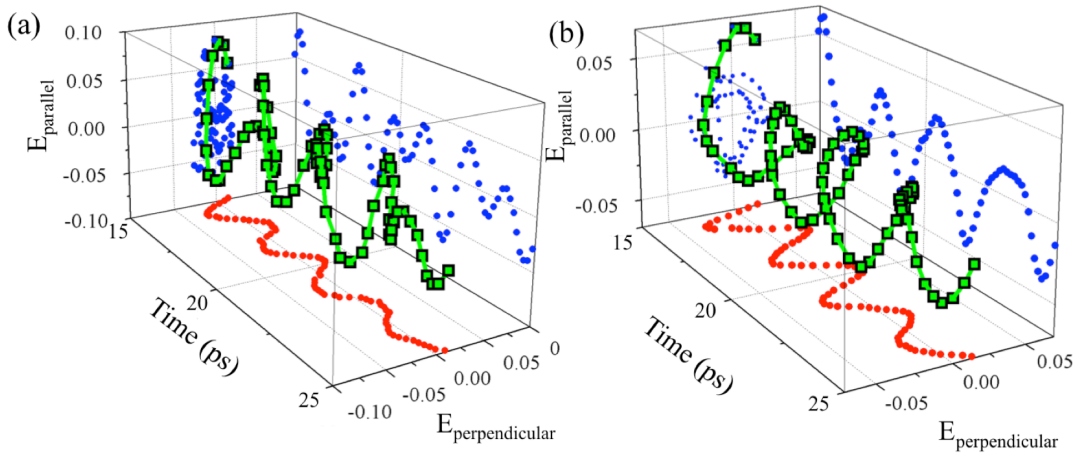

FIG. 4.16 (a) Three dimensional plot of FID emission obtained from single pulse THz excitation of a sintered pellet $ErFeO_3$ sample. (b) FID emission from double pulse excitation of a pellet. The double pulse separation is chosen so that the AF mode emission is selectively cancelled.

Chapter5

Observation of the Spin Reorientation Phase Transition with THz-TDS

5.1 Background

Some orthoferrites are known to show temperature induced phase transition which results in 90 degree rotation of the easy axis of the Fe^{3+} spins. This phase transition is called spin reorientation and many researches on this subject has been conducted.

Recently, studies on femtosecond laser induced ultrafast spin reorientation have been reported [20, 25, 26, 30]. To the best of the author's knowledge, an observation of the spin reorientation transition with the THz-TDS method has not been reported prior to our research. In this chapter, a novel method which employs THz-TDS method for observing spin reorientation is demonstrated. The method introduced here can be applied to detect ultrafast spin reorientation with picosecond time resolution and may be applied for revealing the underlying mechanism of ultrafast reorientation due to inertia driven spin switching and ultrafast heating effect [20, 25, 26, 30]. In addition, because the potential of the Fe^{3+} spins is expected to become substantially unstable near the spin reorientation, it is one of the strong candidates for observing nonlinear behavior with high power THz excitation.

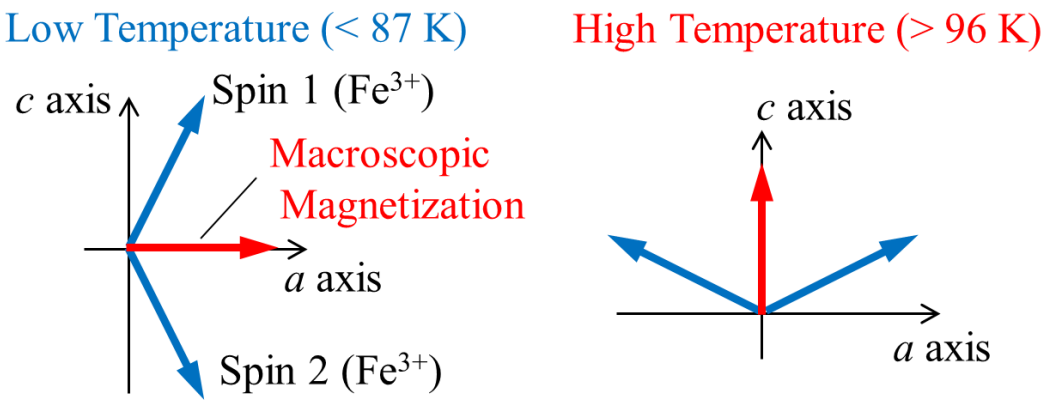

FIG. 5.1 Schematic of Fe^{3+} spin configuration in $ErFeO_3$. The spin configuration is described in a simplified two sublattice representation.

5.2 Spin Reorientation in $ErFeO_3$

Rare-earth orthoferrite $ErFeO_3$ shows spin reorientation transition from high temperature Γ_4 phase to low temperature Γ_2 phase (Fig.5.1). The increase of magnetization of the paramagnetic rare-earth ions due to decrease of thermal energy is known to trigger this phase transition. Due to the effective magnetic field generated by the Fe^{3+} spins, Er^{3+} spins are known to align antiparallel to the weak ferromagnetic moment. In addition to the symmetric exchange, antisymmetric exchange between the rare-earth spins and iron spins exists. This antisymmetric exchange works in a manner where Fe^{3+} sublattice spins are deflected from the a axis to the c axis (increasing the anisotropy A_z and decreasing the anisotropy A_x). When this interaction surpasses that of the Fe^{3+} spins, the equilibrium orientation of the Fe^{3+} spins changes into Γ_2 configuration [47].

For the purpose of observing the spin reorientation transition in $ErFeO_3$, transmission type THz-TDS of $ErFeO_3$ (001) plane single crystal and sintered pellet sample were conducted at various temperature [64]. The thickness of the single crystal sample and pellet sample were approximately 1.3 mm and 1.6 mm, respectively. In order to cool the samples below room temperature, liquid helium was used with a cold finger cryostat (Oxford Instruments). As the windows of the cryostat, a pair of diamond plates or TSURUPICA plates were used.

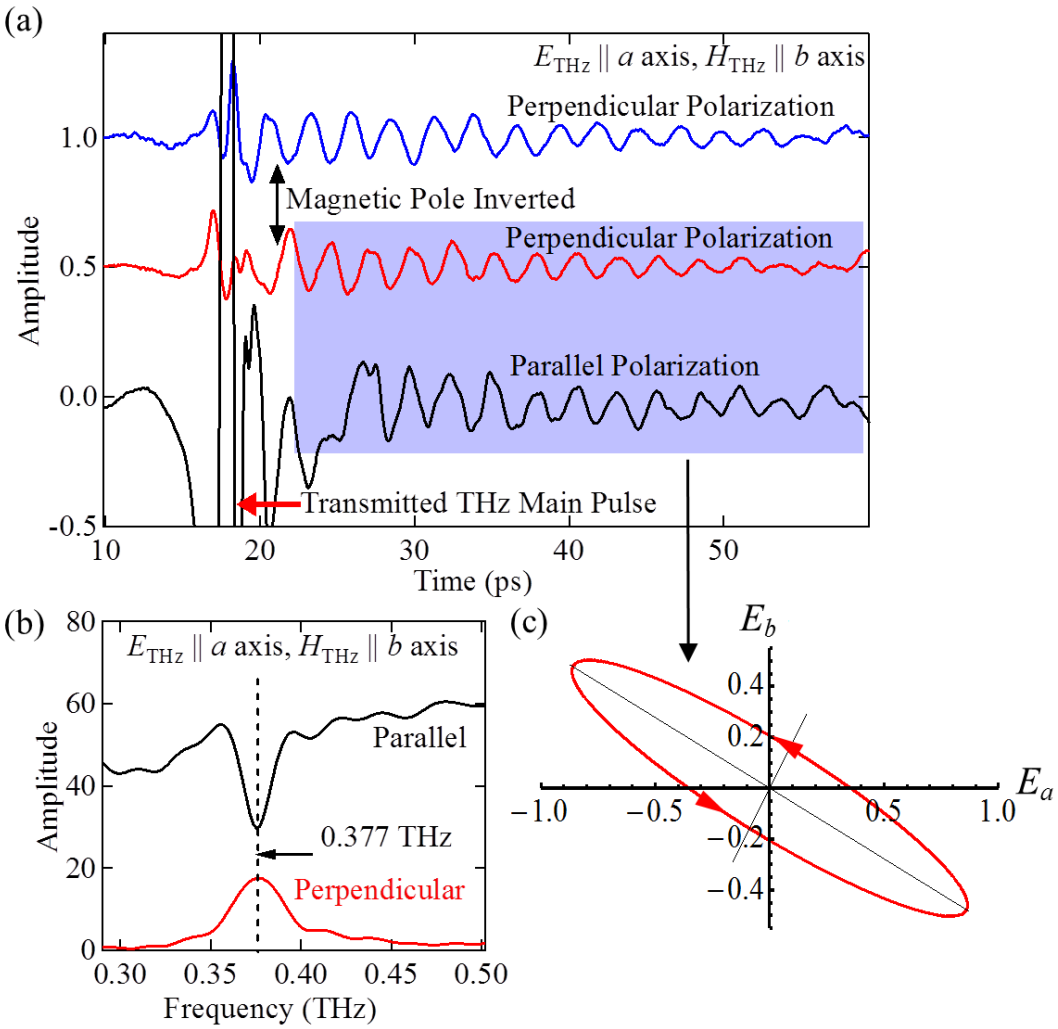

FIG. 5.2 (a) Temporal waveform of transmitted THz wave through (001) single crystal $ErFeO_3$. (b) Fourier spectra of the waveforms in (a). (c) Two dimensional trajectory of the elliptic FID emission at 0.377 THz.

5.2.1 Excitation with THz magnetic Field Component Along *b* axis

Frequency Shift and Polarization Switching

The result of THz-TDS measurement with a (001) $ErFeO_3$ single crystal at room temperature is shown in Fig.5.2. The sample was magnetized along the *c* axis. Similar to the (001) $YFeO_3$ single crystal in the previous chapter, the incident THz pulse excites the F mode antiferromagnetic resonance. The main pulse of the incident THz pulse is followed by the FID emission. Since the magnetic field component of THz pulse parallel to *b* axis excites the

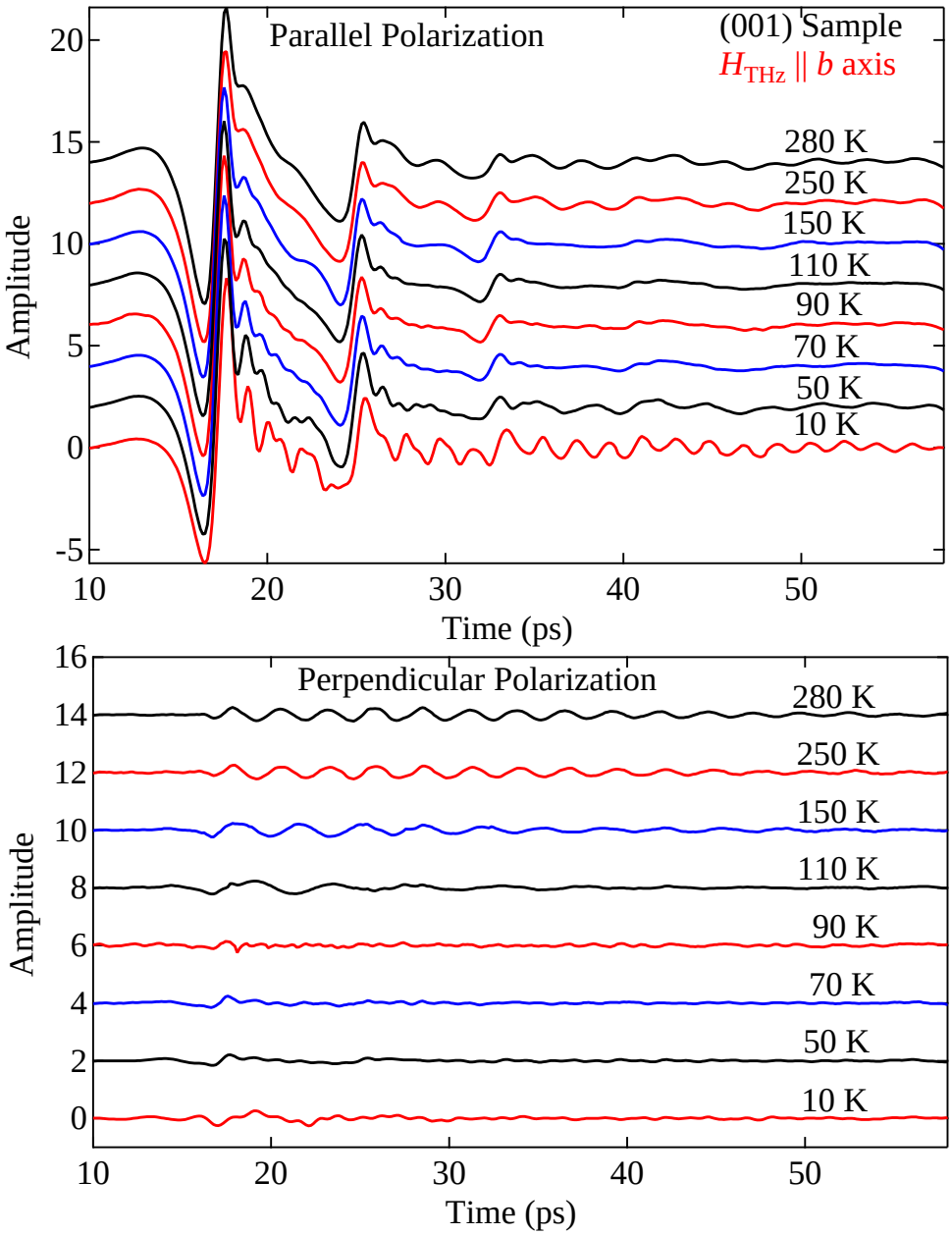

FIG. 5.3 Temperature dependence of THz temporal waveform transmitted from (100) $ErFeO_3$ sample. The polarization of the incident THz pulse is $H_{THz} \parallel b$ axis.

F mode resonance, the oscillation observed here has a frequency equivalent to that of the F mode resonance (0.377 THz). This oscillation is also observed in perpendicular polarization and inversion of the magnetic pole results in inversion of helicity of the FID polarization (Fig.5.2). The trajectory of the elliptic emission is shown in Fig.5.2(c).

Having these basic properties confirmed, temperature dependence of the magnetic reso-

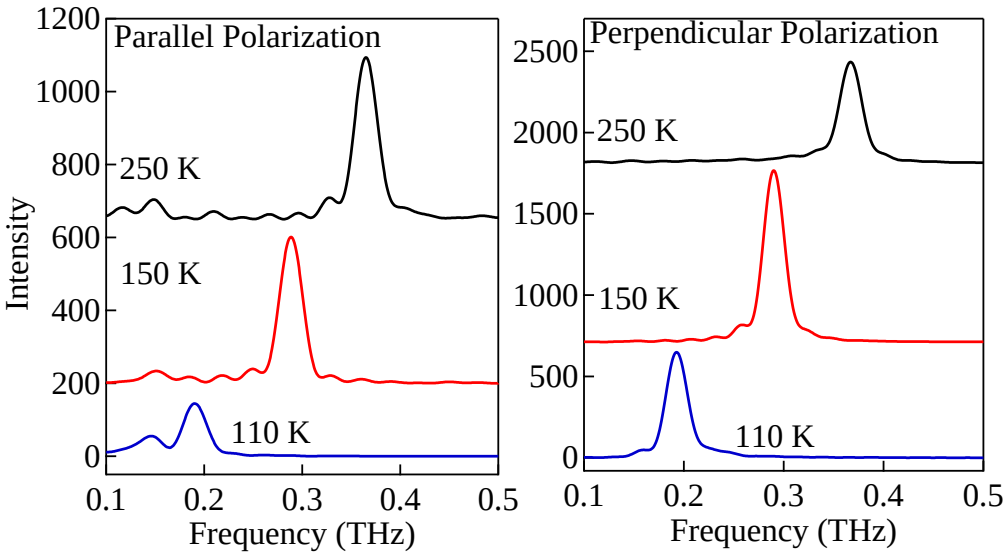

FIG. 5.4 FID emission spectra obtained from $ErFeO_3$ at 250 K, 150 K, and 110 K calculated from data in Fig.5.3

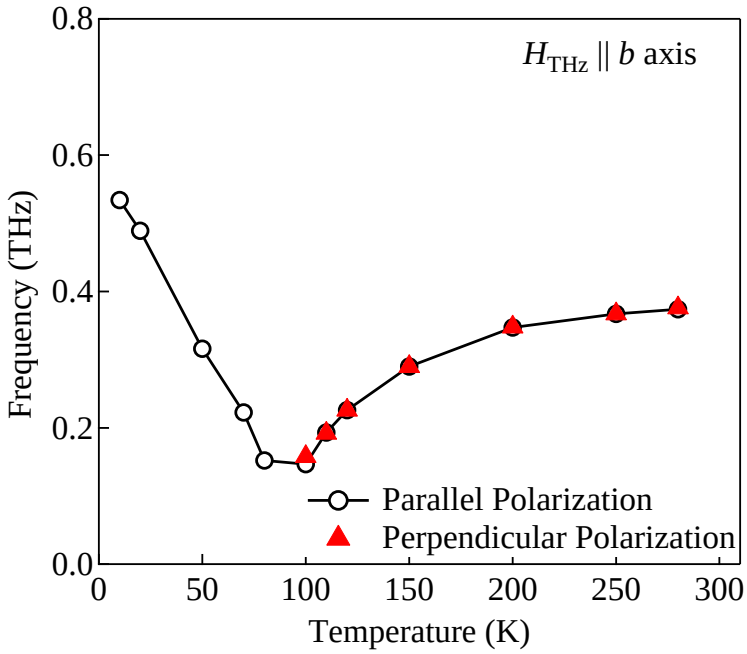

FIG. 5.5 Temperature dependence of FID emission peak frequency for (100) $ErFeO_3$ with $H_{THz} \parallel b$ axis THz pulse.

nance was investigated. Fig.5.3 shows the THz-TDS measurement result with $H_{THz} \parallel b$ axis polarization. As the ambient temperature is lowered from the room temperature to reorientation transition region (around 90 K), the frequency and the amplitude of the FID oscillation becomes smaller. This behavior is observed in both parallel polarization and perpendicular polarization. Due to the presence of the incident THz pulse and its reflected counterparts within the diamond windows of the cryostat, oscillations in 150 K and 110 K are hardly observed. However, the spectra for these temperature show that the oscillation still exist (Fig.5.4).

Cooling the sample further past the transition region, the amplitude of the oscillation in parallel polarization starts to increase. For example, at 50 K, small oscillation with a period of about 3 ps can be observed. By lowering the temperature down to 10 K, the amplitude and the frequency of the FID oscillation becomes larger. Even though such quite strong oscillation exists at 10 K, no such oscillation can be seen in the perpendicular polarization.

Figure 5.5 shows the temperature dependence of the measured FID emission frequency. It can be seen from the figure that when the spin configuration is in the high temperature phase, the frequency of the FID emission decreases as the temperature decreases. On the other hand, in the low temperature spin configuration, decreasing temperature results in increase of the FID emission frequency. Because the frequency changes continuously from the room temperature and no noticeable jump can be observed in the frequency, the FID emission observed in this configuration for both the high and low temperature phase should belong to the F mode antiferromagnetic resonance. The temperature dependence of the resonant frequency matches with the temperature dependence of the F mode expected from equation 2.29 assuming that anisotropy energy $(A_x - A_z)$, which is often regarded to be linearly dependent on the temperature [65, 66], decreases down to zero in the reorientation region. The observed frequency also agrees with the result obtained with the backward wave oscillator experiment [49]. Since the equation of the F mode resonant frequency shows that the frequency takes the minimum value at phase transition region, the transition temperature for this sample seems to exist between 80 K and 100 K. This is consistent with the transition temperature reported in the literatures. Considering the direction of macroscopic magnetization of Fe^{3+} ions (HT: along c axis, LT: along a axis), the incident THz magnetic field $H_{THz} \parallel b$ axis is always perpendicular to the

weak ferromagnetic moment in the whole temperature range. Therefore, the excitation condition that magnetic field pulse perpendicular to the weak ferromagnetic moment excites F mode resonance seems to hold also in the low temperature spin configuration of $ErFeO_3$.

Now that the FID signal in this case is identified as the F mode resonance, the reason why no FID signal is observed in the perpendicular ($H \parallel a$ axis) polarization of the low temperature region can be understood. As mentioned before, the F mode resonance is interpreted as a precession motion of the weak ferromagnetic moment inside the plane perpendicular to the easy axis of the ferromagnetic moment. In the high temperature phase where the macroscopic moment points toward the c axis, this precession takes place inside the a-b plane. Therefore, the F mode resonance generates elliptic FID emission within the a-b plane. On the other hand, when the spin configuration changes to the low temperature phase, the easy axis of the weak ferromagnetic moment is in the a axis direction, which means that FID emission with $H \parallel b$ axis polarization and $H \parallel c$ axis polarization are emitted. Therefore, in the low temperature phase for this experimental configuration, linearly polarized F mode FID emission with $H_{THz} \parallel b$ axis polarization is observed and FID signal cannot be observed in the perpendicular polarization. This relation between the easy axis direction and the polarization of the emitted FID signal for high and low temperature phases are illustrated in Fig.5.6(a). The three dimensional trajectory plot of the waveforms also clearly shows this polarization switching between elliptic polarization and linear polarization (Fig.5.6(b)). Again, the phase shift due to the birefringence of the single crystal was compensated by applying offset of 0.3π in the perpendicular polarization.

These results show that the spin reorientation transition can be detected and the two different phases can be told apart by observing the polarization of the F mode FID emission. This method may be useful since the phase of the sample can be identified without focusing on the temperature dependence of the resonant frequency which requires multiple measurement in wide temperature range. In addition, the possibility of specifying the phase from the existence or non-existence of the emission in the perpendicular polarization means that the phase of the sample can be determined with picosecond order resolution. In the temporal waveforms, two to three cycles of the oscillations at most are sufficient for telling whether the oscillation exists or not. Therefore, this detection method through change of the FID

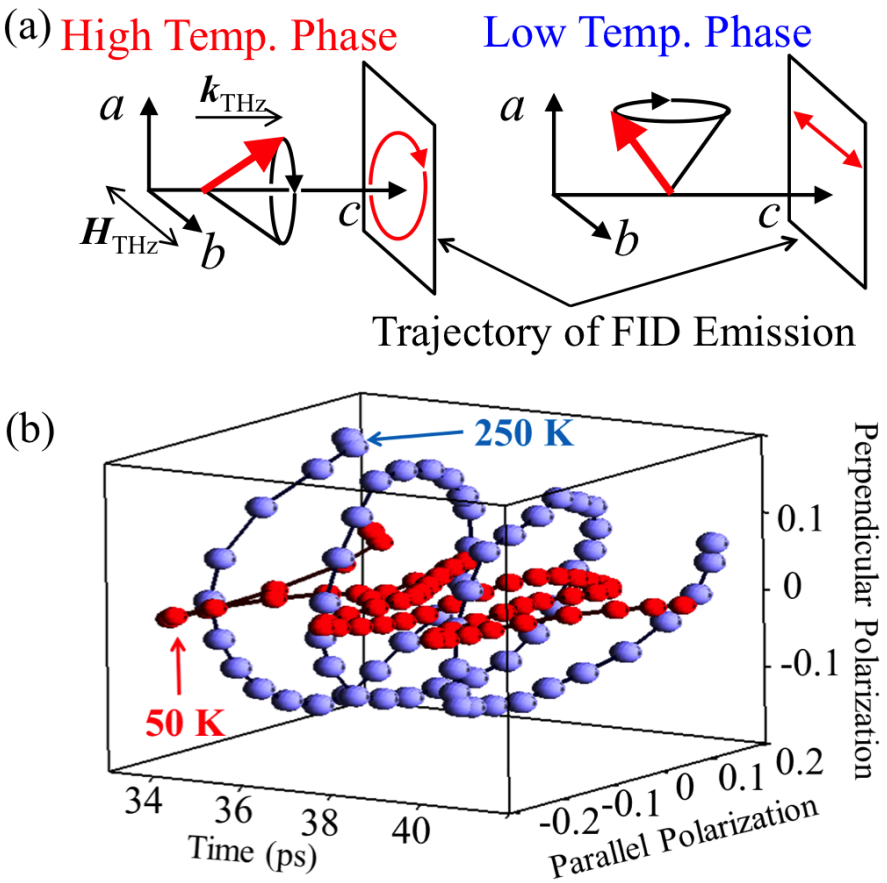

FIG. 5.6 (a) Schematic of spin precession motion and magnetic field component trajectory of F mode FID emission. The change of the spin configuration between the high temperature phase and the low temperature phase results in polarization change of the emission. (c) Three dimensional trajectory of the temporal waveforms obtained with $ErFeO_3$ (001) sample at 250 K (high temperature phase) and 50 K (low temperature phase).

polarization provides an ability to investigate ultrafast spin reorientation transitions.

It should be noted that when this experiment is performed without applying the external static magnetic field, returning the sample's phase from the low temperature phase to high temperature phase resulted in loss of the residual magnetization which existed before cooling the sample. Therefore, to be precise, the low temperature spin configuration of this sample is composed of the magnetic domains with macroscopic magnetization along the $+a$ direction that are described in Fig.5.6(a) and an equivalent number of domains with $-a$ direction magnetization.

Broadening of the F Mode Resonance

As the spectra in Fig.5.4 showed, the intensity of the FID seems to depend on the temper-

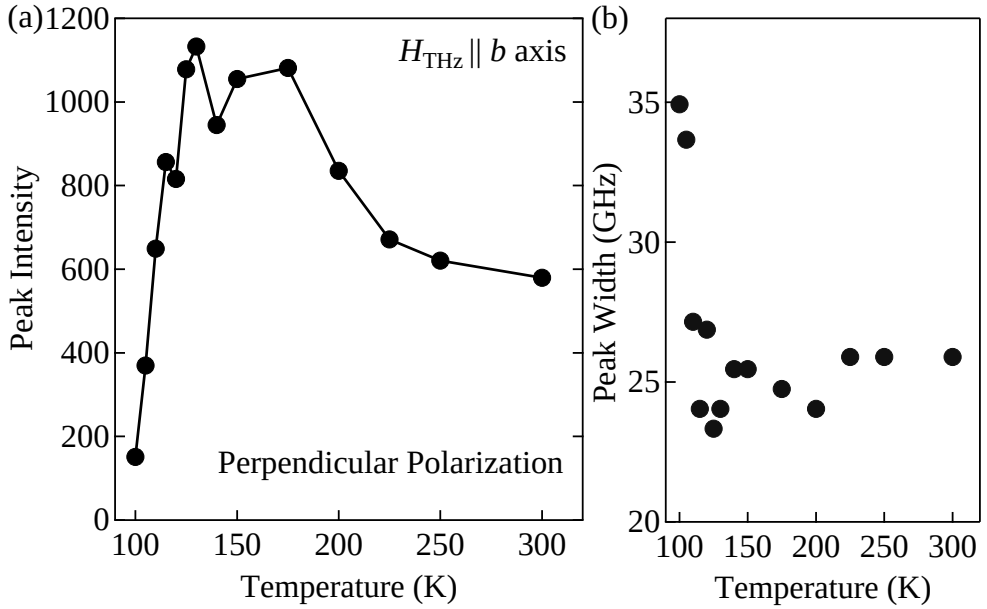

FIG. 5.7 (a) Temperature dependence of the FID intensity emitted from $ErFeO_3$ in the perpendicular polarization. (b)Temperature dependence in the full width half maximum of the FID peak in perpendicular polarization.

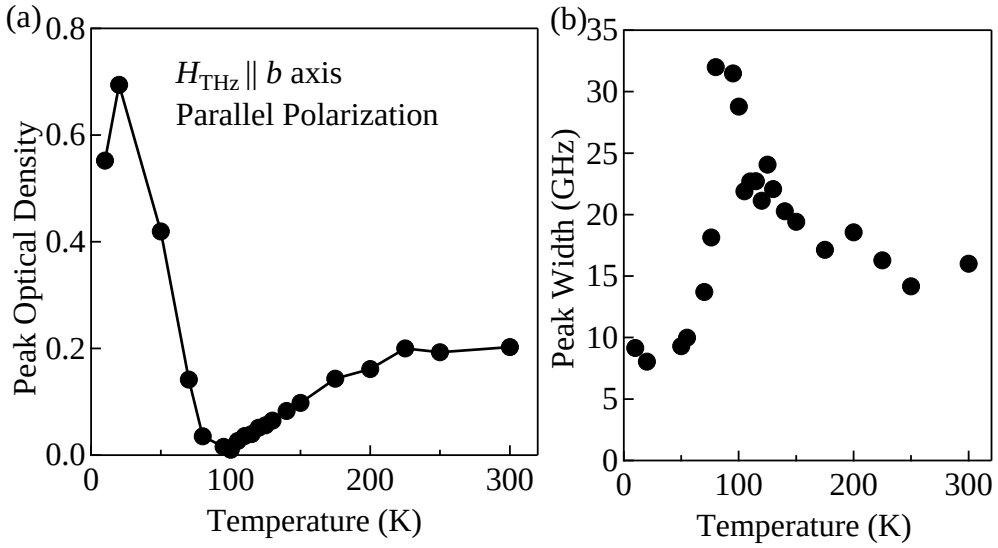

FIG. 5.8 (a) Temperature dependence of the FID intensity emitted from $ErFeO_3$ (peak value of the optical density) in the parallel polarization. (b) Temperature dependent full width half maximum of the peaks in the spectra obtained with FID emission in the parallel polarization.

ature. The temperature dependence of peak FID intensity in the perpendicular polarization is shown in Fig.5.7(a). From the figure, it can be observed that as the temperature approaches the spin reorientation temperature region, the FID intensity shows a rapid decrease. On the other hand, the peak width (full width half maximum) of the FID spectra increases in the vicinity of the spin reorientation region. Therefore, the FID intensity decrease can be ascribed partially to this spectral broadening. Similar behavior can also be observed in the parallel polarization (Fig.5.8). The plots in Figs.5.8(a) and (b) show that the intensity decrease and the peak broadening near the reorientation temperature also occurs in the low temperature phase.

Although the reason of this broadening effect in the vicinity of the spin reorientation cannot be determined, here, two possible mechanisms that can explain this broadening will be introduced.

The first possible mechanism is anharmonicity of the spin precession. It has been shown in the research reported in the past that the reorientation transition can be phenomenologically understood by representing the anisotropic energy of the Fe^{3+} spins by

$$K_2(T)\sin^2\theta + K_4\sin^4\theta \tag{5.1}$$

where $K_2(T)$ and K_4 are the second order and fourth order anisotropy coefficient, respectively, and θ is the angle between the macroscopic magnetization and the c axis [65]. Comparing this anisotropic energy with the Hamiltonian in equation (2.26), we can see that $K_2(T)$ can also be replaced with $2(A_x - A_z)$ and it is linearly dependent on the temperature. On the other hand, K_4 comes from fourth order anisotropy terms that were omitted in equation (2.26), and it is considered to be temperature independent. In the high temperature phase, $K_2(T)$ takes positive value and the equilibrium position of the weak ferromagnetic moment is $\theta = 0$. As the temperature approaches the reorientation region, $K_2(T)$ decreases and becomes negative in the low temperature phase. When the $K_2(T)$ takes a negative value, the equilibrium position starts to shift to $\theta = \pm\pi/2$, which is consistent with the spin configuration in the low temperature phase. This is illustrated in Fig.5.9. Confining the discussion into the case where $\theta = 0$ (high temperature phase), this potential energy can be expanded into

$$K_2(T)\theta^2 + K_4\theta^4 \tag{5.2}$$

In the temperature range sufficiently far from the spin reorientation region, $K_2(T)$ takes

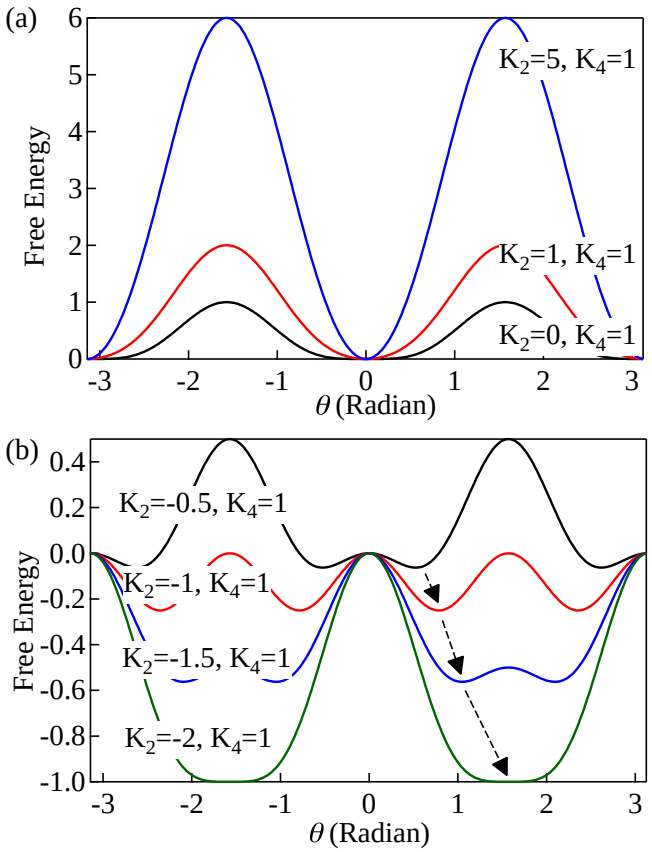

FIG. 5.9 (a)The temperature dependence of the free energy in the high temperature phase of $ErFeO_3$. (b) The free energy in the reorientation temperature region and the low temperature phase.

large value and the potential is harmonic. When the temperature approaches the reorientation region, the second order term becomes small compared to the fourth order term and the free energy becomes anharmonic. In addition, as Fig.5.9 shows, as the temperature approaches the reorientation transition temperature, the curvature of the free energy is loosened, which suggests that the confinement of the magnetic moment is weak in this region. Therefore, the distribution of θ due to thermal energy is predicted to be widely spread compared to that in the temperature region far from the transition temperature. Because the potential near the reorientation region is anharmonic, spins with different value of θ should have different resonant frequency. Thus, the widely spread θ gives rise to spins with various resonant frequency, which explains the observed broadening.

The second possible reason of the broadening is the inhomogeneity of the spin reorientation

temperature. Suppose that there is a certain amount of variations in the transition temperature due to inhomogeneity. In the region far from reorientation, the temperature dependence of the resonant frequency is small and the variation of resonant frequency due to variant transition temperatures is negligible. As the temperature approaches the reorientation region, the temperature dependence of the frequency becomes large. Therefore, slight variation of transition temperature may cause large difference in the resonant frequency. When such fluctuation of the resonant frequency exists, the observed FID peak in a spectrum would become broad. Figure5.10 shows the calculated width derived from the temperature dependence of the F mode resonant frequency (Fig.5.5) by assuming transition temperature fluctuation of about 3 K. With an temperature independent offset of approximately 15 GHz, the temperature dependence of the width can be well reproduced in the high temperature region. However, steep decline of the width in the low temperature region cannot be replicated with this broadening mechanism since the gradient of the resonant frequency in Fig.5.5 shows small temperature dependence. Therefore, although this broadening mechanism is able to reproduce the experimental result qualitatively, some disagreements with the results are still present.

Lastly, it should be noted that the temperature dependence of the FID intensity cannot be explained by the fluctuation of the peak width alone. The relative oscillator strength (the width times the peak intensity) shown in Fig.5.11 shows that considerable amount of temperature dependence still remains in both parallel and perpendicular polarizations. This result suggests that the coupling of the THz magnetic field and the F mode resonance seems to decrease in the vicinity of the spin reorientation region.

5.2.2 Excitation with THz Magnetic Field Component Along a axis

The transmitted THz waveforms in Fig.5.12 shows the temperature dependence of the FID emission obtained from excitation of (100) $ErFeO_3$ single crystal with $H_{THz} \parallel a$ axis THz pulse. In the high temperature phase, equivalent to the case of $H_{THz} \parallel b$ axis, emission from F mode resonance is observed. This is also consistent with the excitation condition of the F mode magnetic resonance in orthoferrites since $H_{THz} \parallel a$ axis is also perpendicular to the weak ferromagnetic moment which points toward c axis direction. However, as soon as the temperature of the sample is lowered below the transition temperature, unlike the previous

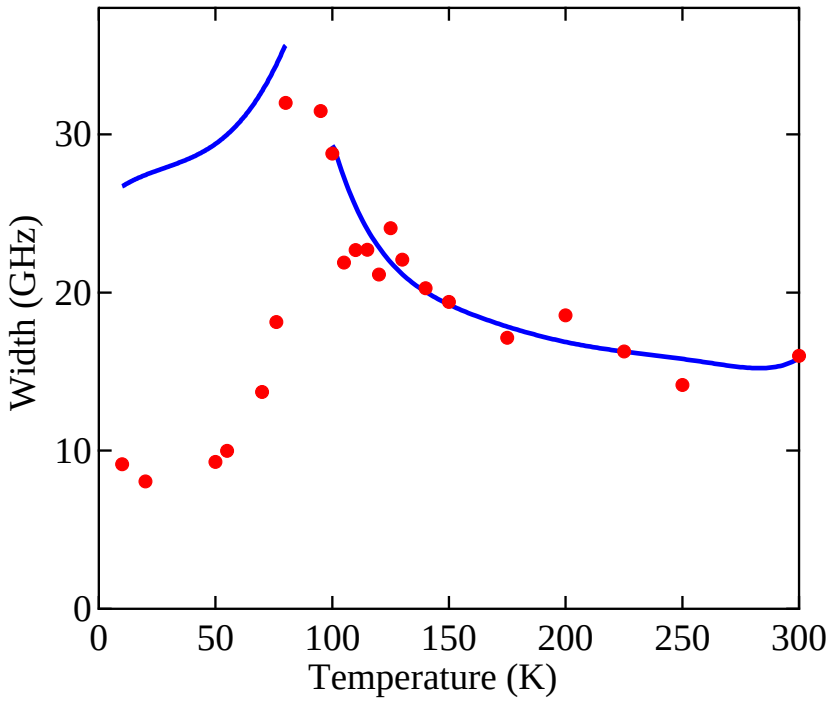

FIG. 5.10 The width of the $ErFeO_3$ F mode peak due to inhomogeneous spin reorientation temperature. The red closed circle markers show the actual FID width in the parallel polarization.

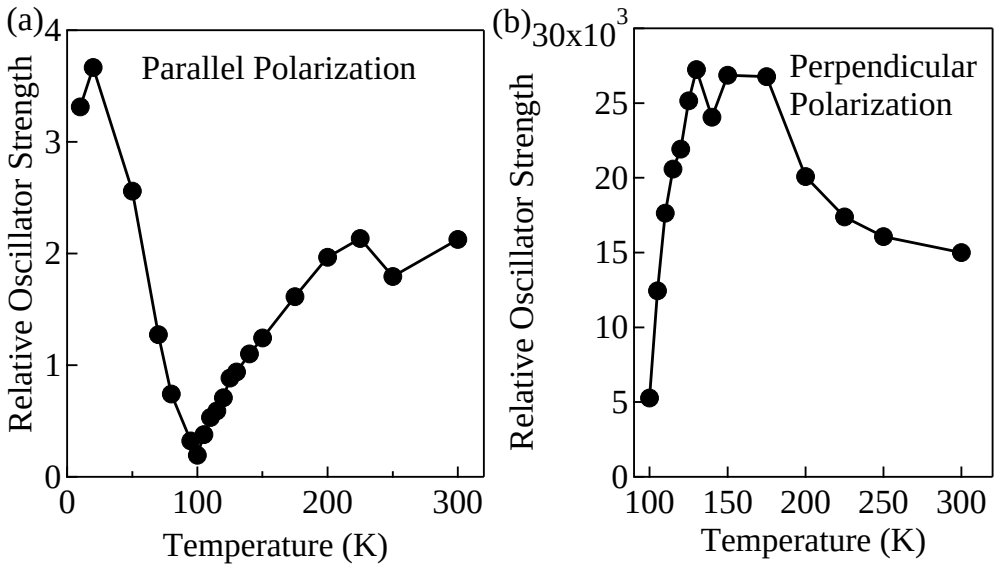

FIG. 5.11 Temperature dependence of the relative oscillator strength of $ErFeO_3$ F mode resonance in (a) parallel polarization, and (b) perpendicular polarization.

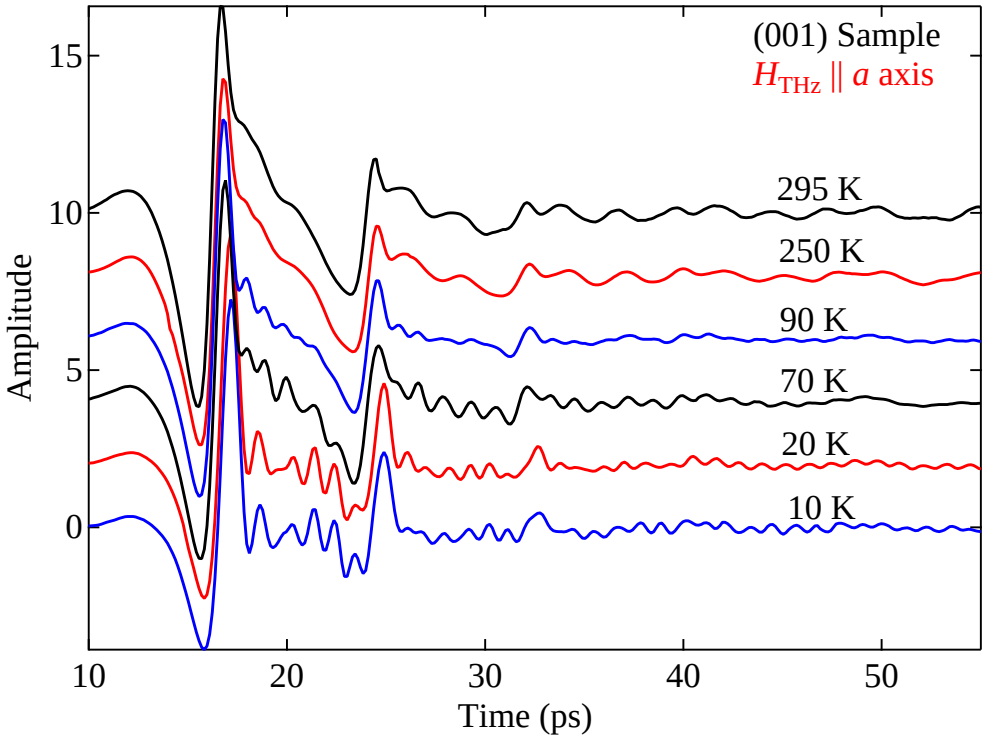

FIG. 5.12 Temperature dependence of THz temporal waveform transmitted from (100) $ErFeO_3$ sample. The polarization of the incident THz pulse is H_{THz} || a axis.

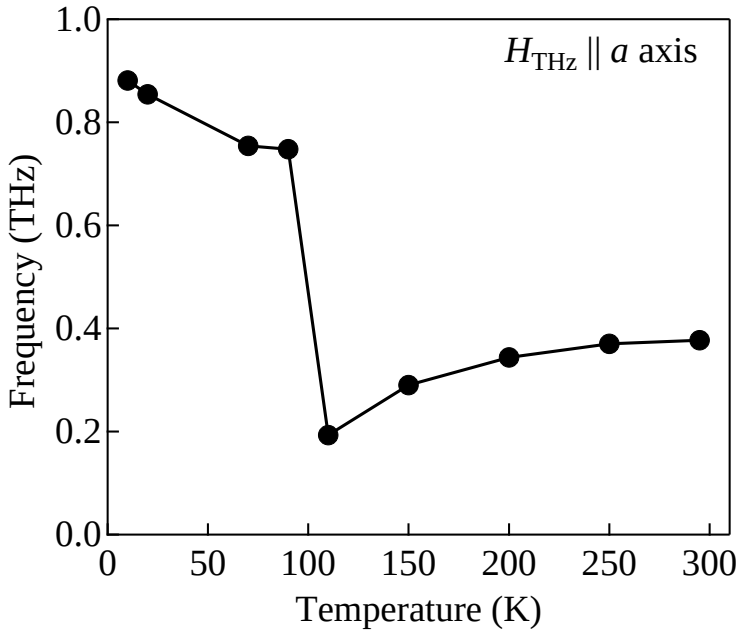

FIG. 5.13 Temperature dependence of FID emission peak frequency for (100) $ErFeO_3$ with H_{THz} || a axis THz pulse.

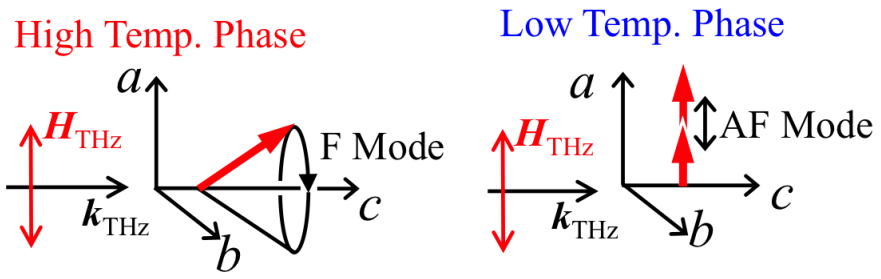

FIG. 5.14 Schematic describing the mode excited in $ErFeO_3$ by $H_{THz} \parallel a$ polarized THz pulse at high and low temperature phases.

$H_{THz} \parallel b$ axis case, an oscillation with a frequency which is much larger than the F mode resonance can be observed. The temperature dependence of the peak FID frequency plotted in Fig.5.13 shows that below the reorientation temperature, immediate increase of about 0.6 THz occurs. As described in Fig.5.14, in the low temperature phase of this configuration, H_{THz} polarized in the a axis direction becomes parallel to the macroscopic magnetization, which is the excitation condition of the AF mode resonance. The AF mode magnetic resonance frequency reported by Kozlov *et al.* [49] also matches with the result shown in Fig.5.13. Thus, this sudden jump of the FID frequency is attributed to the change of the excited magnetic resonance mode.

Similar to the result shown for $H_{THz} \parallel b$ configuration, this mode switching effect can be used to detect the spin reorientation transition. In this case, since the resonant frequency of the two modes differ greatly in the vicinity of the spin reorientation region (F mode: around 0.2 THz, and AF mode: around 0.75 THz), half cycle of the oscillation should be sufficient for distinguishing whether the mode being observed is either F mode or AF mode. Focusing on the existence of the AF mode whose oscillation period is about 1.33 ps at reorientation region, spin configuration for $ErFeO_3$ can be determined with 0.67 ps resolution.

5.2.3 Result Obtained from Sintered Pellet Sample

Temperature dependence of the THz pulse induced FID emission was also investigated with sintered pellet $ErFeO_3$ sample. The frequency of the F and AF mode emission are plotted for various temperatures along with the results obtained from the single crystal experiments

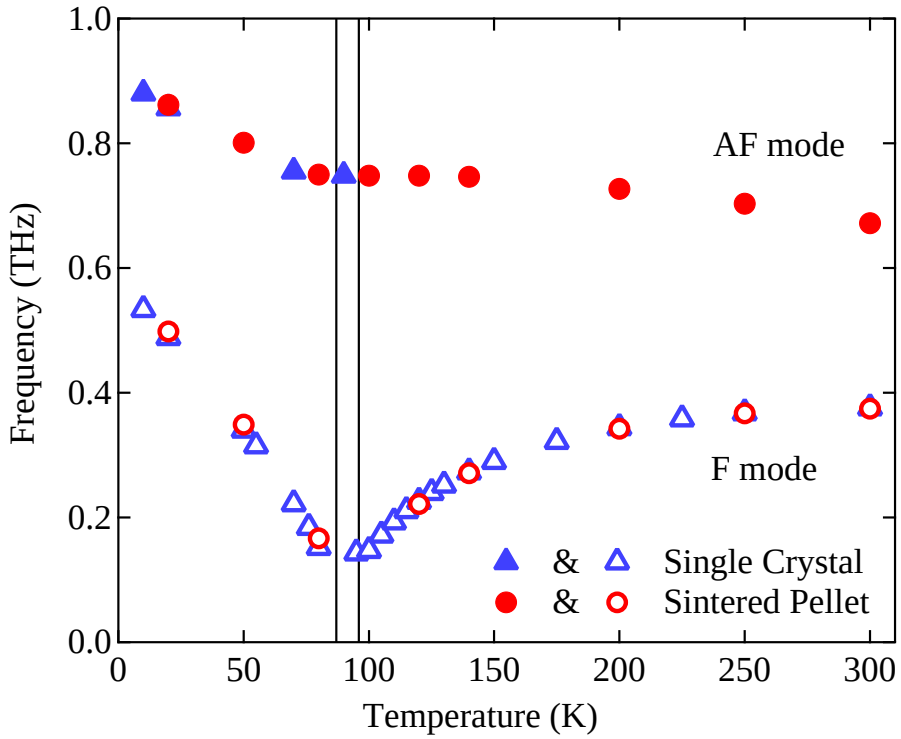

FIG. 5.15 Temperature dependence of F mode and AF mode resonant frequencies in $ErFeO_3$. Frequencies obtained from the single crystal sample and sintered pellet sample are plotted. Two vertical lines indicate the higher and lower transition temperatures at 96 K and 87 K.

(Fig.5.15). No notable difference is observed between the temperature dependence in the single crystal and the pellet sample.

Radiation in the perpendicular polarization was also observed with this sample. Unlike the single crystal samples, this pellet sample could not be magnetized with magnetic field as high as 0.5 T. By using a pulsed magnet with peak value of 8 T, pulse duration of 100 ms, the pellet was magnetized. The residual magnetic field of the sample was about 1mT.

Similar to the experiment with the single crystal, the phase transition into the low temperature phase resulted in the disappearance of the F mode FID emission in the perpendicular polarization (Fig.5.16(a)). This disappearance can be attributed to the loss of the residual magnetization during the phase transition which was also seen in the single crystal. However, when the pellet sample is returned to the high temperature phase, small portion of the FID emission is recovered. This behavior is distinct from that of the single crystal where such reoccurrence cannot be observed. Figure 5.16(b) shows the ellipticity and the rotation angle

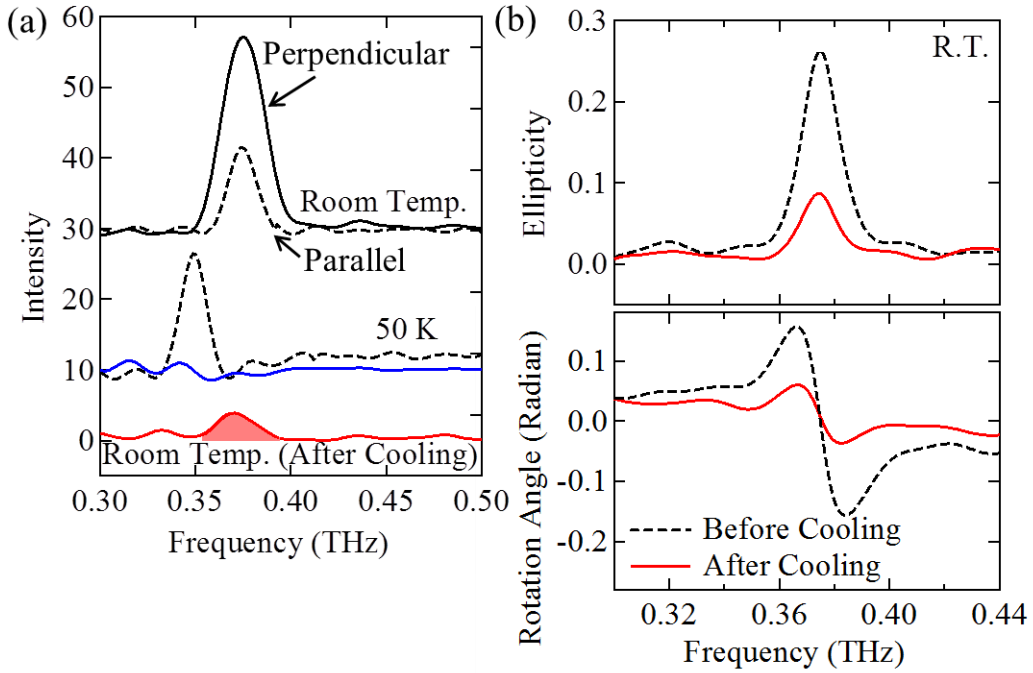

FIG. 5.16 (a) Spectra of FID emission in perpendicular polarization from THz pulse excited pellet $ErFeO_3$ sample which is magnetized perpendicular to the sample surface. The dashed spectra shows the oscillatory component in the parallel polarization due to the F mode resonance (the peak heights are arbitrarily modified). (b) Magneto-optocal spectra of the pellet sample at room temperature. The spectra obtained before cooling the sample below reorientation transition temperature and spectra obtained afterward are compared.

spectra of the transmitted THz wave at room temperature before and after the cooling. As the sign of the ellipticity points out, the helicity of the elliptic emission in the two cases are the same. Therefore the direction of the residual magnetization for the two cases are identical. For this reason, even though majority of the residual magnetization are lost during the spin reorientation transition, a memory effect of magnetic domains which records some portion of the domain structure seems to exist. Considering the large difference in the coercive field of the pellet sample and the single crystal, effects such as pinning of magnetic domains due to defects inside the microcrystals, and stress induced from lattice defects or grain boundaries may be the cause of this memory effect.

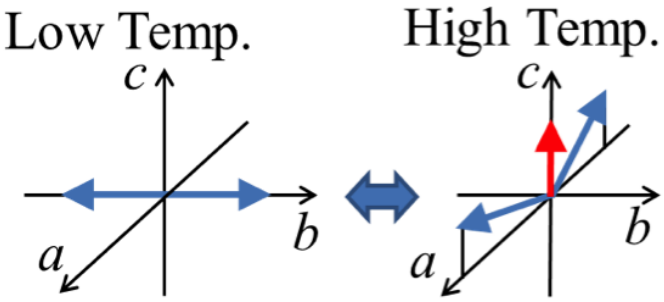

FIG. 5.17 Schematic illustrating the abrupt type spin reorientation in $DyFeO_3$. Simplified two sublattice spin configuration is adopted here.

5.3 Spin Reorientation in $DyFeO_3$

Orthoferrite $DyFeO_3$ shows spin reorientation transition which is distinct from the transition in $ErFeO_3$. The transition from high temperature Γ_4 phase to low temperature Γ_1 phase (Fig.5.17) can be interpreted in the following manner. When the temperature is lowered, the magnetic moment of Dy^{3+} spins increase. Unlike other types of rare-earth ions, single ion anisotropy of Dy^{3+} spins is significantly high and the magnitude of anisotropy energy matches with the exchange energy between the Fe^{3+} spins [47]. It has been reported that the Dy^{3+} spins in $DyFeO_3$ favor b axis as an easy axis [67]. Therefore, reduction of temperature results in increase of Dy^{3+} magnetization along the b axis and through exchange interaction, turns the Fe^{3+} spins parallel to the b axis.

5.3.1 Behavior of the Magnetic Resonance with Abrupt Type Spin Reorientation

THz-TDS measurement with single crystal $DyFeO_3$ was performed. As the samples, (100) sample with thickness of 1.6 mm, and (001) sample with 1.65 mm thickness were used. The result of the measurement at the room temperature is shown in Fig.5.18. Equivalent to $YFeO_3$ and the high temperature phase of $ErFeO_3$, the Fe^{3+} spin configuration of $DyFeO_3$ is Γ_4. The result shown in Fig.5.18 also supports this, because THz magnetic field perpendicular to the weak ferromagnetic moment ($H_{THz} \parallel a, b$) and THz magnetic field parallel to the magnetization ($H_{THz} \parallel c$) were confirmed to excite F mode and AF mode, respectively.

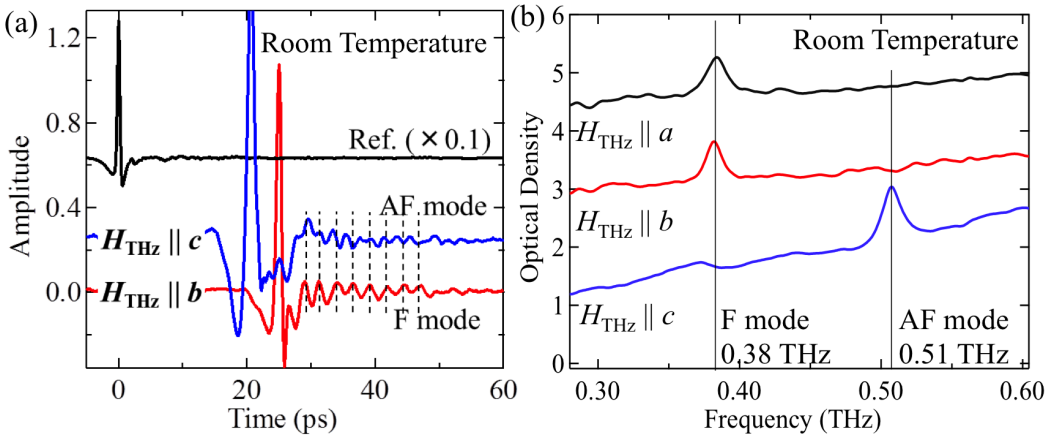

FIG. 5.18 (a) Transmitted THz wave through (100) $DyFeO_3$ single crystal sample at room temperature. (b) Spectra obtained from the waveforms in (a). The spectrum for $H_{THz} \parallel a$ was obtained from TDS measurement with (001) sample.

Figures5.19(a) and (b) shows the result of temperature dependent THz-TDS measurement for $H_{THz} \parallel a$, $H_{THz} \parallel b$, and $H_{THz} \parallel c$ configurations. At low temperature (5 K), $H_{THz} \parallel a$ and $H_{THz} \parallel c$ excitation results in FID emission with 0.547 THz and 0.291 THz, respectively. On the other hand, in $H_{THz} \parallel b$ configuration, no such peak can be seen in 5 K. The temperature dependence of the FID emission peak value in Fig.5.19(b) shows that finite amount of FID emission exists in both $H_{THz} \parallel a$ and $H_{THz} \parallel c$ configuration whereas in $H_{THz} \parallel b$, the FID peak vanishes abruptly at around 60 K.

The temperature dependence of the FID frequency is plotted in Fig.5.20. Unlike $ErFeO_3$, the resonant frequency changes continuously and no switching of the excited resonance mode are observed in any polarization. The figure shows that $H_{THz} \parallel a$ excites F mode in the whole temperature range and $H_{THz} \parallel c$ similarly excites AF mode. Another significant aspect of this temperature dependence distinct with that of the $ErFeO_3$ in the previous section is that instead of the F mode, the AF mode shows softening in the vicinity of the spin reorientation region. On the other hand, temperature dependence of the F mode frequency is very small. Such difference in the behavior of the resonant frequencies occur because the anisotropic energy induced by the rare-earth magnetic moment is different for these two cases. Unlike $ErFeO_3$ where the Er^{3+} spins generated effective magnetic field which favors the orientation of Fe^{3+} spins along c axis, Dy^{3+} spins generates effective magnetic field which turns the Fe^{3+}

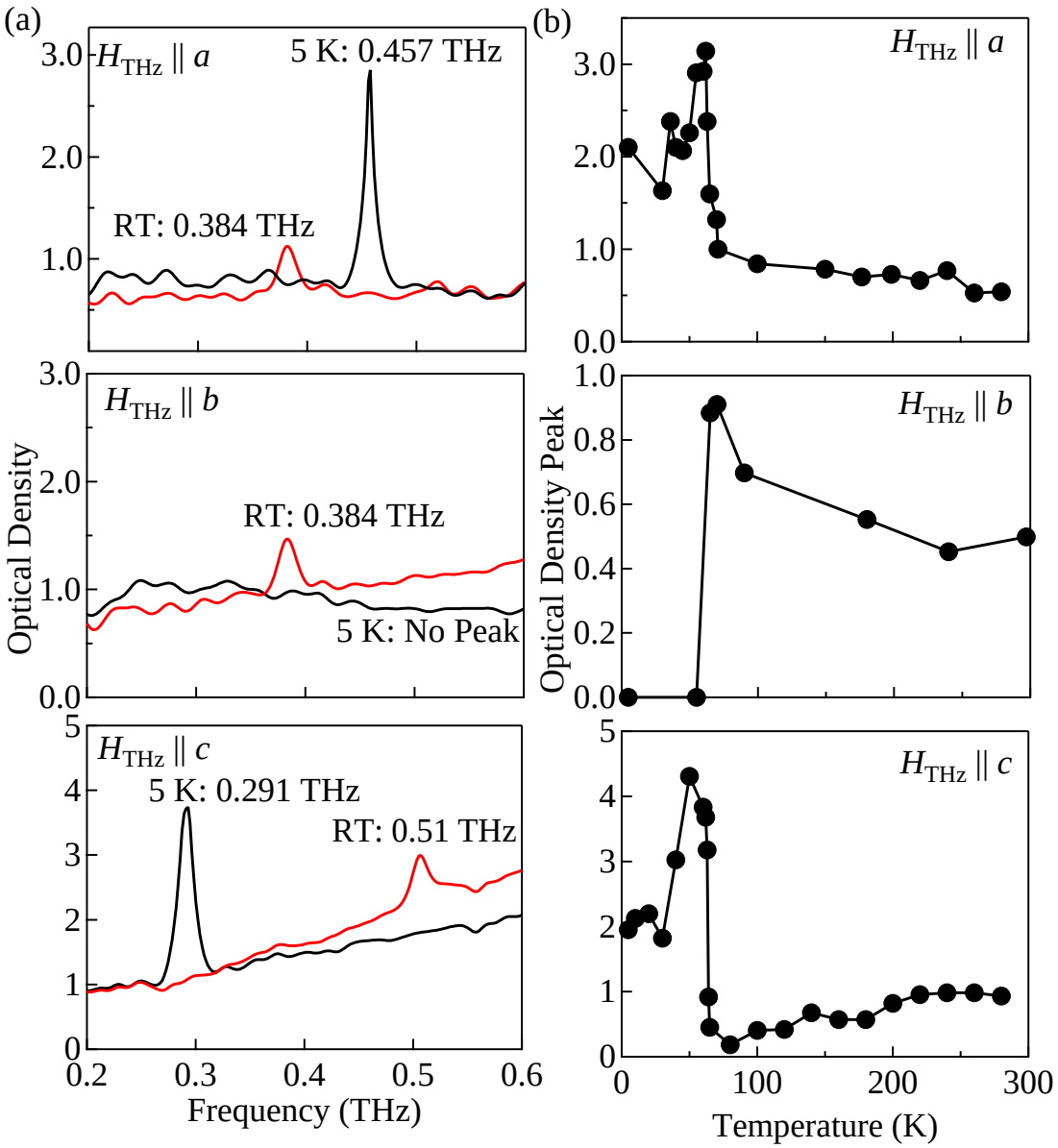

FIG. 5.19 (a) Transmitted THz optical density spectra through $DyFeO_3$ single crystals at room temperature and 5 K. (b) Temperature dependence of the FID peak value in the optical density spectra.

spins to the b axis. This means that A_y in the equation 2.30 increases and this explains the temperature dependence of the resonant frequencies. The temperature dependence of the resonant frequency obtained by backward wave oscillator reported by other group also shows similar behavior [49].

The reorientation transition temperature determined from the temperature dependence of the AF mode frequency is $T_r = 65$ K. This value differs largely from the transition temper-

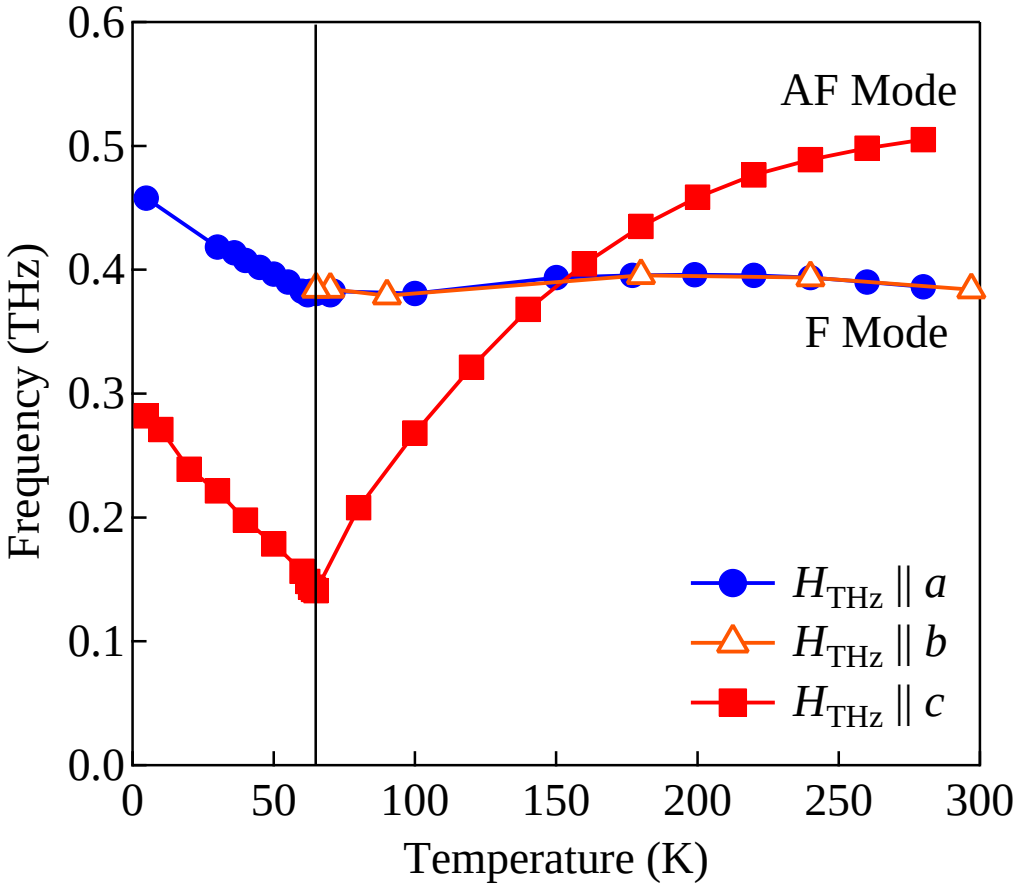

FIG. 5.20 Temperature dependence of the FID peak frequency for $H_{THz} \parallel a$, $H_{THz} \parallel b$, and $H_{THz} \parallel c$ configurations in $DyFeO_3$.

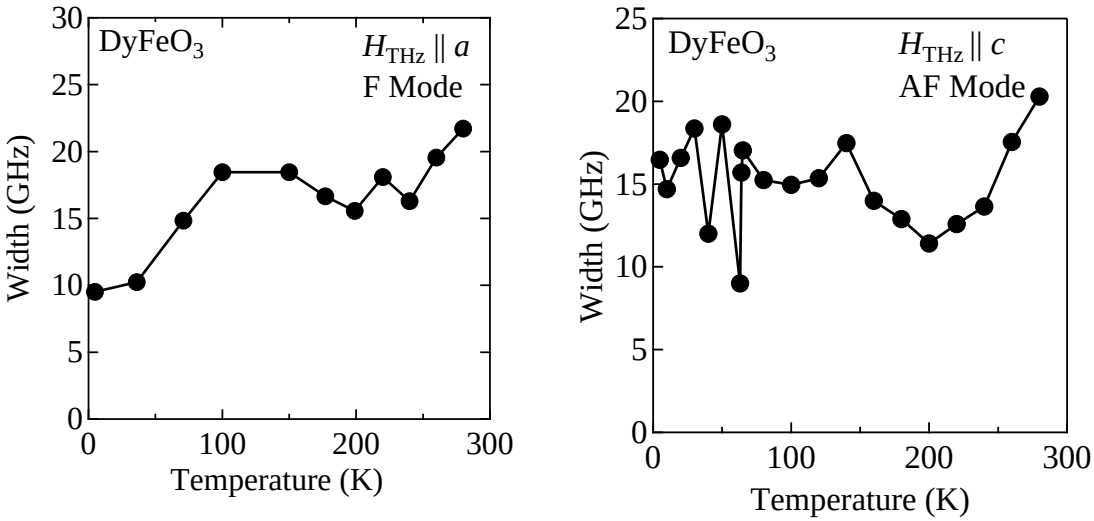

FIG. 5.21 Temperature dependence of the spectral width of F and AF mode peaks in $DyFeO_3$.

ature T_r=48 K reported by other groups [49]. Since impurity which degrades the magnetic effect of the Dy^{3+}, or substitution of Dy^{3+} ions with other types of nonmagnetic or magnetic rare-earth is expected to decrease the transition temperature [68], it is unlikely that the lack of quality of the sample used in this research is the cause of this discrepancy.

Lastly, the temperature dependence of the spectral width of F and AF modes are shown in Fig.5.21. Unlike the width of the F mode resonance in $ErFeO_3$, no broadening was seen in the temperature region near the reorientation transition temperature.

5.3.2 Large Shift of Resonant Frequency Induced by Low Amplitude Magnetic Field

According to reference [69], spin reorientation from Γ_1 (low temperature) phase to Γ_4 (high temperature) phase can be achieved by applying magnetic field along the *c* axis. Because the reorientation in $DyFeO_3$ occurs abruptly at the transition temperature, 0.1 T order magnetic field is sufficient for realizing magnetic field induced phase transition. This threshold magnetic field in $DyFeO_3$ is strikingly small when compared with the external magnetic field of several tesla which is required in $ErFeO_3$ to realize transition from Γ_4 (high temperature) to Γ_2 (low temperature) phase, and vice versa [70].

A phase diagram in Fig.5.22 shows the threshold magnetic field along the *c* axis at various temperature [69]. This phase diagram can also be interpreted as the change of transition temperature induced by the external magnetic field. When viewed this way, it can be predicted that magnetic field of 0.1 T causes the reorientation temperature to shift approximately 10 K. Deducing from this, since the AF mode resonant frequency is highly dependent on the temperature, application of external magnetic field is expected to cause significantly large shift of the resonant frequency. Here, to study the details of the expected frequency shift of AF mode resonance, THz-TDS with sub-Tesla order external magnetic field was conducted with the $DyFeO_3$ single crystal.

First, the experiment was carried out with external magnetic field in the Faraday configuration where the magnetic field is parallel to the THz wave vector. Since AF mode is excited by THz magnetic field parallel to *c* axis, in order to apply external magnetic field along *c* axis and excite AF mode at the same time, 1.4 mm thick (101) plane single crystal sample was

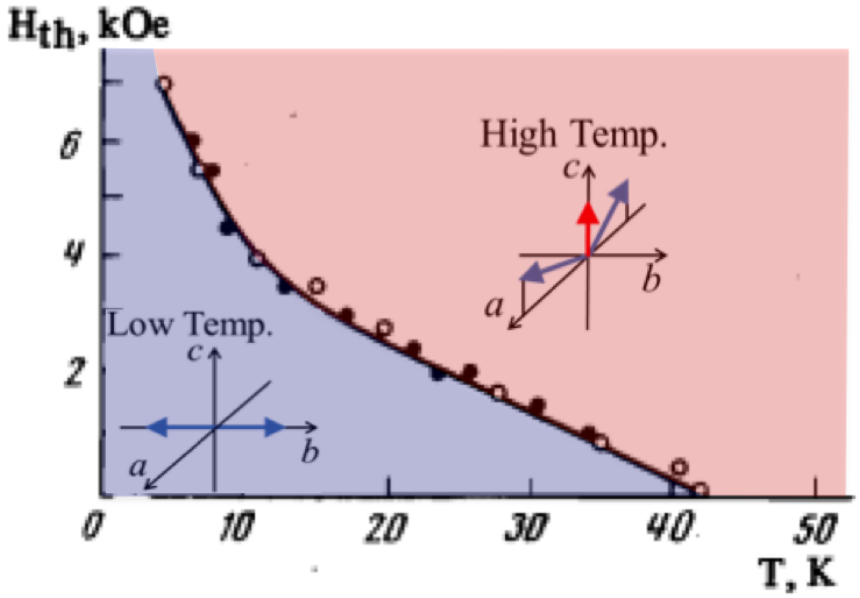

FIG. 5.22 Phase diagram of $DyFeO_3$ [70]. The threshold magnetic field at various temperature is shown. The direction of the external magnetic field is along the crystallographic c axis

prepared. The orientation of the crystal with respect to the THz wave vector, THz magnetic field, and external magnetic field is illustrated in Fig.5.23(a). The external magnetic field was applied with a pair of neodymium-iron-boron magnet. The magnetic field amplitude at the sample position was approximately 0.38 T. Because angle between the c axis and the external magnetic field is 55.2° (calculated from lattice constants a=5.302 Å, and c=7.623 Å [38]), the actual external magnetic field along the c axis is $\cos 55.2° \times 0.38$ T=0.217 T. As a next step, the measurement with external magnetic field in Voigt configuration (Fig.5.23(b)) was conducted. This time, (100) sample was used for the measurement.

The results of these experiments are organized in Fig.5.24. As the temperature dependence of AF mode with external magnetic field show, no significant change can be observed in the region far from the reorientation temperature (Fig. 5.24(a)). On the other hand, when the temperature of the sample approaches the reorientation region, magnetic field dependence is clearly observed (Fig.5.24(a)). From this figure, it can be observed that the application of 0.217 T and 0.28 T along the c axis results in shift of reorientation temperature. The amount of shift for these two cases are approximately 10 K and 13 K, respectively. Converting these into shift per 0.1 T, approximately 4.6 K can be yielded for both cases. This agreement of

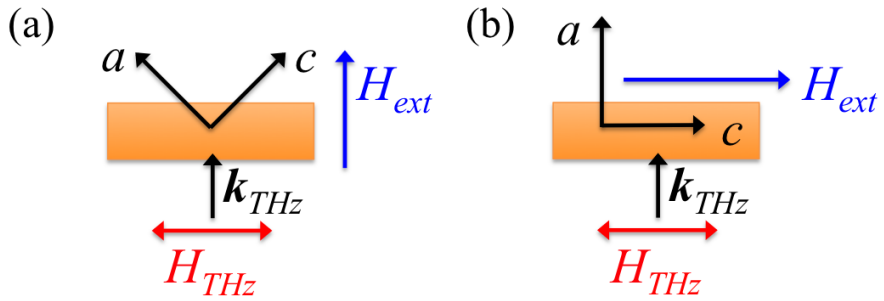

FIG. 5.23 Schematics illustrating the orientation of crystal in experiment with (a) Faraday configuration, and (b) Voigt configuration.

the temperature shift suggests that the effect of magnetic field applied along *a* axis in Faraday configuration is negligible, which was actually expected since the threshold magnetic field along the *a* axis is an order of magnitude larger than the threshold field along the *c* axis [70] We also can ignore the difference of the demagnetizing coefficient between Faraday and Voigt configurations, and this is consistent with the fact that the macroscopic magnetization of the orthoferrite is small.

Next, we will focus on the frequency shift induced by the external magnetic field. Figure5.25 shows the AF mode FID spectra at 50 K for three cases: no magnetic field, 0.217 T magnetic field, and 0.28 T magnetic field. In this temperature region, as the applied magnetic field increase, the FID peak softens. As it can be seen in Fig.5.24(b), the amount of frequency shift is dependent of the temperature. Figure5.26 plots the obtained frequency shift at 20 K, 30 K, and 50 K. This plot shows that as the temperature moves further away from the reorientation temperature, the amount of shift decreases. When comparing the frequency obtained with no magnetic field and the frequency obtained with 0.28 T, the frequency shift is maximized at about 50 K and 65 K (Fig.5.24(b)). Because the total amount of frequency shift at 50 K is approximately 30 GHz, in this experimental condition, the maximum frequency shift per 0.1 T is 10.7 GHz. In the room temperature, application of the external magnetic field resulted in a small frequency shift of about 1.45 GHz/0.1 T.

The most straight forward effect of the external magnetic field expected to be seen in the magnetic resonance is that it induces frequency shift of $\Delta\omega = \gamma H_{ext}$. Using the gyromagnetic constant of the isolated electron $\gamma = 1.76\times10^{11}$ rad T^{-1} s^{-1}, the expected shift due to external

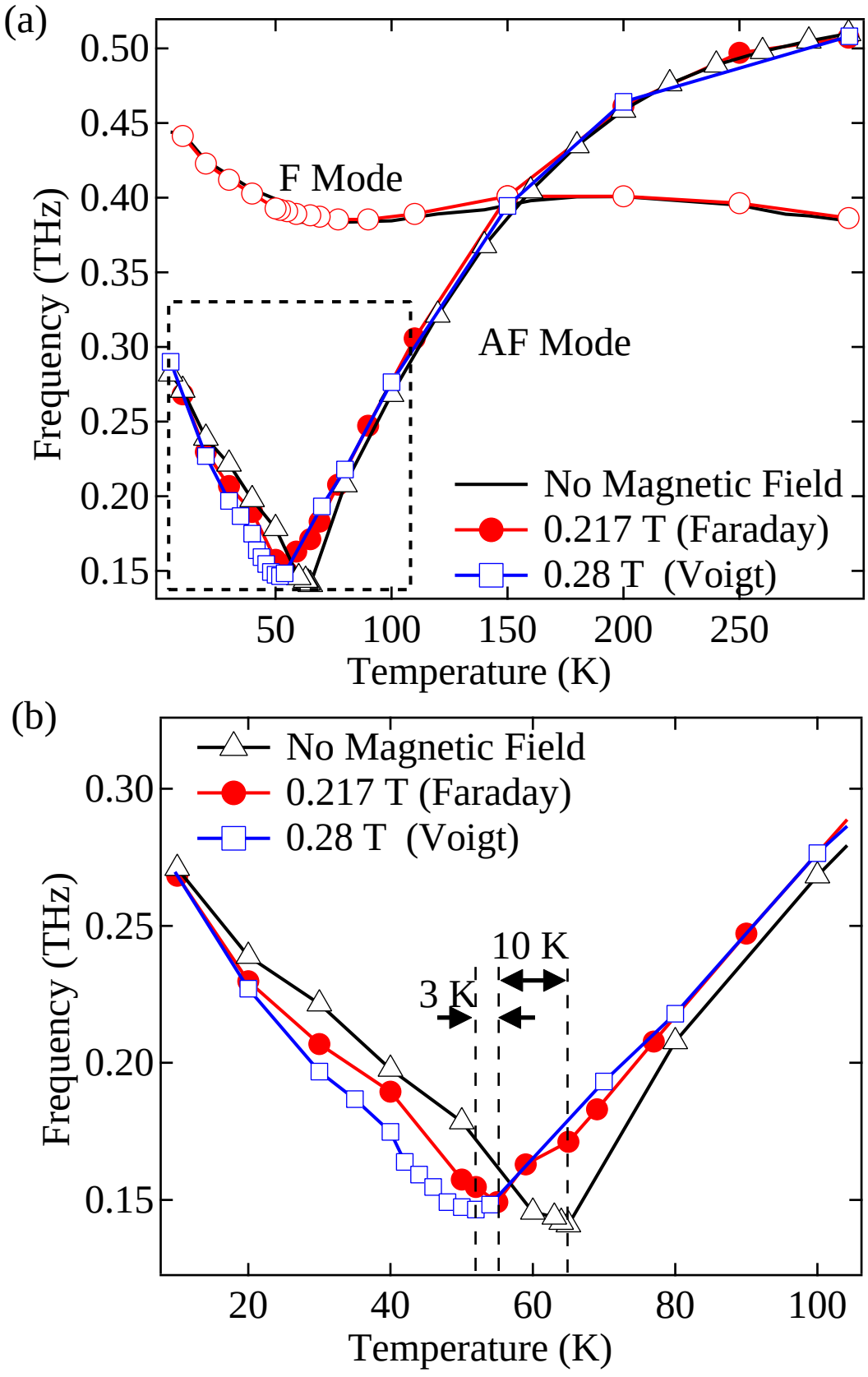

FIG. 5.24 (a) Temperature dependence of FID frequency in $DyFeO_3$ with no external magnetic field, 0.217 T, and 0.28 T external magnetic field along the *c* axis. (b) Magnified plot of the part surrounded by the broken lines in (a).

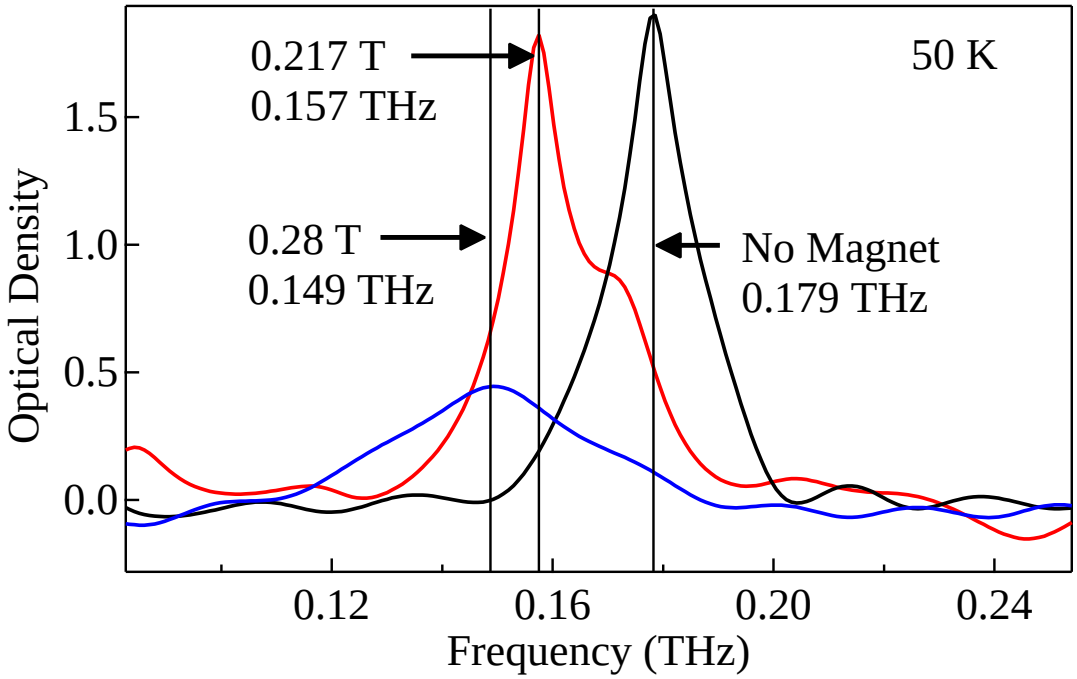

FIG. 5.25 Optical density spectra of $DyFeO_3$ at 50 K measured with no magnetic field, 0.217 T, and 0.28 T external magnetic field along the *c* axis. The peak shift of AF mode FID due to application of the magnetic field can be observed.

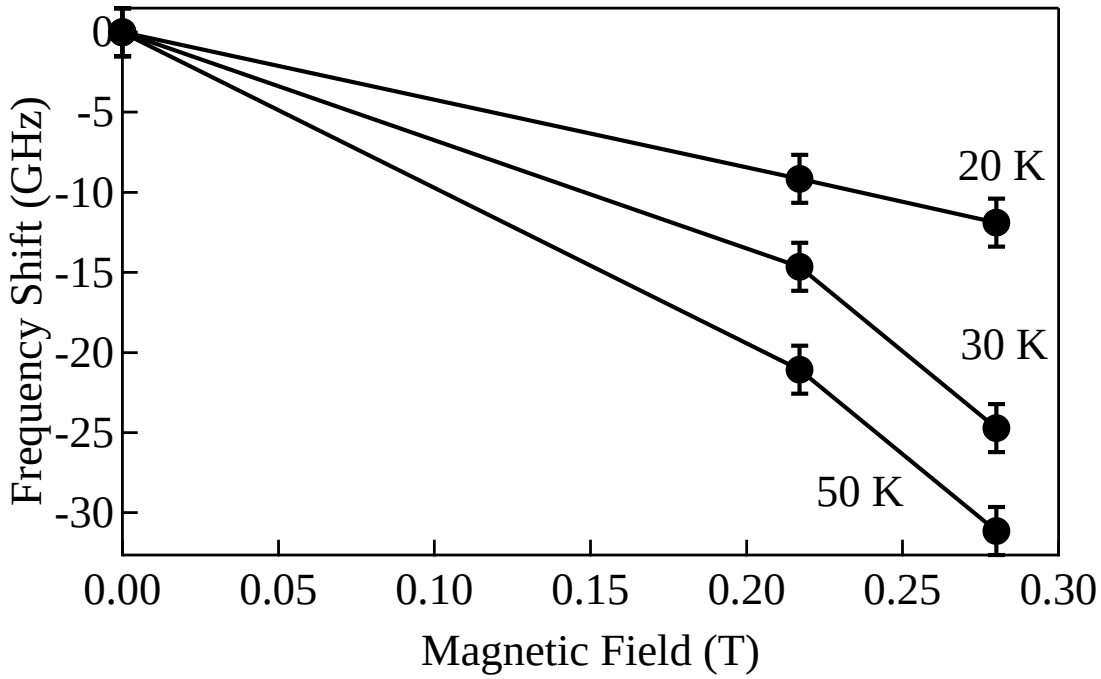

FIG. 5.26 The frequency shift of AF mode resonance in $DyFeO_3$ induced by external magnetic field at 20 K, 30 K, and 50 K.

magnetic field of 0.1 T is 2.78 GHz. This is close to the frequency shift obtained at room temperature and therefore the peak shift at room temperature can be ascribed to this effect. On the other hand, the amount of shift at 50 K is much larger than the shift expected from the calculation and cannot be explained by this effect only.

One of the biggest difference between room temperature and 50 K is the magnitude of the paramagnetic Dy^{3+} moment. Near the reorientation region, the magnetic moment of Dy^{3+} becomes large enough to alter the magnetic anisotropy of Fe^{3+} spins. As it was seen previously, this change of the anisotropy energy changes the resonant frequency of the AF mode. Because the external field induced reorientation is interpreted to occur due to the interaction of the external magnetic field and Dy^{3+} spins [69], this large shift of the AF mode resonance can also be ascribed to the perturbation applied to the Dy^{3+} spins which then affects the anisotropy of Fe^{3+} spins. Therefore, in a sense, this large shift of AF mode resonance frequency can be viewed as amplification of external magnetic field via Dy^{3+} spins.

5.4 Visible Laser Pump - THz Pulse Probe Experiment in $ErFeO_3$ and $DyFeO_3$

To demonstrate that the magnetic resonance excited by THz pulse can be employed to observe ultrafast heating and ultrafast spin reorientation induced with optical pumping pulse, visible laser pump-THz pulse probe experiment was performed.

In the visible and near infrared optical region, orthoferrites are known to have absorption peak due to the transitions ${}^6A_1 \rightarrow {}^4T_1$ and ${}^6A_1 \rightarrow {}^4T_2$ of Fe^{3+} in an octahedral crystal field [71]. Soon after the absorption of optical pulse, the excited Fe^{3+} electrons equilibrate with the lattice. Subsequently, the heated lattice interacts with the electrons of the rare-earth ion and the electronic temperature of the rare-earth are heated. This thermal excitation of the rare-earth electrons manifest in the magnetic resonance of the orthoferrites [20].

The experiments shown in this section aimed to observe ultrafast heating of the spin system through frequency shift of the magnetic resonance modes in orthoferrites $ErFeO_3$ and $DyFeO_3$.

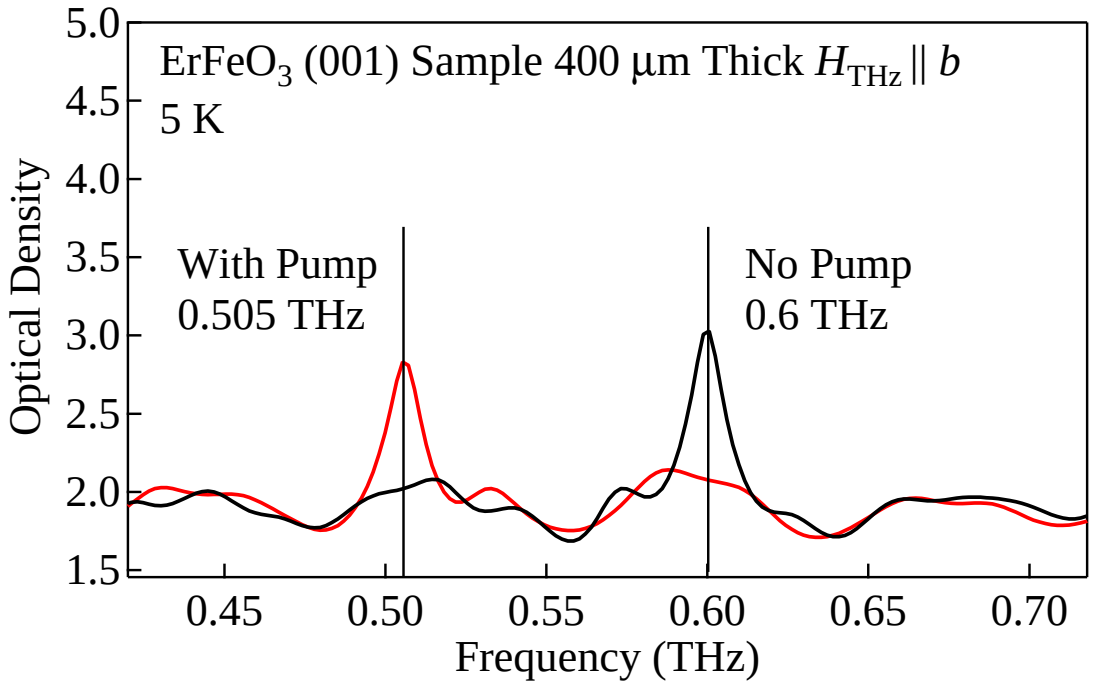

FIG. 5.27 The frequency shift of F mode resonance in $ErFeO_3$ observed with THz-TDS which results from pumping pulse.

5.4.1 Pump and Probe Experiment with THz TDS Method

At first, attempts on observing the optical pumping effect were made with the transmission type THz-TDS method. The pumping pulse was collimated to a diameter of 1 mm, which covers the THz spot area generated from ZnTe crystal. Figure5.27 shows the effect of pumping $ErFeO_3$ (001) sample with 400 μm thickness with150 μJ Ti:sapphire pulse (800 nm, 19 mJ/cm^2). The polarization of the incident THz pulse was $H_{THz} \parallel b$ axis and the temperature of the sample was 5 K. As the figure shows, the F mode frequency shifted for about 0.1 THz. Here, the timing of the pumping was set so that both the THz pulse and pumping laser enters the sample at the same moment of time. In this temperature range, 0.1 THz shift is equivalent to temperature increase of roughly 22.4 K (Fig.5.15). This result is striking since the pump fluence is roughly the same amount as that used in nonthermal precession excitation using the inverse Faraday effect [13].

However, changing the timing the pump pulse arrives at the sample resulted in no significant change in the obtained temporal waveforms and spectra. This suggests that the observed

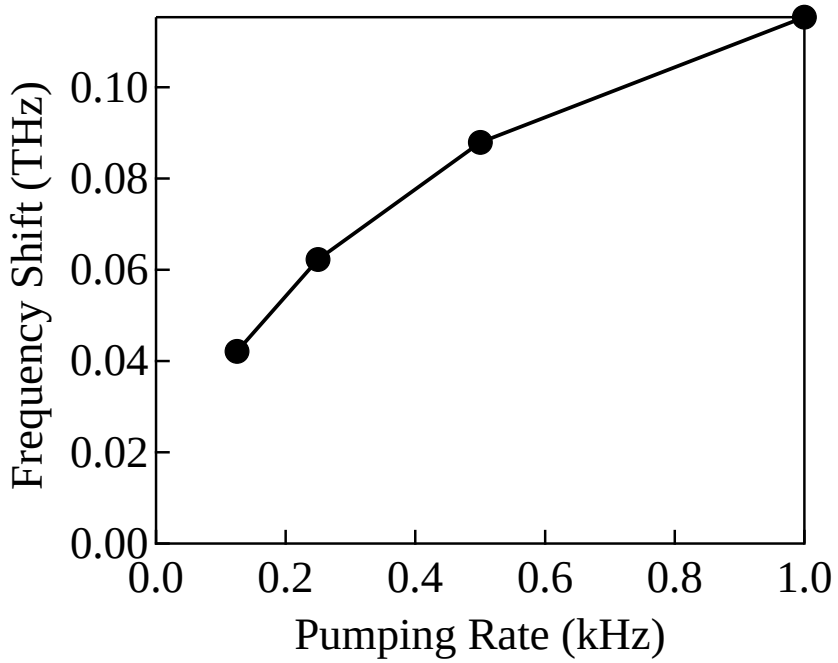

FIG. 5.28 The frequency shift of F mode resonance in $ErFeO_3$ obtained with various repetition rate of the pumping pulse.

temperature increase is not an ultrafast heating observed in preceding researches [26, 30]. To clarify the origin of this temperature increase, the same experiment was conducted with various repetition rates of the pumping pulse (Fig.5.28). The measurement revealed that the amount of frequency shift (and temperature increase) depends on the pumping rate. As the pumping rate decreases, the frequency shift also decreases. From this result, it can be seen that the temperature increase induced by the pumping pulse persists for over several milliseconds and gradually accumulates over time. The ultrafast heating due to each pulses therefore seems to be obscured by this gradual heating effect.

Then, the question why such large amount of heating was not reported in the past where the same amount of pump fluence or larger was used [13, 30] remains. The fact that the result presented by Kimel *et al.*, where pumping pulse of 100 mJ/cm^2(approximately 5 times larger than in this experiment) was employed for generating ultrafast heating of the spin system [30], was not obscured by this gradual heating implies that such effect does not exist in their case. The most prominent difference between this experiment and the past researches are the spot diameter of the pumping pulse. In the reported works, the diameter of the pump pulse ranges

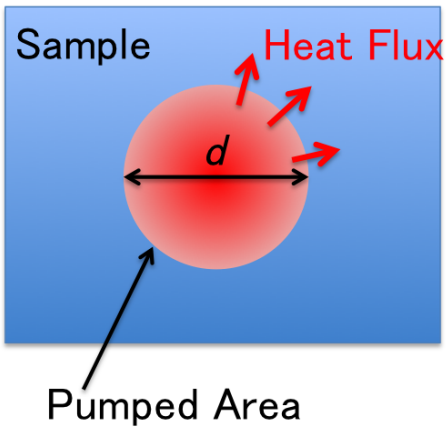

FIG. 5.29 Schematic illustration of heat dissipation occurring as a result of optical pulse pumping of the spins.

from 50 μm to 200 μm which is much smaller than our pump spot diameter of 1 mm. When considering the dissipation of heat from the pumped area with a diameter of d, the total area of boundary where heat flux can pass through is proportional to the diameter d, whereas the total volume of the pumped part of the sample is proportional to d^2 (Fig.5.29). Therefore, as the diameter d gets larger, the thermal dissipation from the pumped area becomes increasingly slow.

In order to conduct visible pump-THz probe experiment with THz-TDS technique, it is necessary to excite the sample uniformly over the THz spot size area. In the case of this experiment this necessity hinders the observation of ultrafast heating effect in orthoferrites. However, at the same time, substantial thermal effect was found to exist in optically pumped ultrafast spin excitation experiment, and depending on the condition of the experiment, this thermal effect may obscure the ultrafast spin dynamics. Therefore, at least to some extent, application of optical pulse for triggering the spin excitation should be handled with care.

5.4.2 Visible Pulse Pump-THz Pump-Visible Faraday Probe Experiment with $LiNbO_3$ Generated THz Pulse

To overcome the slow heating of the sample, pump pulse was focused to a spot diameter of approximately 100 μm. Because the spot size of the THz pulse is roughly 300 μm, the effect of the pumping pulse cannot be detected efficiently with THz-TDS. Therefore, additional visible probe pulse with a spot diameter of approximately 30 μm was introduced and the

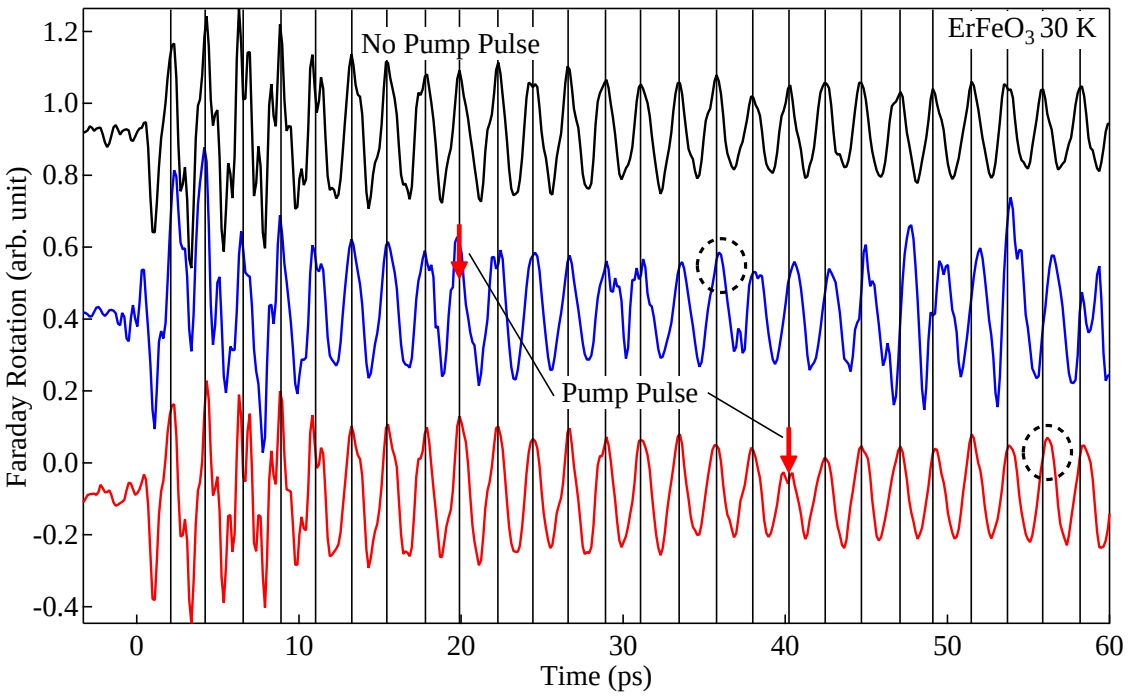

FIG. 5.30 Time dependent Faraday rotation signals induced by THz pulse excited spin precession in $ErFeO_3$. The red arrows show the time of the moment when the 800 nm pumping pulse arrived at the sample.

spin precession excited with the THz pulse was detected through Faraday rotation of the probe pulse. Since the spot size of the probe pulse is much smaller than the pumping visible pulse, the area observed with the probe pulse can be regarded as being uniformly excited by the pump pulse. In order to excite precession motion that is large enough so that the spin dynamics can be observed with the Faraday rotation, high power THz pulse generated from $LiNbO_3$ was used.

First, the pump probe experiment was conducted on (001) $ErFeO_3$ sample with thickness of 100 μm. THz pulse with its magnetic field component parallel to the *b* axis was used to excite the F mode. Since the F mode in the low temperature phase is a precession of the macroscopic magnetization inside *bc* plane, this precession can be observed with the Faraday rotation of the probe pulse.

The time dependent Faraday rotation signals at 30 K are shown in Fig.5.30. At 0 ps, THz pulse arrives at the sample and excites the F mode resonance. The figure shows the results obtained with no pump pulse, pump pulse at 20 ps, and pump pulse at 40 ps. The pump

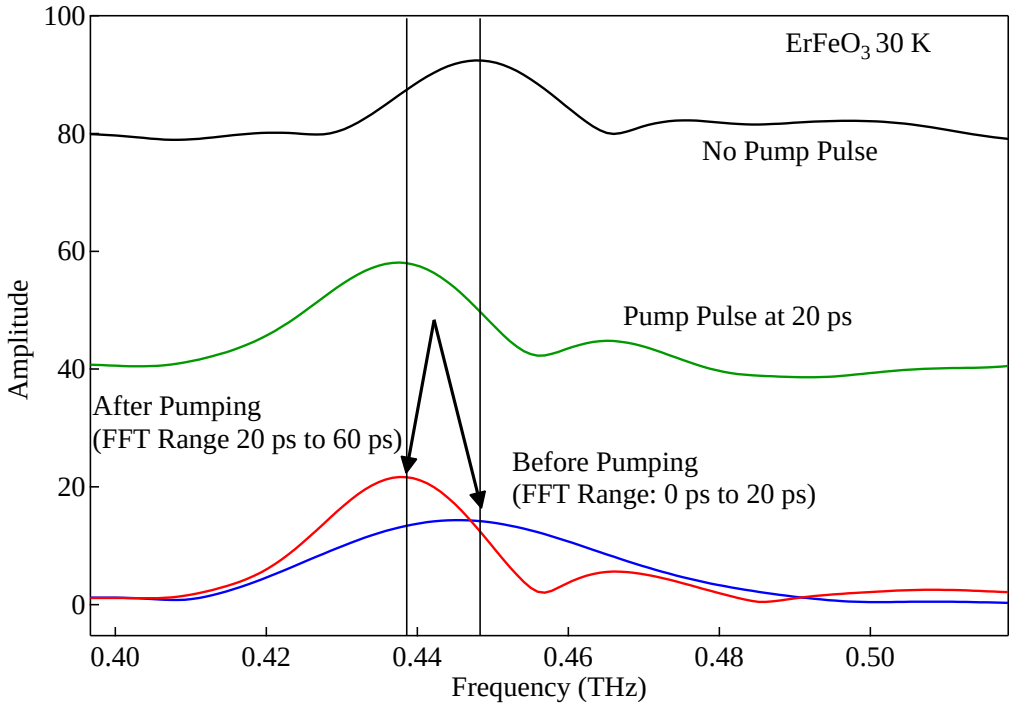

FIG. 5.31 The spectra obtained from the temporal Faraday rotation signals shown in Fig.5.30.

pulse fluence is approximately 100 mJ/cm^2. Focusing on the phase of the oscillations, it can be seen that no difference exists prior to pumping. After the pumping pulse is introduced, the phase of the oscillation starts to deviate from the oscillation obtained with no pumping pulse. This phase shift can be attributed to the shift of the resonant frequency which occurred as a result of ultrafast heating induced by the pumping visible pulse. For both pumping at 20 ps and 40 ps, this phase shift becomes prominent at roughly 15 ps after the pumping. Unlike in the previous experiment, the result shown here clearly exhibits difference between the measurements with different arrival time of the pumping pulse. Figure5.31 shows the Fourier spectra of the Faraday rotation signals shown in Fig.5.30. When we compare the spectrum obtained with no pumping pulse and the spectrum with pumping at 20 ps, it can be seen that the frequency of the F mode shifts about 10 GHz, which is equivalent to temperature increase of about 2.24 K in this temperature region. By dividing the temporal range used for Fourier transformation into two parts, namely, the region before the pump pulse arrives at the sample and the region after the pumping occurred, the obtained frequency of the F mode resonance clearly shows difference. In the temporal region prior to the pumping, the resonant frequency is equal to the frequency obtained by the measurement with no pumping pulse.

In the post-pumping temporal region, the frequency which shifted from the initial frequency becomes dominant. Thus it was verified that time dependent frequency shift induced by ultrafast heating of the spin system can be observed with this method.

For more detailed analysis of the data, time-frequency analysis on the obtained data was done. Figure 5.32 shows the time-frequency distribution of the temporal waveforms in Fig.5.30 with Choi-Williams transformation which provides improved resolution of frequency vs time compared to other time-frequency analysis method such as Wavelet transformation and short time Fourier transform [72, 73].

The time versus frequency plot with no pump pulse and pumping at 20 ps shows apparent difference. While in the plot obtained with no pump pulse show that the resonant frequency is independent of time, introduction of a pump pulse changes the frequency. From this data, the frequency at each moment of time was plotted for pumping pulse with 100 mJ/cm^2 and 50 mJ/cm^2 (Fig.5.33 (a)). As this figure shows, the thermal excitation induced by the pumping pulse gradually heats up the sample and the frequency shift settles at about 20 ps after the excitation. In Fig.5.33(b), the frequency shift is converted into temperature shift using the relation $\Delta\omega = \Delta T \times 4.47$ GHz which stands in this temperature region (cf Fig.5.15). The plot also shows the curve fit result with $T(t) = (T_{Final} - T_{Initial})\exp(-t/\tau) + T_{Final}$. In both 100 mJ/cm^2 and 50 mJ/cm^2 cases, the thermal time constant τ was 11 ps to12 ps. As stated before, the observed frequency change occurs due to the change in the electron temperature of Er^{3+}. Therefore, from this experimental result, it was found out that the heating of the Er^{3+} electrons occurs with time constant of roughly 11 ps. This value is close to the time necessary to pass the energy from the lattice to Er^{3+} electrons, 15 ps, given from the reference [20] which was estimated from the timing the spin reorientation occurred as a result of the pumping pulse. According to this report, the energy transfer from Fe^{3+} electrons to the lattice ends within 500 fs due to the strong coupling between the $3d$ electrons and the lattice. Therefore, the time constant of 11 ps can be regarded as the time required for the lattice to transfer the energy to the Er^{3+} electrons. For this reason, the time constant can be represented by

$$\tau = C_e/g, \tag{5.3}$$

where g is the electron-phonon coupling constant between the Er^{3+} electrons and the lattice, and C_e is the specific heat of the erbium electron system.

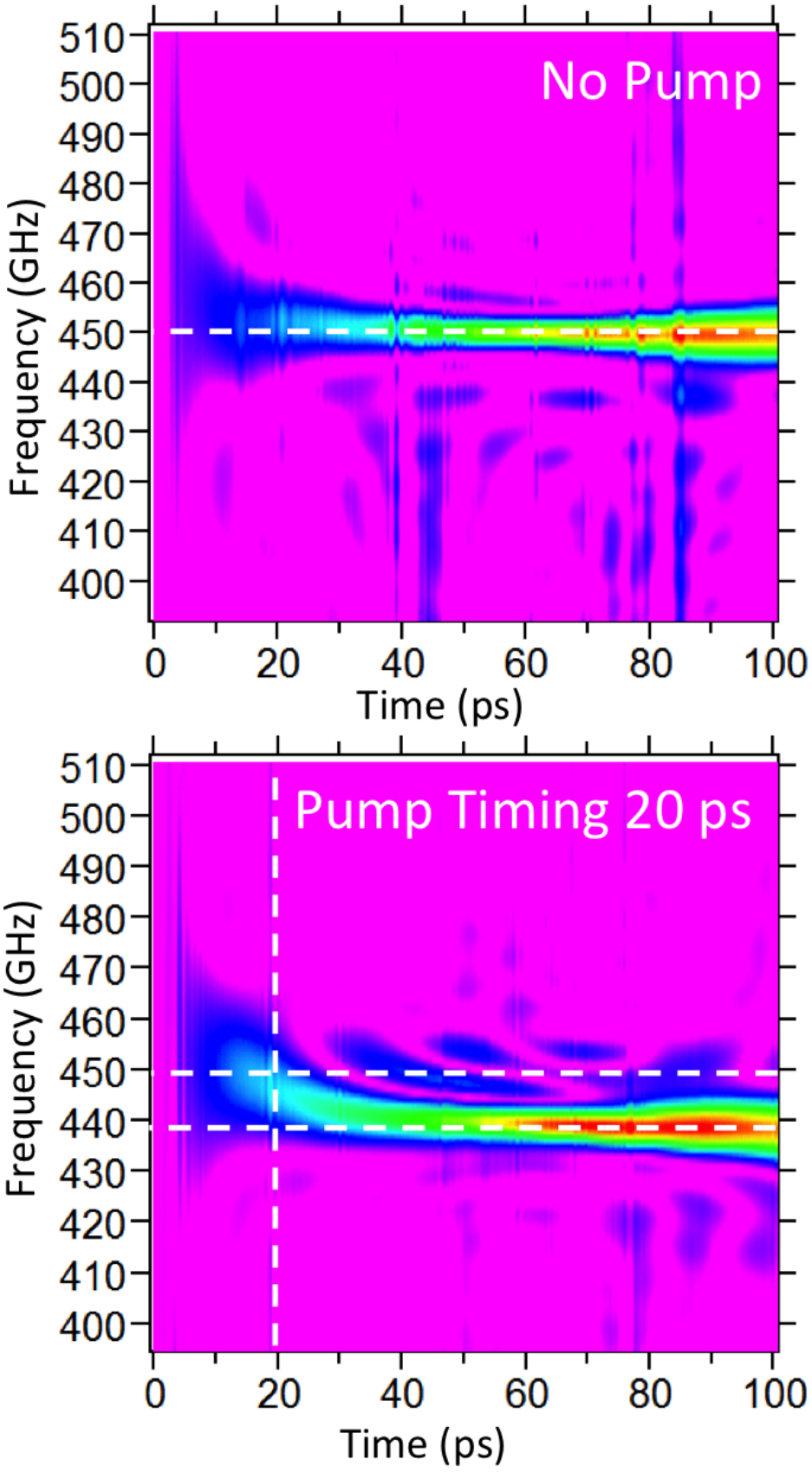

FIG. 5.32 Time-frequency distributions of the pump probe experiment with $ErFeO_3$ at 30 K shown in Fig.5.30

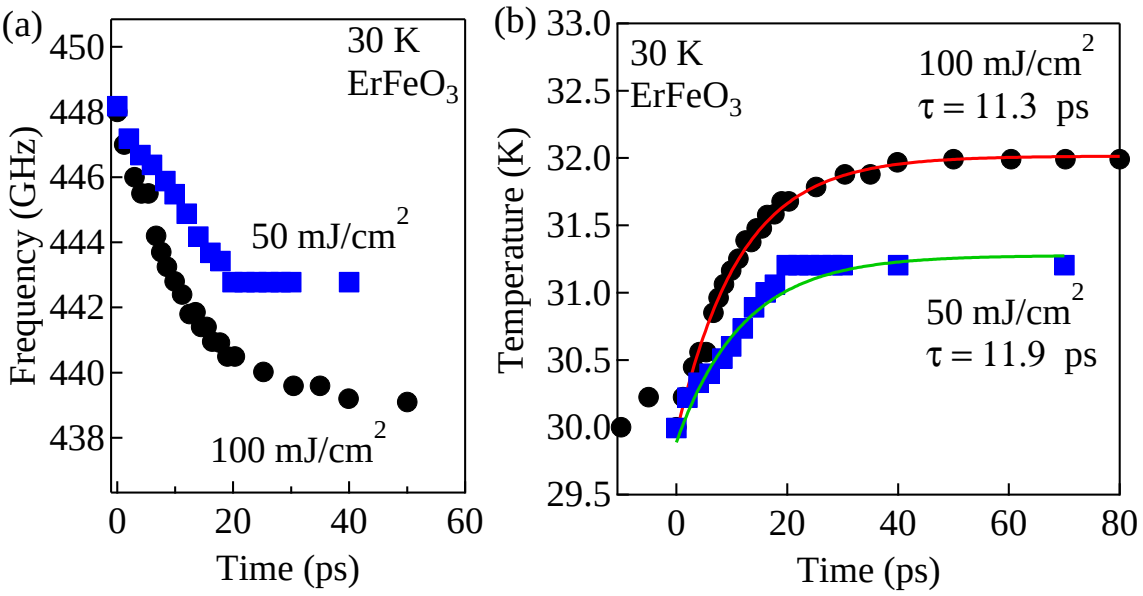

FIG. 5.33 (a) Temporal dependence of the F mode resonance frequency shift induced by pumping pulse of 100 mJ/cm^2 and 50 mJ/cm^2 fluences. The instant pumping pulse arrived at the sample is set as 0 ps. (b) The temperature change converted from the frequency shift in (a).

With the pump-probe experiment at 5 K, similar behavior of the Er^{3+} electron temperature was observed (Fig.5.34). Here, the time constant 19.8 ps is slightly higher than that in 30 K. This can be explained by the decrease in the population of the phonons which results from temperature decrease. Since the phonons mediate the electron phonon scattering [74], decrease of the phonons will result in slower time constant.

Similar experiment was also conducted on a $DyFeO_3$ single crystal. In this sample, as mentioned before, the frequency of the AF mode is highly dependent on the temperature. In order to excite AF mode with THz pulse and observe the AF mode motion with the Faraday rotation, (101) sample with 100 μm thickness was prepared. The result of this measurement is shown in Fig.5.35. As the figure shows, similar to the case of $ErFeO_3$, after excitation with the pumping pulse, picosecond timescale heating of the rare-earth electron temperature is observed. In this case, the thermal time constant is 50.3 ps, which is much larger than the case of $ErFeO_3$. From this result, it can be deduced that the electron-phonon coupling of the Dy^{3+} is much weaker than that of Er^{3+}. According to the work reported in the past, lanthanide-ion series (La, Ce, Pr, Nd, Pm, Sm, Eu, Gd, Tb, Dy, Ho, Er, Tm, Yb, Lu, arranged

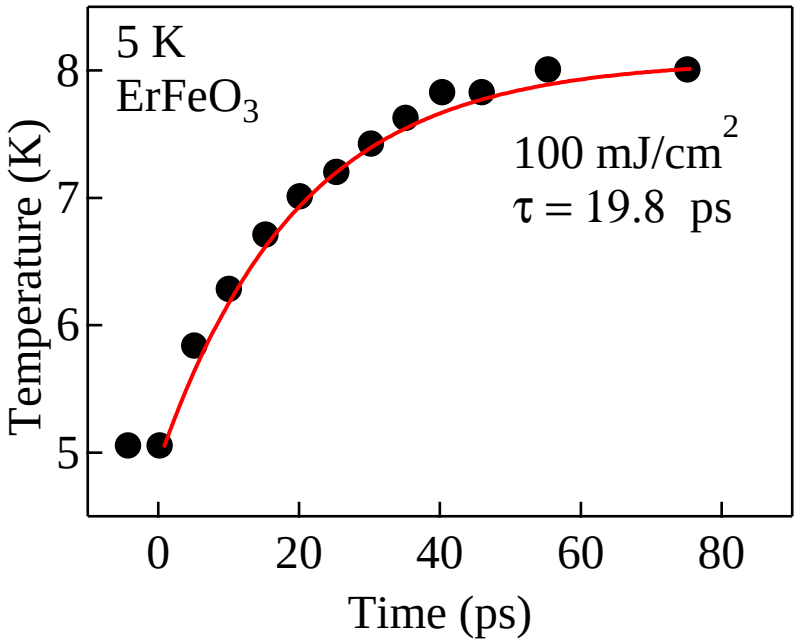

FIG. 5.34 Temporal dependence of the Er^{3+} electron temperature as a result of pumping pulse irradiation. The pump pulse arrived at the $ErFeO_3$ sample at 0 ps.

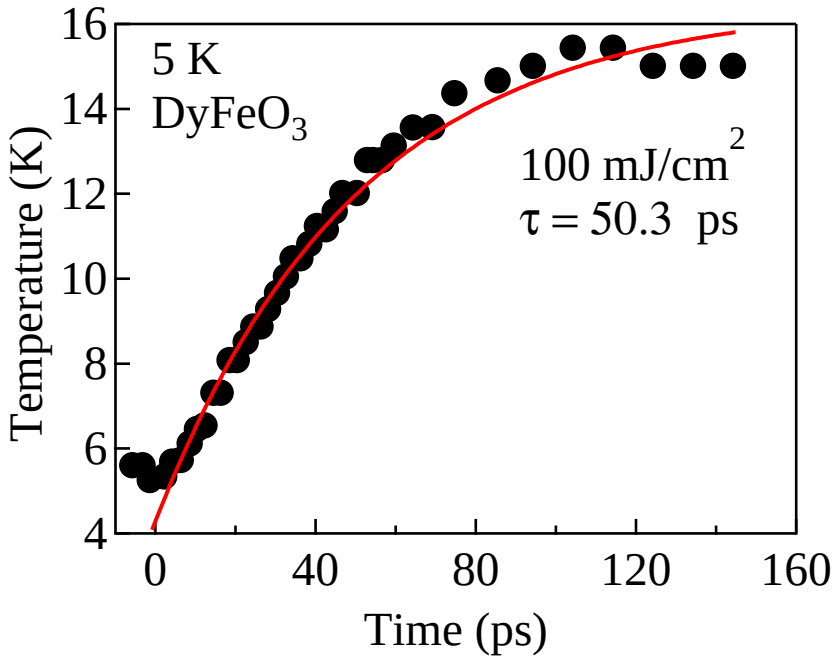

FIG. 5.35 Temporal dependence of the Dy^{3+} electron temperature obtained from the AF mode frequency shift in the pump-probe experiment on $DyFeO_3$ (101) sample. The pump pulse arrived at the sample at 0 ps.

in ascending order of the number of 4*f* electrons) have stronger electron-phonon coupling at the beginning (La and Ce) and at the end (Yb and Lu) of the series. As the number of the 4*f* electrons approach 7 (Gd), the electron-phonon coupling tends to become weaker [75]. In the case of this experiment, Dy^{3+} is more closer to the center of the series compared to Er^{3+} and therefore weaker electron-phonon coupling is expected for Dy^{3+} 4*f* electrons. This reported behavior of the electron-phonon coupling in the lanthanide-ion series is consistent with the result obtained from the pump-probe experiment shown here and supports that the difference in the temperature rise time between $ErFeO_3$ and $DyFeO_3$ is due to the difference in the electron-phonon coupling of the rare-earth ion 4*f* electrons.

As shown here, by combining the Faraday rotation of the visible probe pulses, THz induced spin precession can be used to observe effects such as photoinduced ultrafast heating of the spin system. Unlike the method reported by the past research [20] where the time lag of the ultrafast spin reorientation against the pumping pulse arrival time is measured, the method used here possesses an advantage which enables the direct measurement of the rare-earth electron temperature at each instant of time, even in the region far from the spin reorientation temperature.

Chapter6

Excitation of the Spins with Intense THz Pulses

In this chapter, the spin dynamics induced by high power THz pulse generated from $LiNbO_3$ will be presented. Part of the results which employed the optical pumping was already shown in the previous chapter. Therefore, this chapter will focus solely on the effect of the THz pulse.

In these experiments, THz pulse focused to roughly 300 μm diameter was used to induce spin precession motion in single crystal orthoferrites. In order to observe the motion of the excited spin precessions, Faraday rotation of a probe pulse (<1 μJ/pulse, λ = 800 nm) with a spot diameter of approximately 30 μm was measured. Since the magnetic domain size of the samples used here were several hundred μm, the probe pulse of this size can be used to observe the single domain spin dynamics.

6.1 Spin Dynamics in $DyFeO_3$

In this section, spin dynamics in $DyFeO_3$ single crystal (101) sample with thickness of 100 μm was observed. As stated in the previous chapter, in both high temperature spin configuration and low temperature configuration, F mode and AF mode can be excited by THz magnetic component parallel to a axis and c axis, respectively. First, measurements were conducted at room temperature with the following two experimental configurations: $H_{THz} \parallel b$ polarization shown in Fig.6.1(a) and $H_{THz} \parallel a + c$ polarization shown in Fig.6.1(b). Figures6.2(a) and (b) show the result of this experiment at room temperature. At time 0 ps,

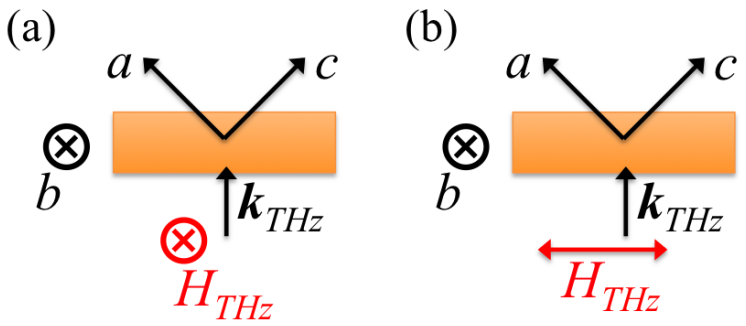

FIG. 6.1 Experimental configuration for (a) $H_{THz} \parallel b$ polarization and (b) $H_{THz} \parallel a + c$ polarization THz pulse excitation of $DyFeO_3$.

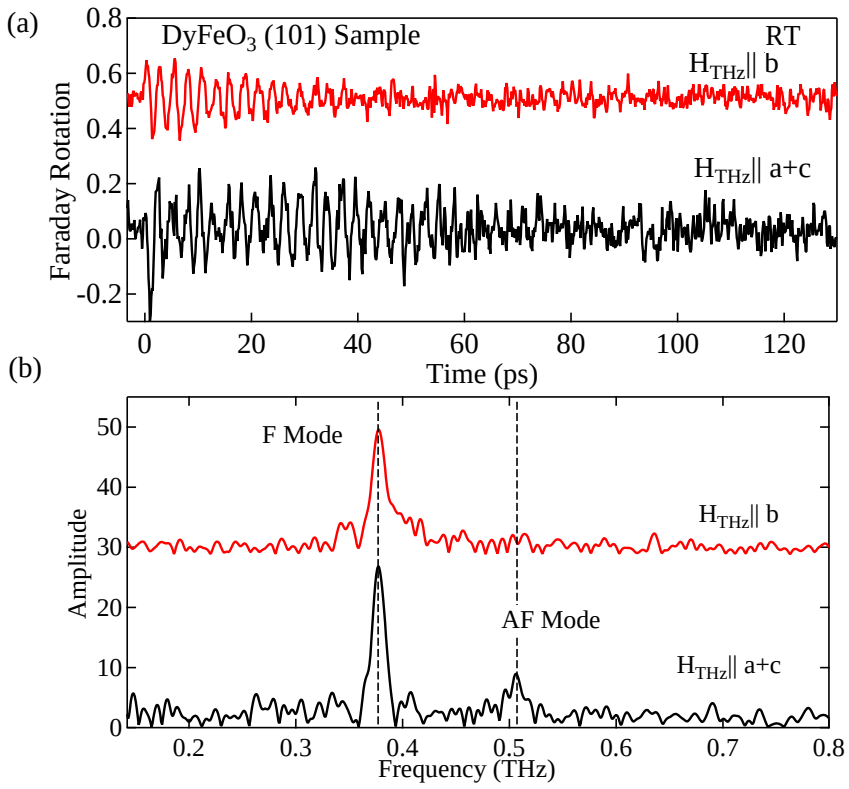

FIG. 6.2 (a) The time dependent THz induced Faraday rotation signal obtained with (101) $DyFeO_3$ single crystal at room temperature. (b) The Fourier spectra of the waveforms in (a).

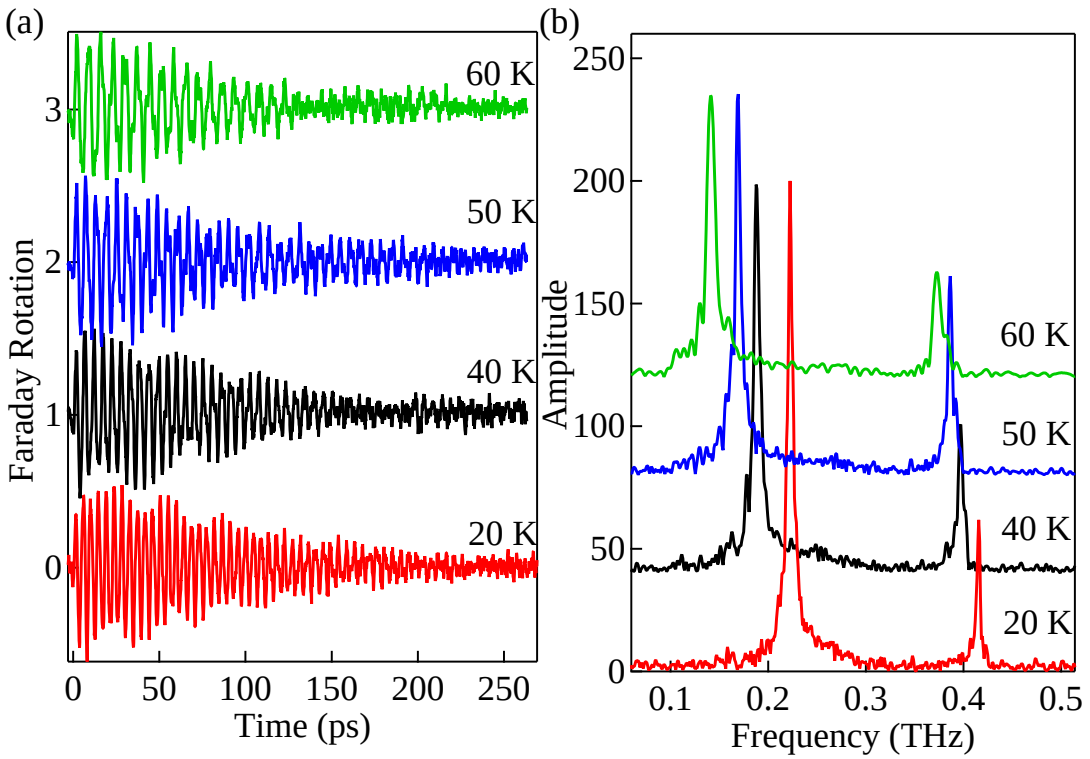

FIG. 6.3 (a) The time dependent THz induced Faraday rotation signal obtained with (101) $DyFeO_3$ single crystal at 20 K, 40 K, 50 K, 60 K. (b) The Fourier spectra of the waveforms in (a).

the THz pulse arrives at the sample and excites the precession (Fig.6.2(a)). As expected, $H_{THz} \parallel b$ polarization excites F mode resonance and $H_{THz} \parallel a + c$ polarization (parallel to $(10\bar{1})$ direction) results in simultaneous excitation of both F and AF mode.

As a next step, the spin dynamics in the low temperature phase was observed with $H_{THz} \parallel a + c$ polarization. Figure6.3 shows the temporal Faraday rotation signals and their Fourier spectra at 20 K, 40 K, 50 K, and 60 K. All of these temporal waveforms show beating which is due to the coexisting F and AF mode, which can be observed in the spectra. The figure show that the spin precession lasts for about 200 ps, which is quite long compared to the result obtained with the THz-TDS. For example, the line width of AF and F mode at 20 K in this experiment was 6.3 GHz and 4 GHz, respectively. On the other hand, the line width of AF and F mode obtained from the THz-TDS was 15 GHz and 10 GHz, respectively (Fig.5.21). This discrepancy with the THz-TDS result may be due to the difference in the size of the observed area. In the previous THz-TDS experiments, spin precession inside large

area covered by THz spot size (1- 4 mm diameter) was summed up and observed. Therefore, spatial dependence of the resonance frequency due to inhomogeneity of the samples such as defects should have been averaged in the previous case, leading to a superficial decrease in the lifetime of the precession. On the other hand, since spin precession inside small area of roughly 30 μm in diameter is observed in this chapter, such superficial decrease of life time is expected to be considerably smaller than the previous cases.

Increasing the temperature above 60 K, the amplitude of the oscillation shows sudden decrease (Fig.6.4(a)). Closer observation of the waveforms at 61 K and 62 K show that small amplitude oscillations still persist (Fig.6.4(b)). The spectra in Fig.6.4(c) show that this sudden decrease of the oscillation is due to the sudden decrease of the AF mode (lower peak) peak amplitude. At 61 K, the amplitude of the AF mode peak becomes very small, and at 62 K, the peak cannot be observed at all. It was shown in the previous chapter that when the spin configuration changes from the low temperature configuration to the high temperature configuration, the AF mode peak amplitude decreases abruptly. Therefore, the spin reorientation transition temperature in this case is at around 61 K. In the previous chapter, we have seen that the spin reorientation temperature of $DyFeO_3$ was about 65 K, which differs for about 4 K with the result obtained here. For comparison, Fig.6.5 shows the temperature dependence of the AF mode peak spectra obtained with the THz-TDS experiment (weak excitation). This figure shows that the AF mode peak is clearly visible at 65 K and as the temperature is lowered to 63 K, the peak value grows significantly. This behavior obviously does not match with the result obtained in this experiment. The relative oscillator strength obtained from these two experiments also clearly show that the temperature dependence of both the AF mode and F mode peak suggest lower reorientation temperature for high intensity THz experiment (Fig.6.6).

In the previous chapter we have also seen that application of external magnetic field along the *c* axis lowers the reorientation temperature. However, unlike these experiments, the result shown here was obtained with no magnetic field applied. The only magnetic field applied to the sample is the magnetic field component of the THz pulse. One possible explanation for such a situation is that the reorientation temperature shift observed here is caused by the THz magnetic field.

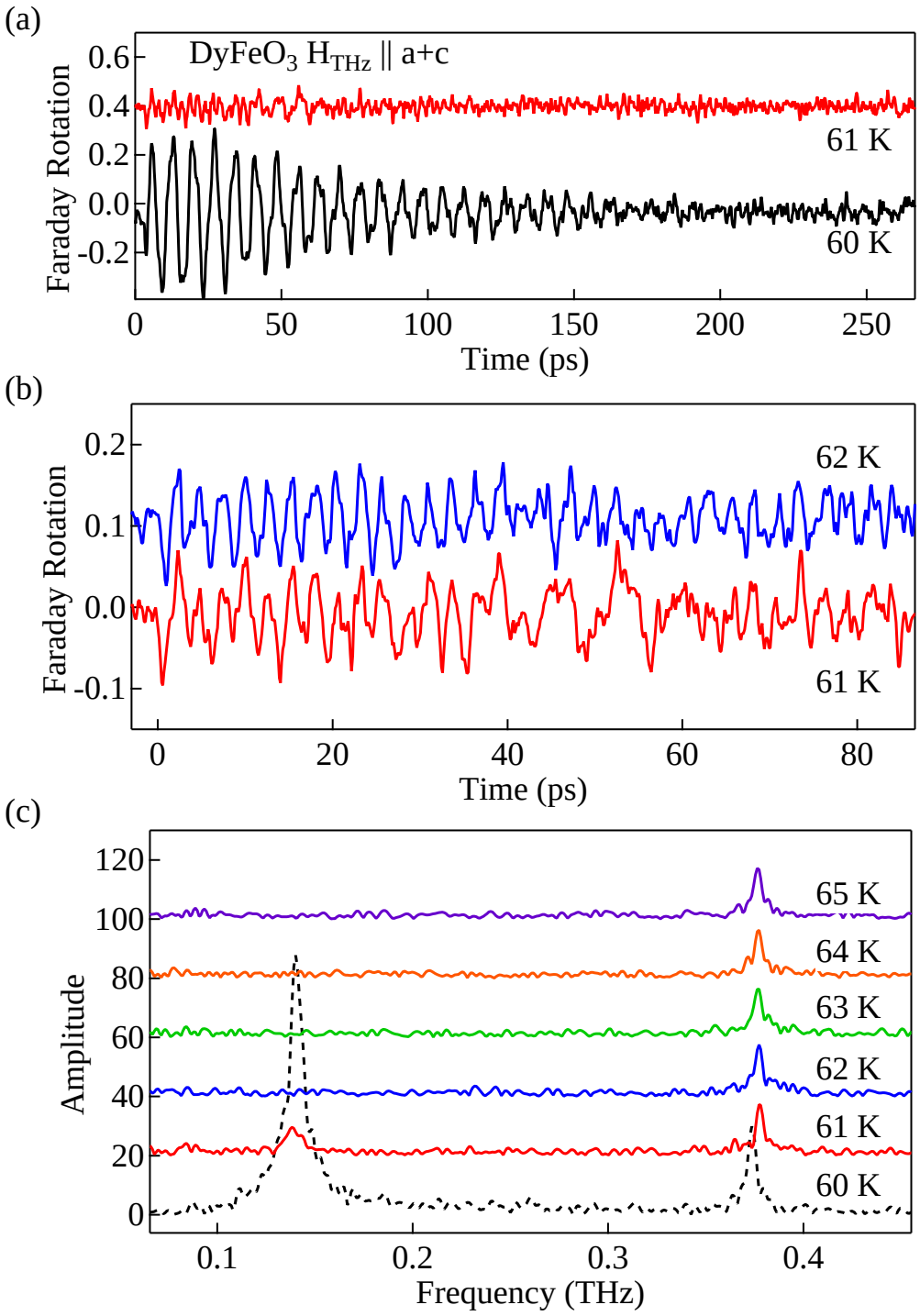

FIG. 6.4 (a) The time dependent THz induced Faraday rotation signal obtained with (101) $DyFeO_3$ single crystal at 60 K and 61 K. (b) The temporal Faraday signal obtained at 61 K and 62 K. (c) Fourier spectra at 60 K, 61 K, 62 K, 63 K, 64 K and 65 K. The electric field strength of the incident THz pulse was 240 kV/cm.

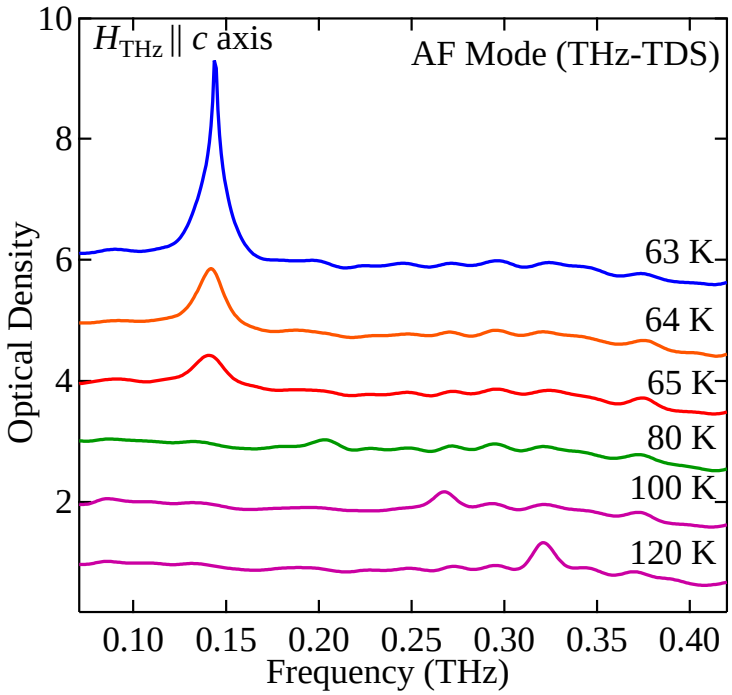

FIG. 6.5 The optical density spectra of AF mode resonance obtained with THz-TDS measurement at various temperature.

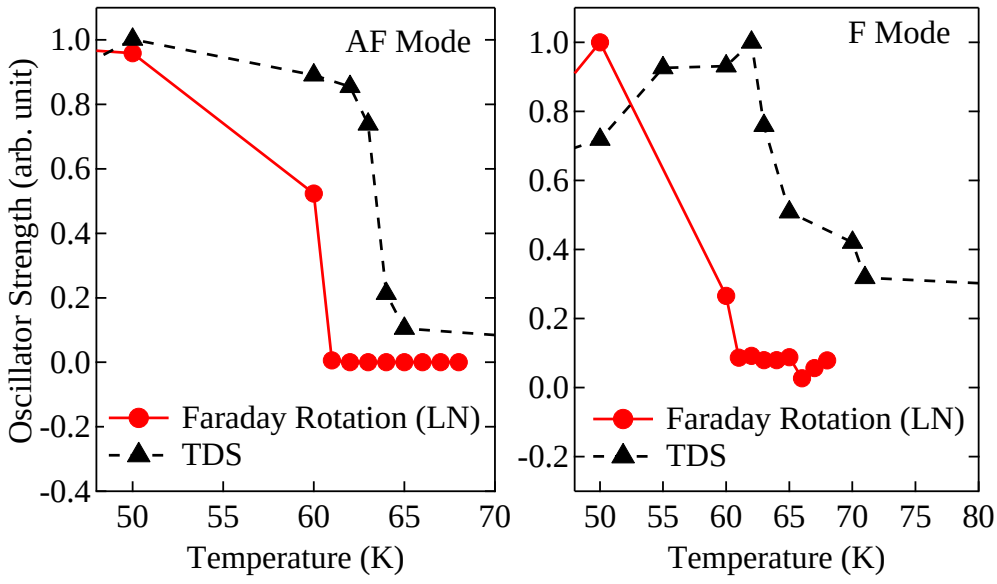

FIG. 6.6 Temperature dependence of the relative oscillator strength obtained with high intensity THz pulse excitation and THz-TDS (weak THz pulse). The oscillator strength with high intensity THz was derived from the data shown in Fig.6.4(c). For the oscillator strength with weak THz pulse (THz-TDS), the data shown in Fig.5.19(b) ($H_{THz} \parallel c$ for AF mode, and $H_{THz} \parallel a$ for F mode) were used.

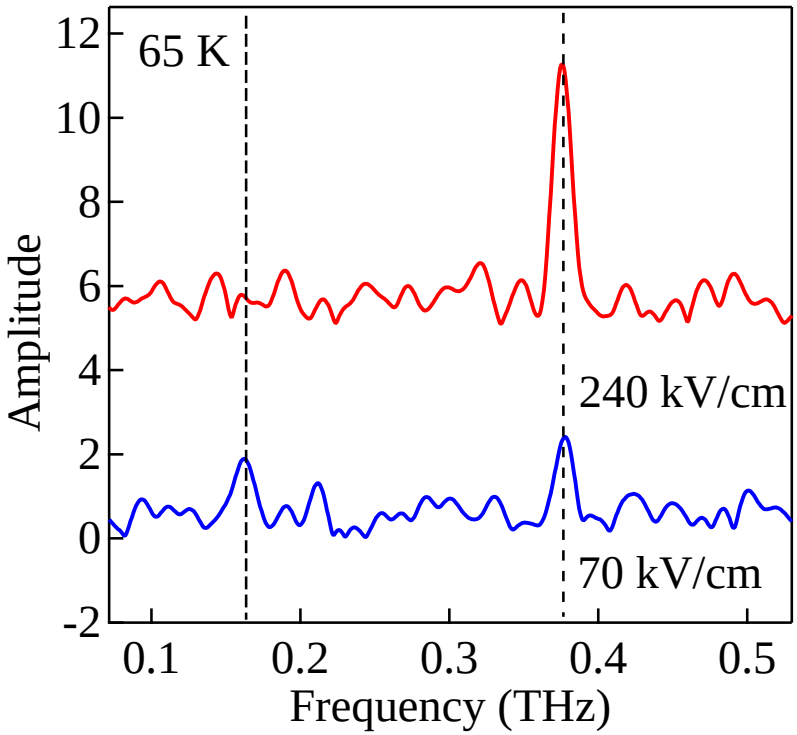

FIG. 6.7 The Fourier spectra of the time dependent Faraday rotation obtained at 65 K.

Another possibility is the heating due to absorption of THz pulse. However, as the following estimation shows, the temperature increase due to the THz absorption is much smaller than the observed reorientation temperature shift. The energy density of the THz pulse with 240 kV/cm electric field is $\varepsilon_0 E^2 = 51 \times 10^2$ J/m^3. The volume of a single THz pulse with a spot diameter of 300 μm and temporal duration of 0.5 ps is $\pi \times (150 \times 10^{-6})^2 \times 0.5 \times 10^{-12} \times 3 \times 10^8 = 10^{-11}$ m^3. Therefore, the single THz pulse total energy can be estimated to be about 51 nJ. The heat capacity of $DyFeO_3$ at around 60 K is about 20 JK^{-1}mol^{-1} [76]. Because the THz pulses transmits through the $DyFeO_3$ well, the sample with thickness of 100 μm is expected to be heated uniformly by the THz pulse. Thus, the sample volume inside the 300 μm diameter THz spot is 7×10^{-12} m^3. Using the lattice constant of $a = 0.5$ nm, $b = 0.5$ nm and $c = 0.7$ nm [38], the heat capacity of the sample with a volume of 7×10^{-12} m^3 is roughly 5.4 μJ/K. Thus, even if all of the THz pulse energy is absorbed by the sample, the temperature increase is only $51 \times 10^{-9}/5.4 \times 10^{-6} = 9.4 \times 10^{-3}$ K and this cannot explain the shift of the reorientation temperature which was about 4 K. In addition, since most part of the THz energy is transmitted through the sample without being absorbed, the actual temperature

increase is expected to be much smaller than this estimation.

When the THz amplitude is reduced to about 30 % of the value maximum amplitude, as Fig.6.7 shows, a peak which appears to be like an AF mode peak is observed. This change is equivalent to the increase of the reorientation transition temperature. Therefore, this result is consistent with the above picture that the THz magnetic field along the c axis causes the reorientation temperature shift.

6.2 Spin Dynamics in $ErFeO_3$

An $ErFeO_3$ (001) single crystal was selected as the sample. The thickness of the sample was 100 μm. THz pulses with $H_{THz} \parallel b$ axis polarization was incident to the sample. Since in the high temperature Γ_4 phase (G_x, A_y, F_z structure), THz pulse with this polarization can only excite F mode resonance, that is, a precession of macroscopic magnetization inside ab plane (Fig.6.8). Therefore, in this configuration, no oscillation can be observed with the Faraday rotation. However, in the low temperature Γ_2 phase (F_x, C_y, G_z structure), excited F mode incorporates magnetization oscillation along the c axis direction (Fig.6.8). Thus, the F mode precession can be observed through the Faraday effect of the probe pulse. Such behavior was actually confirmed experimentally (Fig.6.9). From the figure, it can be seen that oscillation of the Faraday rotation occurs after the arrival of THz pulse at 0 ps.

As the temperature is lowered, for example at 70 K, the lifetime of the oscillation becomes increasingly long (Fig.6.10). In this temperature range, the precession lasts for over several hundred picosecond, which is far larger than the life time of the F mode resonance (< 40 ps) obtained with THz-TDS transmission experiments. Therefore, similar to the case of $DyFeO_3$, it can be interpreted that the lifetime of the spin precession in $ErFeO_3$ obtained with the THz-TDS measurement is superficially degraded by inhomogeneity such as defects in the crystal.

6.2.1 Beating of the F mode Resonance

Another striking aspect of the result shown in Fig.6.10 is a 50 ps period beating of the oscillation and sudden increase of oscillation amplitude starting from 200 ps. These behaviors were not observed in the experiments described in the previous chapters, and to the extent

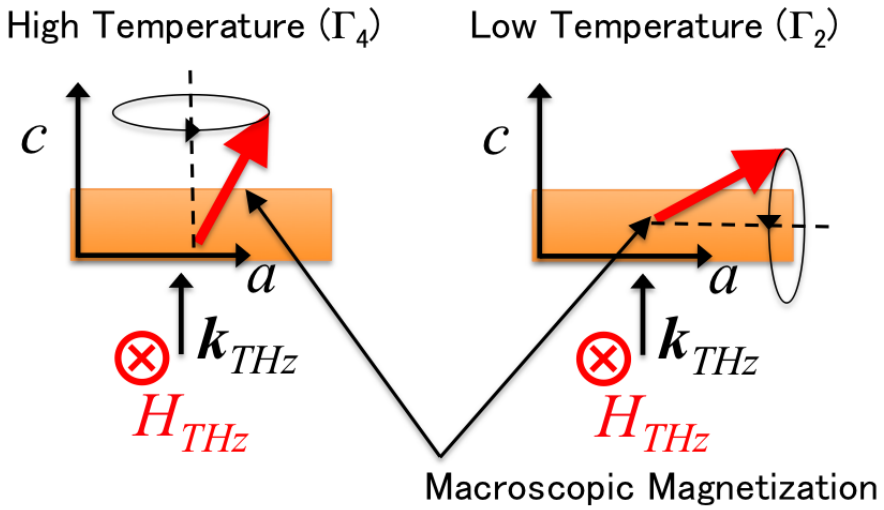

FIG. 6.8 Experimental configuration of THz pump- visible Faraday probe experiment with $ErFeO_3$. Excited F mode precession of the macroscopic magnetization in high and low temperature spin configuration is also described.

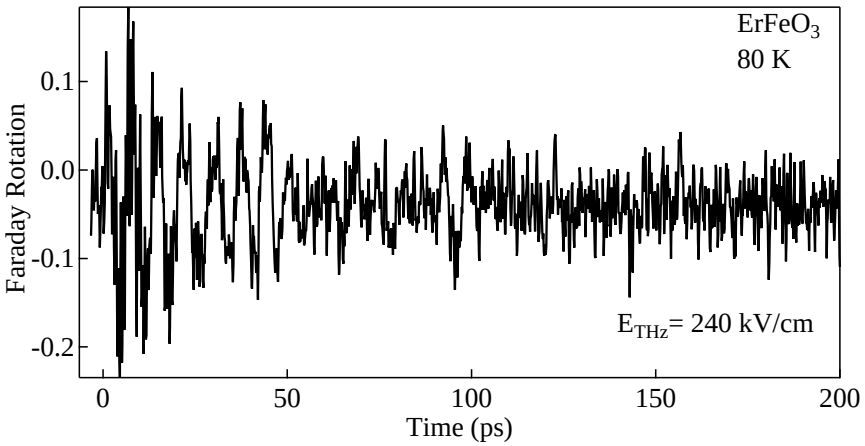

FIG. 6.9 The time dependent THz induced Faraday rotation signal obtained with (001) $ErFeO_3$ single crystal at 80 K.

of the author's knowledge, no similar reports have been made in the past. Unlike in the experiment with $DyFeO_3$ (101) sample, AF mode resonance is not excited nor observed in this experimental condition and therefore this beat signal cannot be ascribed to the coexistence of the F and AF mode oscillations. From the Fourier spectra of this data, it can be verified that AF mode peak (approximately 0.8 THz) does not exist (Fig.6.11). Instead, the F mode resonance at around 0.2 THz is split into two peaks with a separation of about 18.3 GHz and this split is responsible for the observed beating with 50 ps period. As the result obtained

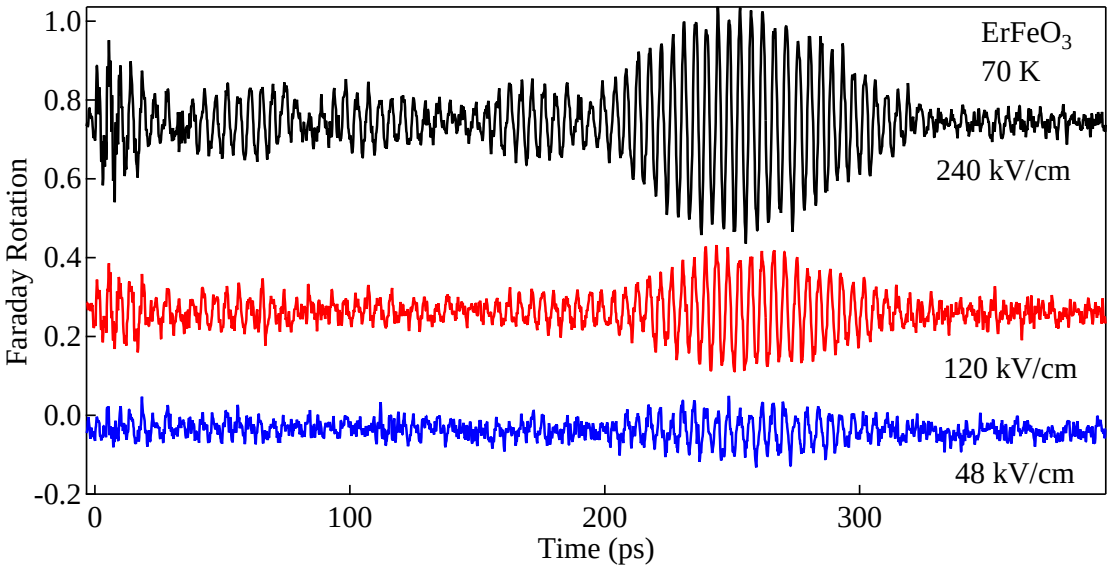

FIG. 6.10 The time dependent THz induced Faraday rotation signal obtained with (001) $ErFeO_3$ single crystal at 70 K.

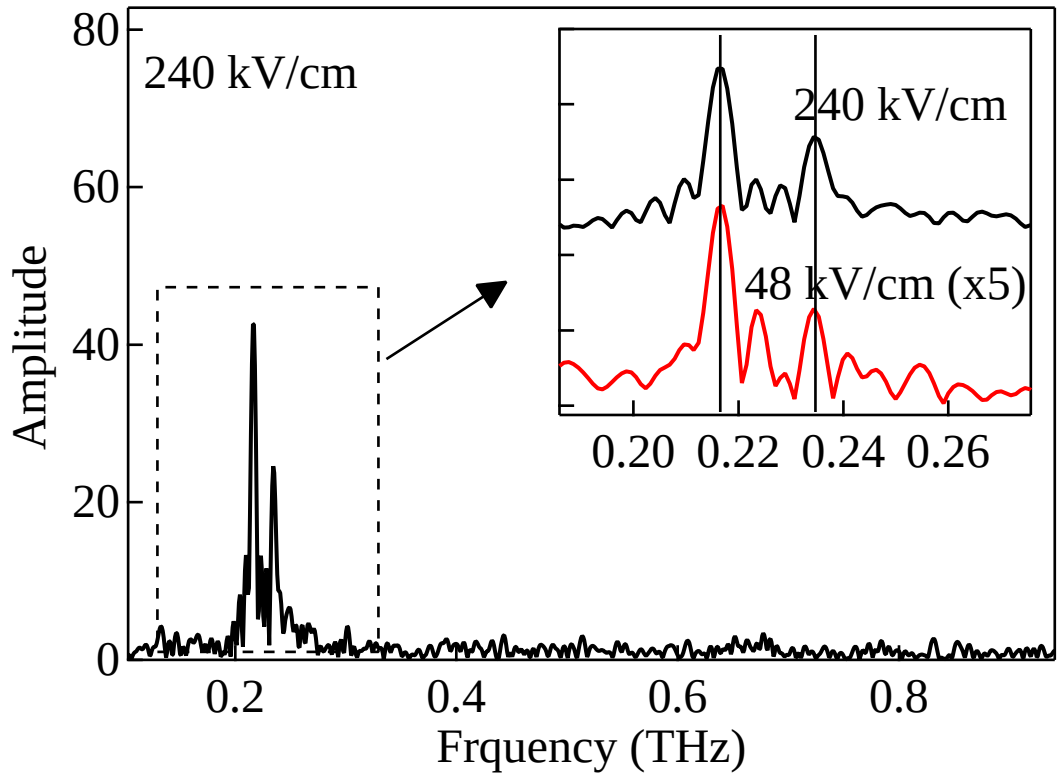

FIG. 6.11 The Fourier spectra of the time dependent Faraday rotation in $ErFeO_3$ at 70 K.

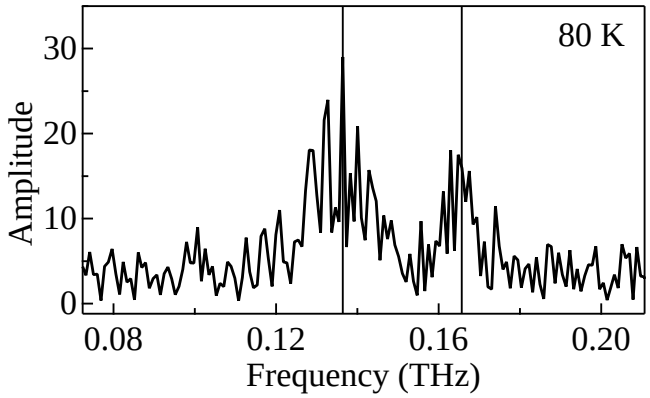

FIG. 6.12 The Fourier spectra of the waveform measured in $ErFeO_3$ at 80 K. The temporal waveform is shown in Fig.6.9.

with different THz pulse amplitude in Fig.6.10 show, the beating and the amplitude increase still exists with lower THz amplitude of approximately 120 kV/cm and 48 kV/cm. Although the beating is difficult to be recognized due to low signal to noise ratio with 48 kV/cm THz pulse, the split peaks can still be observed in the Fourier spectra (Fig.6.11). Also, while it cannot be clearly observed in the temporal waveform in Fig.6.9, spectra at 80 K also shows similar splitting of the F mode (Fig.6.12). The amount of split at 80 K is 28 GHz and this is somewhat larger than the splitting observed at 70 K.

Decreasing the temperature further more, similar beatings and amplitude increase can still be seen (Fig.6.13). In the temperature range such as 20 K and 30 K, the lifetime of the oscillation is extremely long and lasts for more than 1 nanosecond. The spectra in Fig.6.13(c) show that the splitting of the F mode resonance peak exists also in these temperatures. The amount of splitting shows temperature dependence and as the temperature reduces, the splitting also reduced. The splitting at each temperature is listed in Table6.1. As mentioned previously, existence of such splitting of the F mode resonance has never been reported before.

Although there are several known mechanisms that can cause multiple lines of the magnetic resonance modes, they do not seem to match the splitting observed here. For example, when an uniform precession spin wave mode is excited in a thin sample, standing spin wave along the thickness direction is known to be excited. Such $k \neq 0$ spin waves have resonant frequency higher than the uniform precession mode. However, the sample thickness of 100 μm used in this experiment is too thick and such spin wave modes should be obscured by the line width

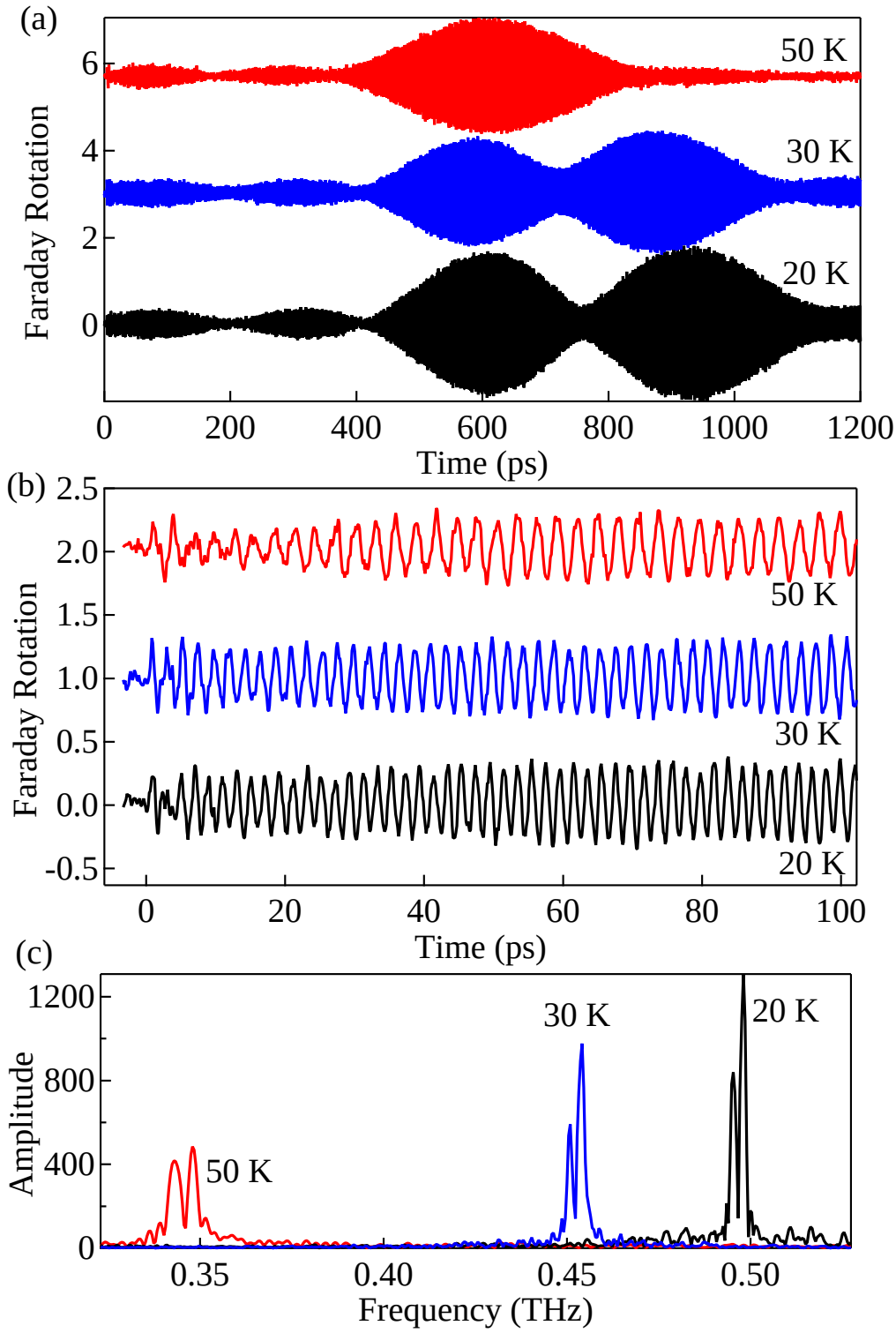

FIG. 6.13 The time dependent THz induced Faraday rotation signal obtained with (001) $ErFeO_3$ single crystal at 50 K, 30 K, and 20 K. (a) The Faraday rotation signal from 0 ps to 1200 ps. (b) The Faraday rotation signal from 0 ps to 100 ps. Oscillations due to F mode resonance can be resolved. (c) The Fourier spectra of the temporal waveforms in (a).

of the uniform mode [77].

The magnetic resonance modes are also known to split under existence of a magnetic domain walls [50]. However, in our case, this mechanism was experimentally denied. As stated in chapter 3, the magnetic domains in the sample used here can be uniformly aligned with an external magnetic field of roughly 0.01 T. Figure6.14(a) shows that the splitting exists even when the magnetic domain structure is cancelled by sufficiently strong external magnetic field (about 0.1 T) along the *a* axis direction. A shift of the two peaks proves that the external magnetic field is applied to the sample. The effect of the magnetic field can also be observed in the temporal waveforms in Fig.6.14(b). Since reversing the external magnetic field resulted in the inversion of the phase of the precession, the applied magnetic field is sufficient for aligning the magnetic domains. Therefore, it can be expected that no magnetic domain walls exist inside the probed area. Persistence of the splitting in spite of these responses against the external magnetic field suggests that this mode splitting cannot be ascribed to the splitting due to magnetic domain walls.

Here, instead of these known mechanisms, a novel splitting mechanism due to the Dzyaloshinskii-Moriya interaction is proposed. The basic idea of this mechanism is as follows. As stated in chapter 2, orthoferrites have four different Fe^{3+} sublattice spins (Fig.6.15(a)). When focusing on the dynamics of spin sublattice 1, interactions with the nearest neighbor spins, that is spin 2 and spin 4, will suffice. Owing to the two types of canting, the overt canting and the hidden canting, the canting angle θ between spin 1 and 2 and the canting angle θ' between spin 1 and spin 4 are slightly different (Fig.6.15(b)). This slight difference is due to the small difference in the Dzyaloshinkii-Moriya interaction between spin pairs 1-2 and 1-4. Such small variation of the Dzyaloshinskii-Moriya interaction is usually ignored in the commonly used two-sublattice approximation, but it can be expected to cause splitting of the magnetic resonant frequency.

For more detailed discussion, we will first figure out the direction of the Dzyaloshinskii vector. From the conclusion of Moriya's work [43], Dzyaloshinskii-Moriya interaction between two spins at point A and B is known to be determined by the symmetry between the A and B. Dzyaloshinskii vector is known to follow the following rules:

1. $\boldsymbol{D} = 0$ when a center of inversion is located at the point halfway between A and B.

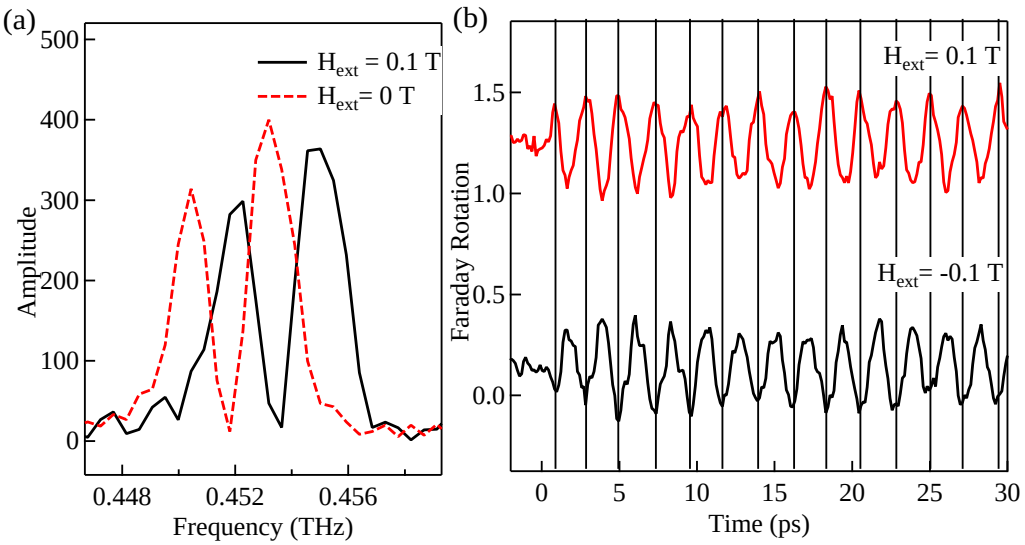

FIG. 6.14 (a) The spectra of Faraday rotation in $ErFeO_3$ at 30 K with and without external magnetic field along a axis. (b) Comparison of the spin dynamics in the first 30 ps with external magnetic applied along $+a$ and $-a$ direction.

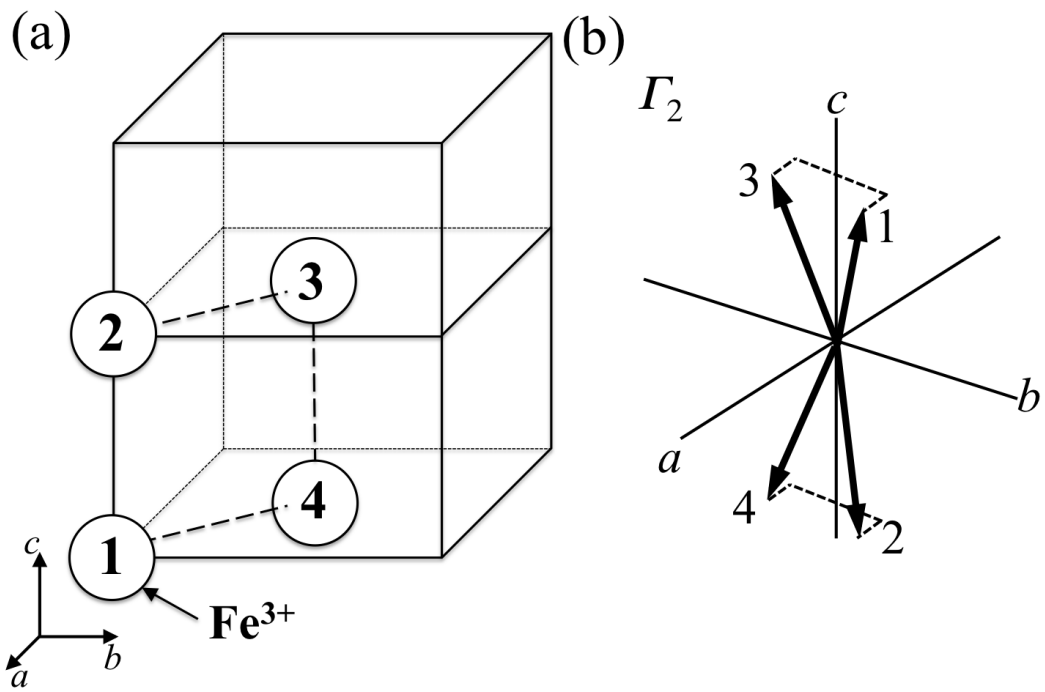

FIG. 6.15 (a) Crystallographic structure of orthoferrites and position of the four Fe^{3+} sublattices. (b) Low temperature spin configuration in $ErFeO_3$.

Table6.1 The split F mode resonant frequency at each temperature

Temperature (K)	Frequency 1 (GHz)	Frequency 2 (GHz)	Splitting (GHz)
80	136	164	28
70	216.1	234.4	18.3
50	342.8	347.9	5.1
30	450.9	454.1	3.2
20	495.3	498.1	2.8

2. $\boldsymbol{D} \parallel \boldsymbol{m}$ when mirror plane $\boldsymbol{m}$ bisects A and B.
3. $\boldsymbol{D} \perp \boldsymbol{m}$ when A and B is inside a mirror plane $\boldsymbol{m}$.
4. $\boldsymbol{D} \parallel$ two-fold axis when a two fold axis passes through the midpoint of A and B.
5. $\boldsymbol{D} \parallel$ AB when n-fold axis is along AB.

In addition, these conditions also holds for glide planes instead of mirror planes [44].

Close observation of the crystal structure (Fig.2.6) reveals that sublattices 1 and 2 can be transformed into each other with a mirror plane parallel to *ab* plane. Similarly, sublattices 1 and 4 are transformed to each other by a *b* glide with a mirror plane parallel to *bc* plane. Therefore, consulting to the above rules, the Dzyaloshinskii vectors between the two pairs of sublattices are:

$$\boldsymbol{D}_{12} = \begin{pmatrix} D_x \\ D_y \\ 0 \end{pmatrix}, \tag{6.1}$$

$$\boldsymbol{D}_{14} = \begin{pmatrix} 0 \\ D'_y \\ D'_z \end{pmatrix}. \tag{6.2}$$

From the relation of the overt canting and hidden canting [48], all of the Dzyaloshinskii constants in equations (6.1) and (6.2) is expected to take close values.

When considering these Dzyaloshinskii vectors, the following terms should be added to the equation of motion (2.27) in 2.2.2.

$$-i[s_{1x}, \boldsymbol{D}_{12} \cdot (\boldsymbol{s}_1 \times \boldsymbol{s}_2)] = 2D_x(s_{1z}s_{2z} + s_{1y}s_{2y}) - 2D_y s_{1y}s_{2x} \tag{6.3}$$

$$-i[s_{1y}, \boldsymbol{D}_{12} \cdot (\boldsymbol{s}_1 \times \boldsymbol{s}_2)] = -2D_x s_{1x}s_{2y} + 2D_y(s_{1x}s_{2x} + s_{1z}s_{2z}) \tag{6.4}$$

$$-i[s_{1z}, \boldsymbol{D}_{12} \cdot (\boldsymbol{s}_1 \times \boldsymbol{s}_2)] = -2D_x s_{1x}s_{2z} - 2D_y s_{1y}s_{2z} \tag{6.5}$$

$$-i[s_{1x}, \boldsymbol{D}_{14} \cdot (\boldsymbol{s}_1 \times \boldsymbol{s}_4)] = -2D'_y s_{1y}s_{4x} - 2D'_z s_{1z}s_{4x} \tag{6.6}$$

$$-i[s_{1y}, \boldsymbol{D}_{14} \cdot (\boldsymbol{s}_1 \times \boldsymbol{s}_4)] = 2D'_y(s_{1x}s_{4x} + s_{1z}s_{4z}) - 2D'_z s_{1z}s_{4y} \tag{6.7}$$

$$-i[s_{1z}, \boldsymbol{D}_{14} \cdot (\boldsymbol{s}_1 \times \boldsymbol{s}_4)] = -2D'_y s_{1y}s_{4z} + 2D'_z(s_{1y}s_{4y} + s_{1x}s_{4x}) \tag{6.8}$$

$-i[\boldsymbol{s}_2, \boldsymbol{D}_{12} \cdot (\boldsymbol{s}_1 \times \boldsymbol{s}_2)]$, and $-i[\boldsymbol{s}_4, \boldsymbol{D}_{14} \cdot (\boldsymbol{s}_1 \times \boldsymbol{s}_4)]$.

In the case of this experiment, the spin orientation is Γ_2. Therefore, $s_{1z} \approx 1$, $s_{2z} \approx -1$, $s_{4z} \approx -1$ and $s_{ix,iy} \ll 1$. Since the motion in z axis component is small compared to the motion inside xy plane, we will concentrate only on the motion of x axis component and y component. Dropping the constant terms and higher order terms $s_{ix}s_{jx}$, $s_{ix}s_{jy}$ and $s_{iy}s_{jy}$,

$$-i[\boldsymbol{s}_1, \boldsymbol{D}_{12} \cdot (\boldsymbol{s}_1 \times \boldsymbol{s}_2)]_x = -i[\boldsymbol{s}_2, \boldsymbol{D}_{12} \cdot (\boldsymbol{s}_1 \times \boldsymbol{s}_2)]_x = 0 \tag{6.9}$$

$$-i[\boldsymbol{s}_1, \boldsymbol{D}_{12} \cdot (\boldsymbol{s}_1 \times \boldsymbol{s}_2)]_y = -i[\boldsymbol{s}_1, \boldsymbol{D}_{12} \cdot (\boldsymbol{s}_1 \times \boldsymbol{s}_2)]_y = 0 \tag{6.10}$$

$$-i[\boldsymbol{s}_1, \boldsymbol{D}_{14} \cdot (\boldsymbol{s}_1 \times \boldsymbol{s}_4)]_x = -2D'_z s_{4x} \tag{6.11}$$

$$-i[\boldsymbol{s}_1, \boldsymbol{D}_{14} \cdot (\boldsymbol{s}_1 \times \boldsymbol{s}_4)]_y = -2D'_z s_{4y} \tag{6.12}$$

$$-i[\boldsymbol{s}_4, \boldsymbol{D}_{14} \cdot (\boldsymbol{s}_1 \times \boldsymbol{s}_4)]_x = -2D'_z s_{1x} \tag{6.13}$$

$$-i[\boldsymbol{s}_4, \boldsymbol{D}_{14} \cdot (\boldsymbol{s}_1 \times \boldsymbol{s}_4)]_y = -2D'_z s_{1y}. \tag{6.14}$$

Therefore, while terms (6.11) to (6.14) must be added to the equation of motion when considering the sublattice pair 1 and 4, no additional term needs to be added for $s_1 s_2$ pair.

Solving the new equation of motion, for the F mode resonance, the following two resonant frequencies are obtained.

$$\omega_{F12} = \omega_1 \tag{6.15}$$

$$\omega_{F14} = \sqrt{\omega_1^2 + 4D_z'^2} \tag{6.16}$$

Where ω_1 is the resonant frequency in equation (2.29) obtained from the two-sublattice approximation.

Using the values of the F mode resonance listed in Table6.1, the calculated value of D'_z in the temperature range from 20 K to 70 K lies inside 26 GHz to 45 GHz in the dimension of frequency, or 0.86 cm^{-1} to 1.5 cm^{-1} in the dimension of the wavenumber. According to Koshizuka *et al.*, the Dzyaloshinskii constant in orthoferrites are roughly 1 cm^{-1} [51], which is very close to the value of D'_z obtained here. Figure6.16 shows the calculated value of split with various ω_{F12} using the equations (6.15) and (6.16). Comparing with the actual experimental result plotted in Fig.6.16, the splitting calculated with value of the Dzyaloshinskii

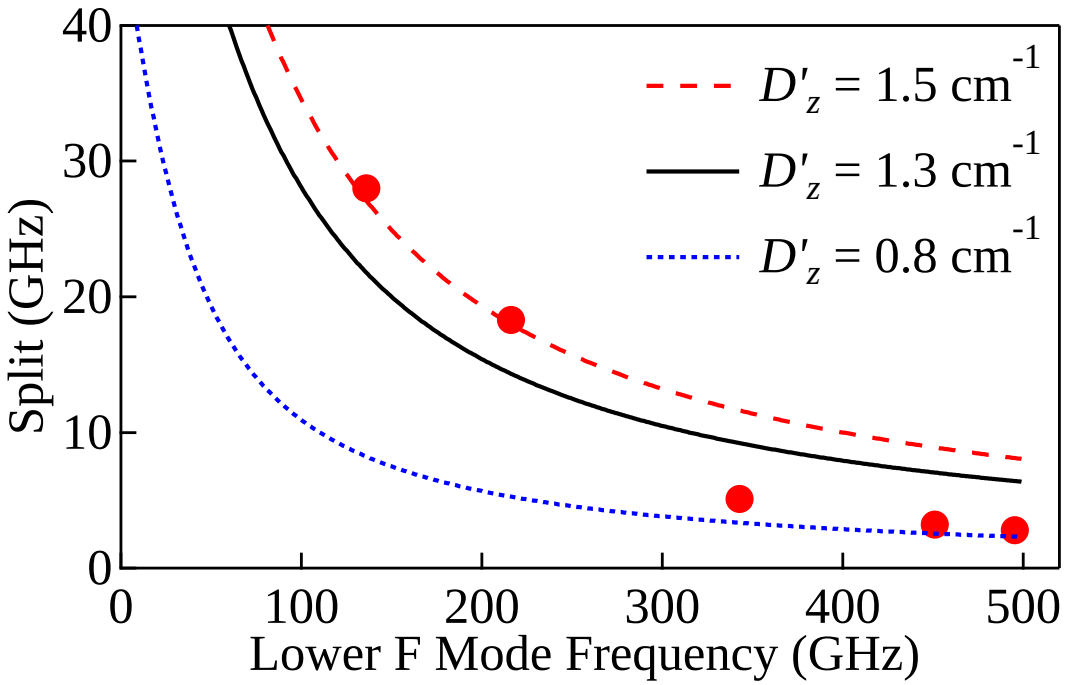

FIG. 6.16 The calculated value of the F mode resonance splitting versus ω_{F12} for values $D'_z = 0.8\ \mathrm{cm}^{-1}$, $1.3\ \mathrm{cm}^{-1}$ and $1.5\ \mathrm{cm}^{-1}$. The closed circle markers show the splitting versus the lower F mode peak frequency obtained in $ErFeO_3$ at 20 K, 30 K, 50 K, 70 K, and 80 K.

constant $D'_z = 1.3\ \mathrm{cm}^{-1}$ shows good agreement with the frequency dependence (and temperature dependence) of the splitting. Thus, it was confirmed that this splitting mechanism offers reasonable explanation on the splitting of the F mode resonance and the beating observed in the first several hundred picosecond in the temporal waveforms.

The splitting mechanism introduced here is not peculiar to the F mode resonance and similar splitting can be expected in the AF mode. However, as shown before in Fig.5.15, AF mode resonance in $ErFeO_3$ is higher compared to the F mode frequency. Since the splitting due to the Dzyaloshinskii-Moriya interaction decreases as the resonant frequency increases, such splitting of AF mode with roughly 0.8 THz resonant frequency may be hidden inside the line width of the AF mode.

Application of the same argument on Γ_1 phase (low temperature phase in $DyFeO_3$) yields frequencies

$$\omega_{12} = \sqrt{\omega^2 + 4D_y^2} \tag{6.17}$$

$$\omega_{14} = \sqrt{\omega^2 + 4D_y'^2} \tag{6.18}$$

Since D_y and D_y' are expected to take similar value, the splitting of the frequency may become nearly zero. Thus, the fact that no splitting was observed with $DyFeO_3$ low temperature phase does not contradict with the proposed splitting mechanism.

In the Γ_4 phase, the splitting of the resonance modes due to the Dzyaloshinskii-Moriya interaction are

$$\omega_{12} = \sqrt{\omega^2 + 4D_x^2} \tag{6.19}$$

$$\omega_{14} = \omega \tag{6.20}$$

Since D_x may be as large as D_z, it may be possible to observe similar splitting in the Γ_4 phase. However, this splitting can be resolved if the resonance mode has sufficiently long lifetime and sufficiently low resonant frequency, and lack of such characteristics would obscure the splitting.

To summarize, the newly discovered splitting of F mode resonance mode was explained by splitting mechanism owing to the Dzyaloshinskii-Moriya interaction. The magnitude of the splitting and the temperature dependence of the splitting can be reproduced to a good agreement with the experimental result. The reason why such splitting was never reported in the past researches on magnetic resonance may be due to the spatial dependence of the resonant frequency rising from factors such as crystal defects, since the spatial resolution of traditional magnetic resonance experiment is limited by the diffraction limit of the resonant frequency ($\lambda \sim$1 mm).

6.2.2 Other Characteristic Behaviors

Amplitude Increase of the Faraday Rotation Signal

Another characteristic behavior observed in this experiment is the sudden increase of the Faraday rotation amplitude occurring several hundred picosecond after the THz pulse excitation. In order to see what is happening in this time region, Fourier spectra with two types of time windows are shown (Fig.6.17). Here, the temperal waveform obtained by 120 kV/cm THz pulse at 30 K is used. In the temporal region before amplitude increase occurs, lower branch of the split F mode resonance is predominant although higher branch F mode also

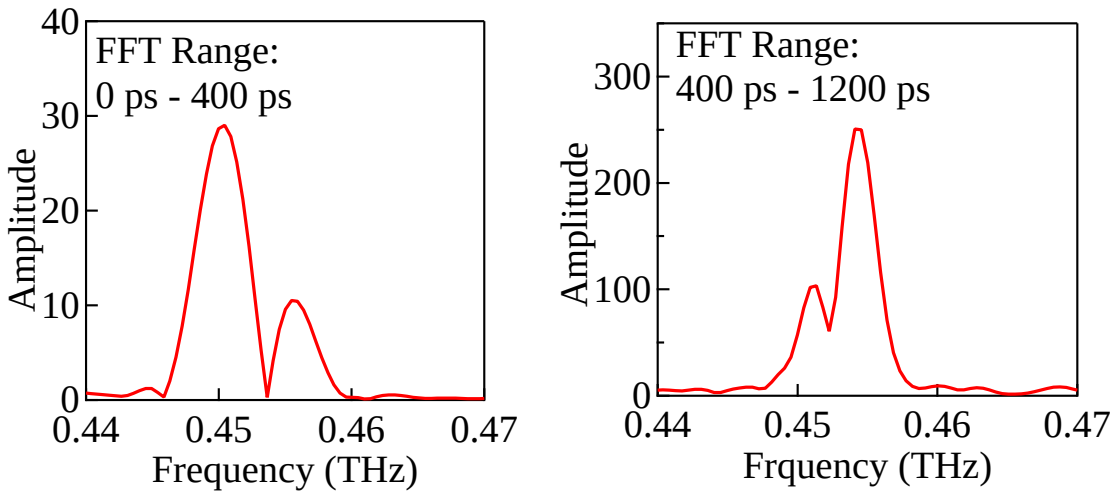

FIG. 6.17 The Fourier spectra obtained in $ErFeO_3$ at 30 K, 120 kV/cm THz pulse with different time windows. FFT range refers to the time shown in Fig.6.13(a).

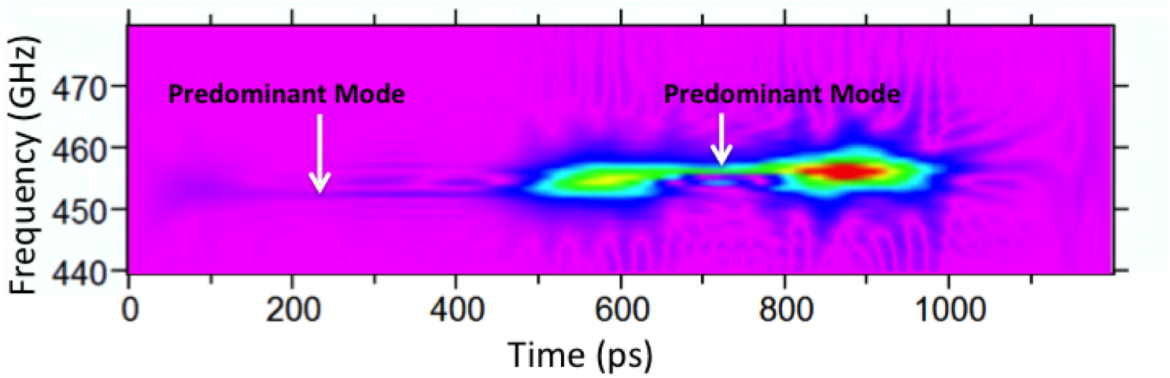

FIG. 6.18 Time-frquency distribution image of the Faraday rotation signals obtained in $ErFeO_3$ at 30 K.

exists to some extent. In the region including the large amplitude oscillation, the spectrum shows that the balance of the two F mode branches are reversed and in this temporal region, higher branch becomes predominant. The time-frequency analysis in Fig.6.18 also show similar time development. Soon after the THz excitation at 0 ps, the lower branch F mode resonance is shown to be the predominant mode. Starting from 600 ps, the predominant oscillation switches into the higher branch F mode.

These result suggests that two split F mode resonances couple to each other and transfer energy from one another. At first, the lower branch mode is strongly excited and at the same time, higher branch mode is excited somewhat weakly. As the time passes, the energy

stocked by the lower branch starts to flow into the higher branch and the high frequency F mode amplitude starts to grow. Finally, at t =600 ps, most of the energy in the low frequency mode is transferred to the higher mode, resulting in switching of the predominant mode. Comparing the time-frequency distribution with the temporal waveform in Fig.6.13(a), the large amplitude region corresponds to the time where the predominant mode switches from the lower branch to the higher branch. Thus, the amplitude increase in the Faraday rotation signal may be the outcome of the coupled oscillation of the two split F mode resonance.

Strong Excitation Effects

As described in Fig.6.19(a), the behaviors such as the beating structure and the amplitude increase of the Faraday rotation signal did not show significant dependence on the incident THz amplitude. However, the Fourier spectra in Fig.6.19(b) show significantly nonlinear THz pulse amplitude dependence which seems to be the result of strong excitation. When the F mode is excited by a THz pulse with an peak amplitude of 120 kV/cm, two split peaks mentioned earlier is observed. On the other hand, when excited by a THz pulse with 230 kV/cm peak amplitude, a broad spectral component with numerous peaks are obtained. If we look at the spectra with two kinds of time windows shown in Fig.6.20, it can be seen that this strong excitation effect does not show up near the time origin. In the temporal region of about 400 ps to 1200 ps after the THz excitation (Fig.6.20), the Fourier spectra show distinctive difference. This means that this strong excitation effect occurs several hundred picosecond after the THz excitation. Figure6.21 shows the result of the time-frequency analysis of the spin dynamics induced with 230 kV/cm peak amplitude THz pulse. Unlike in Fig.6.18, around 600 ps, a widely spread frequency component is observed. This component spreads from about 380 GHz to 500 GHz and temporally localized at 600 ps to 700 ps. This localized broad component is the cause of the broad spectra in Fig.6.19(b).

It was mentioned before that the switching of the predominant mode between the lower F mode and the higher F mode occurs at around 600 ps and this coincides with the temporal region where this broad component is localized at. What this implies is that the broad spectral component can only be generated when certain level of amplitude of the both split F mode oscillations coexist. Therefore, the localized broad spectral component can be interpreted to be generated by the coupling between the two modes of F mode resonance that are presumed

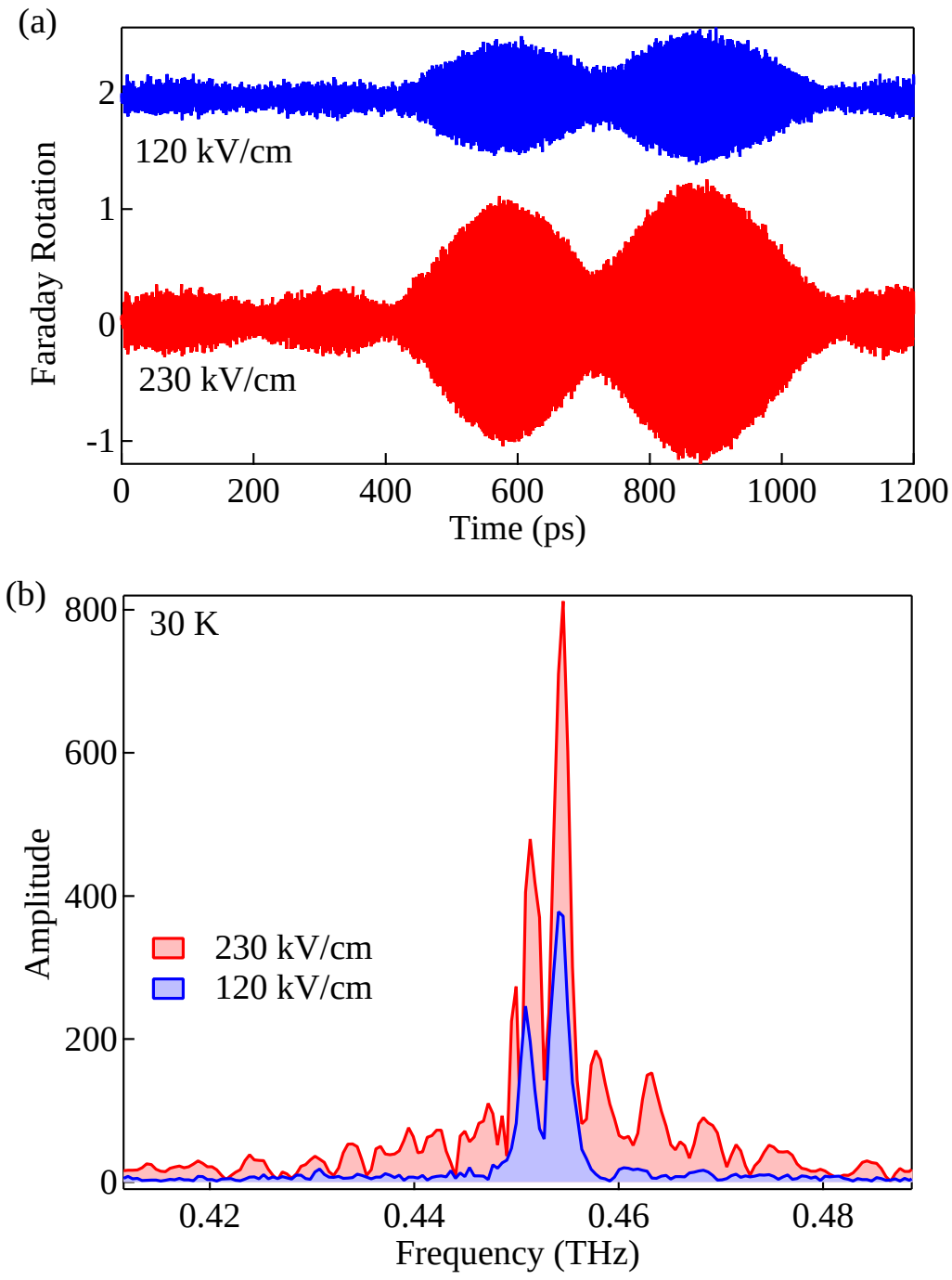

FIG. 6.19 (a) The time dependent THz induced Faraday rotation signal obtained in $ErFeO_3$ at 30 K with THz peak amplitude of 120 kV/cm and 230 kV/cm. (b) The Fourier spectra obtained from the temporal waveforms in (a).

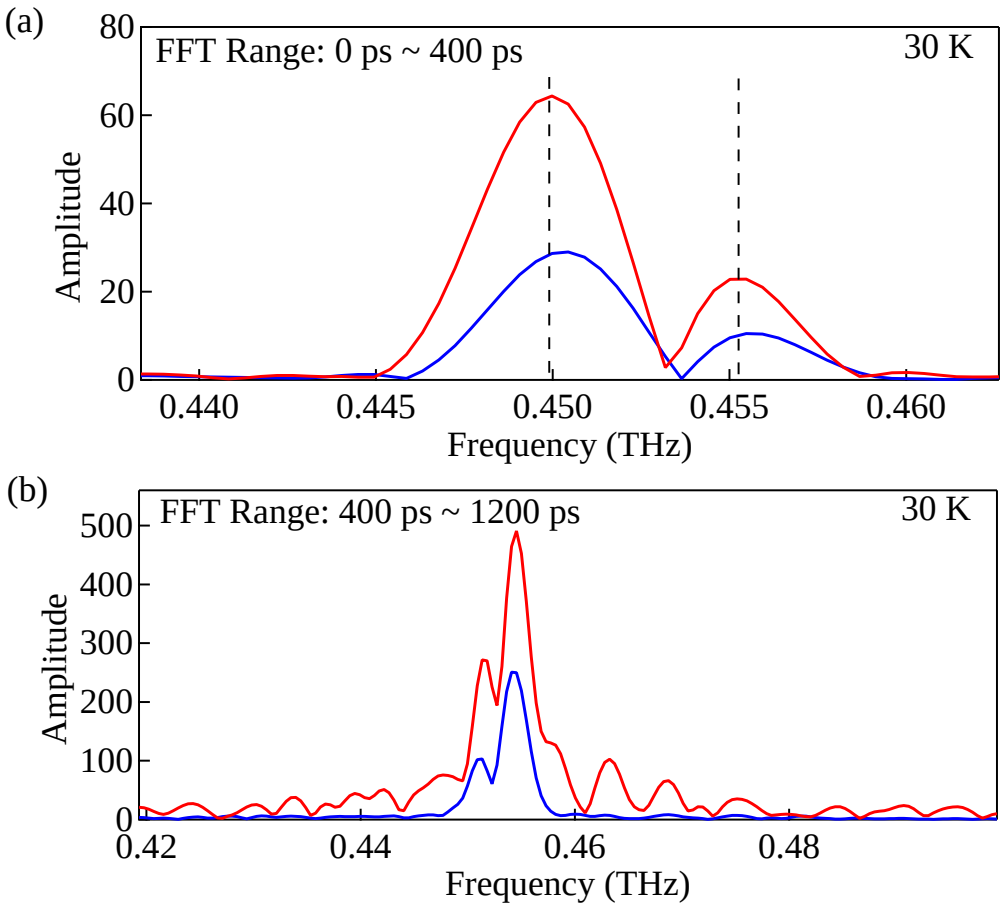

FIG. 6.20 Fourier spectra of the data in Fig.6.19(a) with two kind of time window. (a) Spectra obtained with Fourier transformation range from 0 ps to 400 ps. (b)Spectra with Fourier transformation range from 400 ps to 1200 ps.

to be split by the Dzyaloshinskii-Moriya interaction.

The dependence of this broad component on the THz peak amplitude is actually complicated and not monotonous. The spectra in Fig.6.22(a) shows that when the peak THz amplitude is small (120 kV/cm and 190 kV/cm), no broad components can be confirmed. In the higher THz amplitude condition (205-230 kV/cm), the broad component appears. However, when the THz pulse amplitude is increased to 240 kV/cm, the broad component suddenly disappears. The peak amplitudes in the spectra also show non-monotonous THz amplitude dependence (Fig.6.22(b)). A decrease in the peak is observed when the THz amplitude is raised from 190 kV/cm to 205 kV/cm. Because the broad component starts to appear from 205 kV/cm excitation, this temporally localized broad component is considered to be generated at the expense of decrease of the F mode resonance peak amplitude. Figure6.22(c) shows the

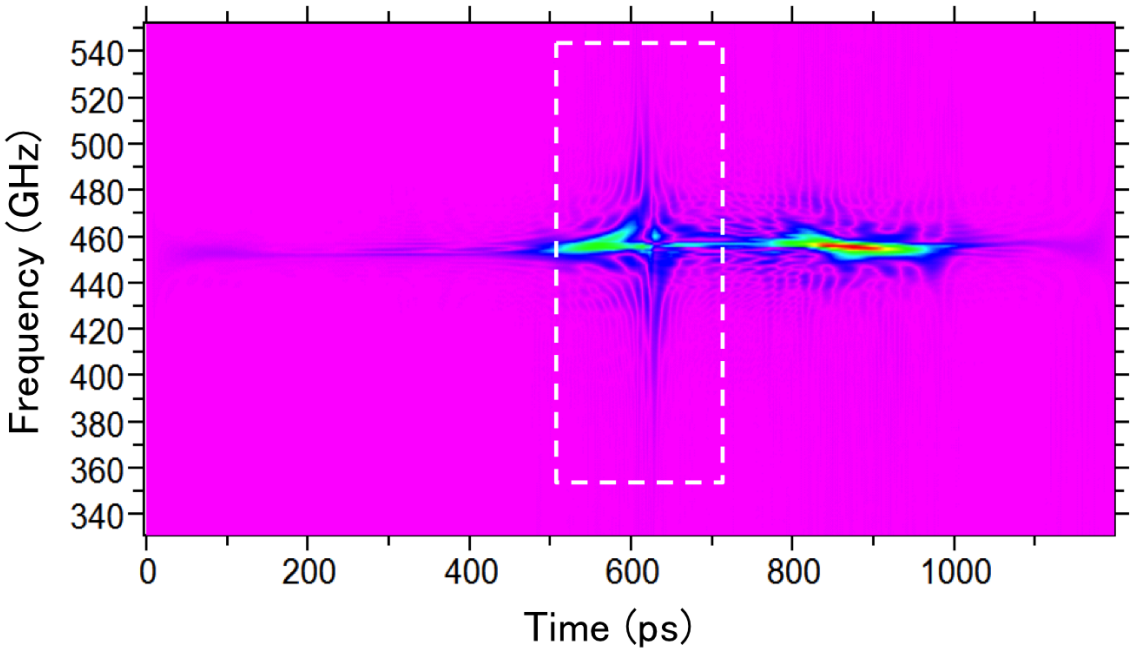

FIG. 6.21 Time-frequency distribution image obtained in $ErFeO_3$ at 30 K with THz excitation with 230 kV/cm peak amplitude.

total amplitude of the spectra in Fig.6.22(a) calculated by integrating the amplitude over wide frequency range (from 0.3 THz to 0.6 THz). It can be observed from the figure that the total amplitude of the spectra shows sudden increase at 205 kV/cm which again corresponds to the appearance of the broad spectral component. Further increase of the THz amplitude do not change the total amplitude until THz amplitude reaches 240 kV/cm and the broad component disappears. At 240 kV/cm, the total amplitude drops to the value which matches with the linear extrapolation of the values in 120 kV/cm and 190 kV/cm. Therefore, the non monotonous dependence on the THz amplitude seems to have its origin in the temporally localized broad spectral component. This assumption is also supported by the Fourier transformation within 0 ps to 400 ps with various THz amplitude where the peak amplitude of the obtained spectra show monotonic increase as the incident THz amplitude increases (Fig.6.23). In addition, the THz peak amplitude dependence of the spectral peak amplitude in Fig.6.23 seems to show slight nonlinearity. For example, the peak amplitude of approximately 70 obtained with 240 kV/cm is more than twice as large as the value of about 29 obtained with 120 kV/cm THz pulse. Since the deviation from the linear dependence at this level is subtle, experiments with much stronger THz pulse is required for judging the significance of this nonlinear be-

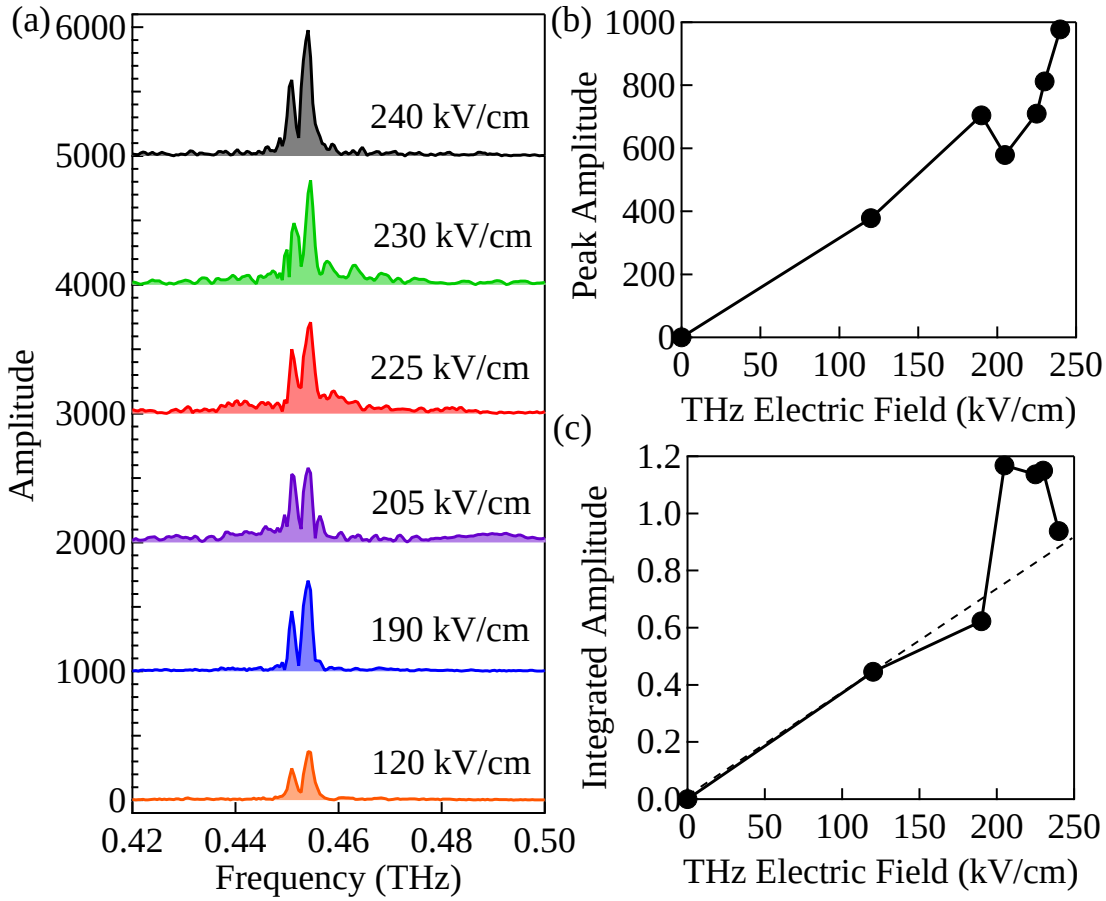

FIG. 6.22 (a) The Fourier spectra of the Faraday rotation in $ErFeO_3$ at 30 K with various THz amplitude. The Fourier transformation range was from 0 ps to 1200 ps. (b) The plot of the peak amplitude in (a). (c) Total amplitude of the peaks in (a) calculated by integrating the spectra over wide frequency range from 0.3 THz to 0.6 THz.

havior. Also, stronger THz pulse excitation may provide additional insights on the detailed generation condition of the temporally localized broad spectral component.

Looking once again at Fig.6.23(a), when we compare the spectra with 240 kV/cm THz pulse and 120 kV/cm THz pulse, slight red shift of the F mode peaks can be noticed. The amount of the observed shift is roughly 0.5 GHz, approximately 1/1000 of the resonant frequency. Comparison of the two temporal waveforms are shown in Fig.6.24. Soon after the THz excitation occurs, the phase of the oscillation in both cases seem to be equivalent. However, as the time passes, the phase in the two waveforms start to deviate from one another. At around 300 ps, phase shift of approximately 0.26 ps is observed and the oscillation induced by 240 kV/cm THz pulse starts to lag behind. Since the oscillation period of the F mode at

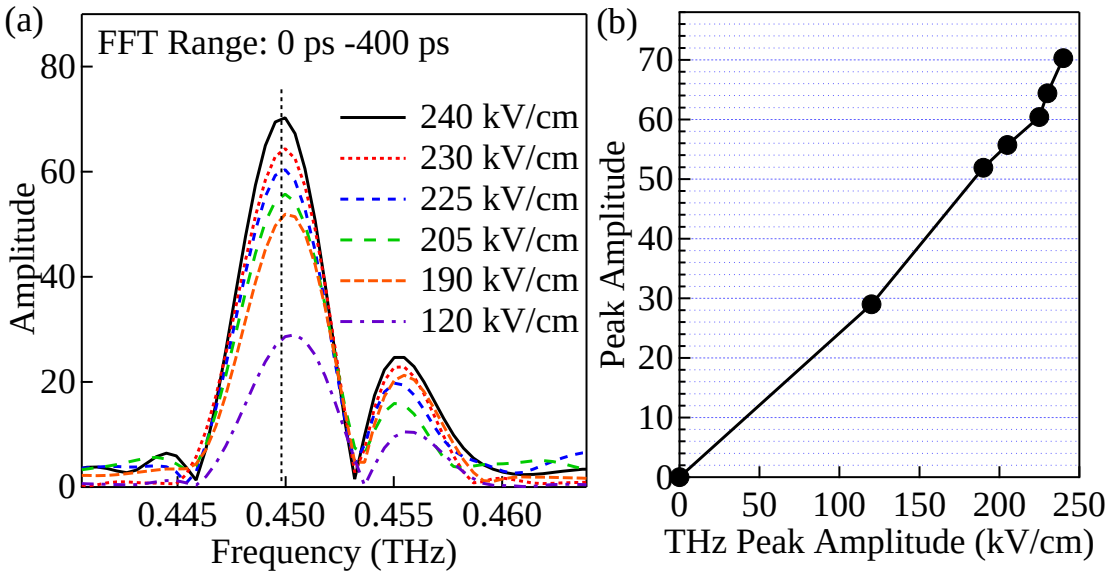

FIG. 6.23 (a) The F mode spectra in $ErFeO_3$ at 30 K with various THz amplitude. The Fourier transform range was set from 0 ps to 400 ps so that the effect of the broad spectral component can be excluded. (b) The plot of the peak amplitude of the peaks shown in (a).

30 K is about 2.2 ps, the spins oscillates for about 130 times during 300 ps. As previously stated, since the observed frequency shift is 1/1000 of the frequency, expected amount of the phase shift after 130 oscillations is roughly 0.15 which is equivalent to 0.33 ps in this case. Considering the temporal resolution of this measurement (0.13 ps/step), the expected phase shift and the observed shift agree reasonably well. At around 900 ps after the THz excitation, the shift of the oscillation becomes greater (roughly 0.7 ps). Thus, the temporal waveforms in Fig.6.24 also support the validity of the red shift of the F mode resonant frequency caused by a strong THz pulse.

The observed red shift can be ascribed to the anharmonic nature of the Fe^{3+} spin potentials. Unlike the real magnetic field, the effective magnetic field applied to the spins are actually dependent on the orientation of the spins. In the low amplitude oscillations, such differences were very small and negligible. However, as the spins are excited largely out of the equilibrium, this difference starts to become non-negligible and become observable as frequency shift. In this experiment, the angle of the spin tipping due to THz excitation is estimated to be about 0.02 rad (see Appendix). This frequency shift can also be qualitatively understood by heating due to THz absorption. However, using the heat capacity of 8 $JK^{-1}mol^{-1}$ in $ErFeO_3$

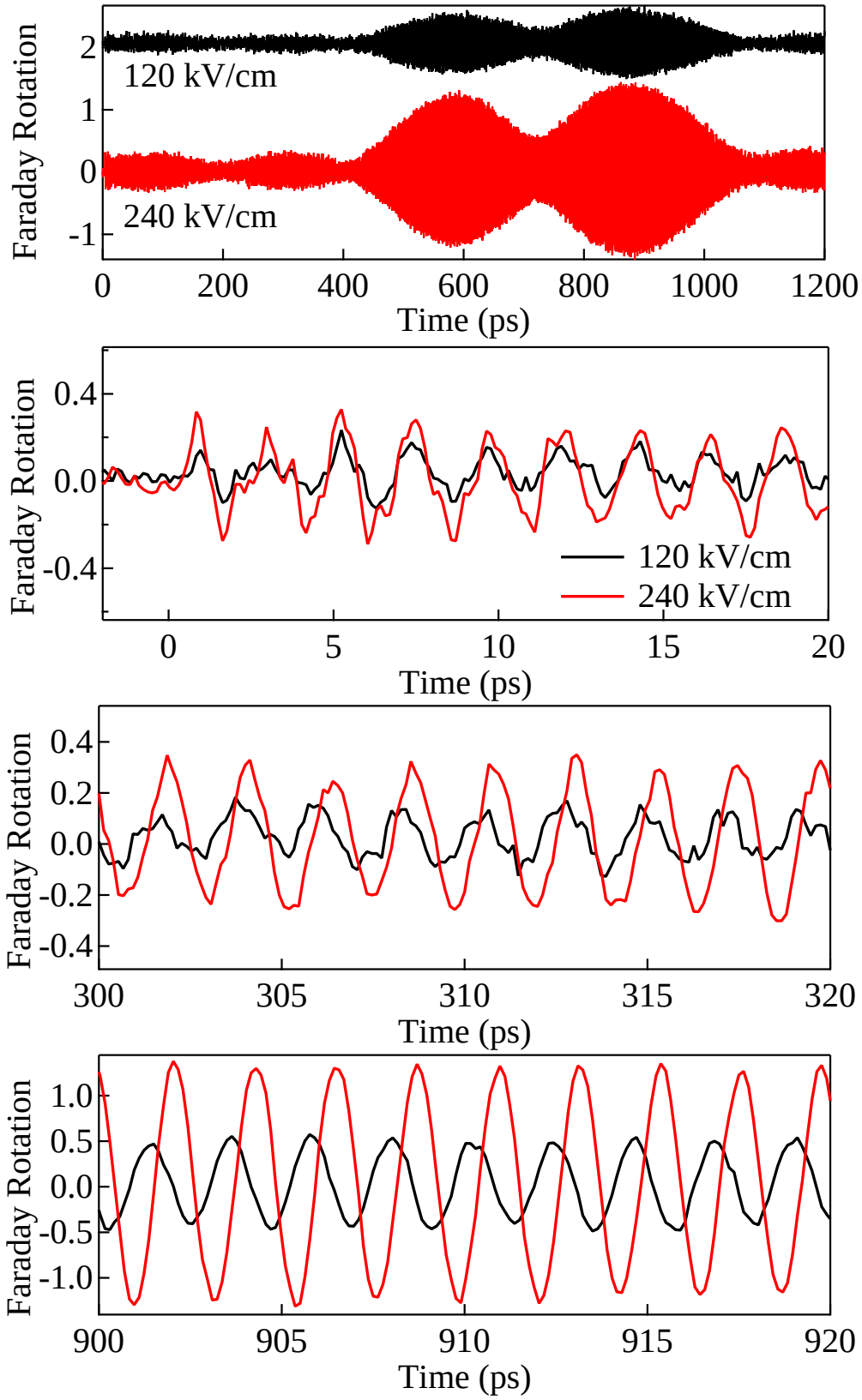

FIG. 6.24 The time dependent THz induced Faraday rotation signal in $ErFeO_3$ at 30 K obtained with THz amplitude of 240 kV/cm and 120 kV/cm.

at 30 K, it can be estimated that the temperature increase caused by THz absorption is 0.025 K at most. As previously mentioned, F mode frequency shift in $ErFeO_3$ in this temperature range is 4.47 GHz/K. Therefore, even if all of the THz pulse energy is absorbed, which is unlikely to happen, the resulting frequency shift is 0.1 GHz. This is smaller than the observed shift and therefore, the heating by THz absorption cannot be the main cause of the observed frequency shift.

Since larger frequency shift is predicted when the spins are deflected out of the equilibrium position much largely, measurement with much stronger THz pulse may result in more drastic frequency shift and detailed information on the potential of the spins may be obtained.

Chapter7

Conclusion

In this thesis, pulsed THz wave induced ultrafast spin dynamics in canted antiferromagnet $RFeO_3$ were studied. $RFeO_3$, which is also called orthoferrites are known to possess two antiferromagnetic resonance modes in the sub-THz region, namely F mode and AF mode resonance, and the dynamics of these two resonance modes were observed.

The THz time domain spectroscopy experiment on $YFeO_3$ revealed that both branches of the antiferromagnetic resonance can be excited with the magnetic field component of the THz pulse in an analogous manner to the THz excitation of ferromagnetic resonance reported prior to this research [31]. The excited spin precessions were observed through magnetic dipole radiation which is also known as the free induction decay (FID) signals. By performing a double pulse excitation of the magnetic resonance, coherent control of the spin precession was demonstrated. The result of this coherent control experiment confirmed for the first time, that the energy of the incident THz pulse is stored in the precessing spin system and that this energy can be re-collected by introducing additional THz pulse at appropriate timing.

Using $ErFeO_3$ and $DyFeO_3$ as the samples, phase transition known as the spin reorientation transition was studied with the THz TDS method. In the rotational type reorientation present in $ErFeO_3$, it was found that polarization change of the emitted FID, and the change in the frequency of the precession occurs owing to the spin reorientation. The abrupt type spin reorientation in $DyFeO_3$ was also observed as the change in the frequency of the F and AF mode. In addition, the external static magnetic field induced reorientation temperature shift was studied with $DyFeO_3$. The result of this experiment showed that large frequency shift of the AF mode resonance occurs with application of a fairly weak magnetic field. In addi-

tion, by exploiting the temperature dependence of the antiferromagnetic resonant frequency, ultrafast heating effect induced by a pumping visible pulse was observed. As a result, the time constant of the ultrafast heating differed largely between $ErFeO_3$ and $DyFeO_3$. Such difference was interpreted as the difference in the electron-phonon coupling of Er^{3+} $4f$ electrons and Dy^{3+} $4f$ electrons. Thus, it was shown that the visible pump THz probe experiment is effective for observing ultrafast heating of the spin systems and informations on electron-phonon coupling of the rare-earth $4f$ electrons can be obtained.

Finally, high intensity THz pulse with electric field amplitude up to 400 kV/cm was used to excite the magnetic resonances in $DyFeO_3$ and $ErFeO_3$ and the spin dynamics were observed via Faraday rotation signal of the visible laser pulses. In $DyFeO_3$, the reorientation temperature obtained with this method was slightly lower than that obtained with the THz-TDS measurement. One possible explanation for this mismatch is that the incident THz magnetic field caused the reorientation temperature to shift. Excitation with lower THz amplitude resulted in reappearance of the AF mode peak which implies the increase of reorientation temperature, and therefore supports the interpretation that the incident THz magnetic field shifts the reorientation temperature. The experimental result with $ErFeO_3$ sample in the low temperature spin configuration revealed the existence of the splitting of the F mode resonant frequency which has never been reported before. In this thesis, a novel splitting mechanism originating from the Dzyaloshinskii-Moriya interaction, which does not appear in the frequently used two-sublattice model, was proposed. It was shown that the magnitude of the splitting and its temperature dependence can be reproduced reasonably well with this theoretical model. In addition, several peculiar behaviors such as sudden increase of the precession amplitude several hundred picosecond after the THz excitation, and generation of temporally localized broad spectral component were experimentally observed. While further detailed analyses are required, these behaviors seem to be related with the previously explained splitting of the F mode resonant frequency. Also, slightly nonlinear THz pulse amplitude dependence of the precession amplitude and small red shift of the F mode resonance peak were observed as a result of strong excitation of the spins by THz magnetic field component. This red shift is much larger than the frequency shift which is expected from the heating due to THz absorption, and therefore can be interpreted as anharmonicity of the spin dynamics.

Table7.1 Comparison of the spin excitation methods

Methods	Ultrafast Excitation	Time Domain Observation	Heat Generation	Spectral Resolution
THz Pulse	Yes	Yes	Negligible	Low
CW Source	No	No	Negligible	High
Visible Pulse	Yes	Yes	Non- Negligible	Low

Table7.2 Comparison of the probing methods

Methods	Sample Thickness	Observable Dynamics ($\boldsymbol{k} \parallel z$)	S/N Ratio	Spatial Resolution
FID	1mm	ΔM_x, ΔM_y	High	1 mm - 4 mm
Faraday Rotation	100 μm	ΔM_z	Low	30 μm

The features of the spin excitation with THz pulse are listed in Table7.1 along with the features of other techniques such as CW source (BWO) and visible pulse excitation methods. Major advantages using THz pulses are the ability to excite spin precession in sub-picosecond time scale and the ability to realize time domain visualization of the spin dynamics. Owing to these advantages, experiments described in this research such as the double pulse coherent control and observation of photoinduced ultrafast heating were realized. Such ultrafast excitation and real-time domain observation cannot be achieved with the spectroscopy using the CW source. Although ultrafast spin excitation and time domain observation are also possible using excitation with femtosecond visible laser, as we have seen in chapter 5, introduction of visible pumping pulse results in generation of non-negligible amount of heat. Thus, the excitation method employing the visible laser is not suitable for the purpose of precise investigation on the normal mode characteristics, especially when a temperature dependent behavior exists. In addition, as it was shown in Figs.4.1 and 4.3, internal reflection of the incident THz pulse at the sample surface can be temporally separated and the fringes in the transmission spectra can be removed. Such data processing technique cannot be used with a monochromatic source and this is also one of the advantage the THz pulse excitation method possesses.

One aspect where excitation with THz pulse is less advantageous compared to the CW source is its spectral resolution. Since the CW oscillator used in Ref. [49] is highly monochromatic, the spectral resolution is roughly 0.03 GHz. On the other hand, in the time domain measurement, the spectral resolution is determined by the length of the temporal data. In most measurement, the length of data was shorter than 100 ps and in such cases, the spectral resolution can only be roughly 10 GHz or larger. In the experiment shown in chapter 6 where the length of the obtained data reached 1 ns, the spectra can be resolved to roughly 1 GHz. However, it is worth noting that the degradation of the spectral resolution in time domain measurement due to a short time window can be suppressed by extrapolating the temporal data with zeros [78, 79]. In addition, since curve fitting of an exponentially decaying oscillation can easily be performed in the temporal waveforms even when the length of the data is not sufficiently long, in the fairly simple cases where the number of the resonance mode and their frequencies are already known, the lack of high spectral resolution may not become a

critical issue.

The characteristics of the two detection methods of the spin dynamics used in this research, namely, FID emission (in THz-TDS) and Faraday rotation, are listed in Table7.2. One significant difference between the two methods is the optimum thickness of the samples. In the TDS measurement, samples with thickness varying from 0.1 mm to about 4 mm were tested and sample thickness of about 1 mm was found to be preferable in order to obtain enough FID emission. Although it is possible to measure the FID signal with 0.1 mm thick samples at room temperature, in samples such as $ErFeO_3$ where the oscillator strength of the resonance decreases in the vicinity of the spin reorientation transition, it becomes increasingly difficult to observe the FID emission. On the other hand, when the sample thickness gets larger, the resonant absorption becomes too large and accurate absorption spectra can no longer be obtained. In the method using the Faraday rotation of the transmitted visible probe pulses, the sample thickness cannot be large. Since the absorption of the orthoferrites at λ =800 nm is approximately 50 cm^{-1} [71], the sample thickness cannot exceed 200 μm. In this research, the samples used in these experiments were roughly 100 μm thick. Considering the amplitude of the oscillation obtained with this method, it seems possible to apply this method on sample as thin as 10 μm. Another important difference is the direction of the observable magnetization dynamics. Presupposing that the FID emission or the visible probe pulse propagates along the z axis, the FID emission reflects the magnetization dynamics along the x and y axis, while the visible Faraday rotation shows the magnetization dynamics along the z axis. Therefore, these two methods can be used as a complimentary approach to one another. Also, in this research the FID detection method was confirmed to be applicable with THz pulse obtained from Ti:Sapphire oscillator which possess high signal to noise ratio. In this research, the detection with Faraday rotation was only confirmed with THz pulse generated from 1 kHz Ti:Sapphire regenerative amplifier. Thus, at this moment of time, higher S/N ratio is guaranteed with the FID method. However, there is a possibility that Faraday rotation can be measured with the oscillator system and in that case, the S/N ratio of the two methods will no longer show significant difference. Lastly, the spatial resolution in FID method is lower compared to that using visible Faraday rotation. This is because the spatial resolution in FID experiment is limited by the diffraction limit of the THz pulse, while the Faraday rotation is limited by the

diffraction limit of the visible probe pulse. To be specific, in this research, the spatial resolution with FID detection ranged from 1 mm to 4 mm, whereas the method using the Faraday rotation was roughly 30 μm. As the experiment in chapter 6 showed, owing to the high spatial resolution of the visible probe pulse, detection with the Faraday rotation suppressed the inhomogeneous effects due to spatial non-uniformity. Such robustness against the inhomogeneity has enabled observation of the undiscovered fine structure in antiferromagnetic resonance in the orthoferrites.

To sum up, in this thesis, it was shown that pulsed THz waves can be used for exciting, controlling, and observing the spin precession in canted antiferromagnet. In addition, this experimental method has shown that direct energy transfer between spins and THz pulse, spin reorientation transition, and ultrafast heating of the spin system can be observed. In the perspective of this research as an investigation on the physical properties of the orthoferrites, several new behaviors such as spin reorientation temperature increase in $DyFeO_3$ due to the THz magnetic field, splitting of the F mode resonance in $ErFeO_3$, and $ErFeO_3$ F mode frequency shift by strong THz pulse were revealed experimentally, and interpretations on these phenomena were presented. Several newly discovered behaviors such as temporally localized broad spectral component in strongly excited $ErFeO_3$ were also observed and although further detailed research is required, these phenomena seem to have occurred as a result of the coupling between the two split F mode resonances in $ErFeO_3$.

The results shown in this thesis suggest that spin excitation with much stronger THz pulse may cause drastic effects in the spin system, and further development on the THz pulse amplitude is expected in the future. Although there still is a room for improving the THz system since our system can generate only about 40 % of the world record THz amplitude using the same generation method, we still lack several orders of magnitude for the purpose of completely flipping over the spins with THz magnetic field. In order to circumvent this problem, coherent excitation of the spins with a pulse train of THz pulse may be effective. Since the simplest example of the pulse train excitation, the double pulse coherent control, has proven to be effective in this thesis, development of an efficient method for generating and controlling the periodical THz pulse train is desired. Another effective approach is to enhance THz magnetic field using metamaterials and discovery of number of interesting phenomena are to

be expected.

Also, application of the recently developed "z-polarized" THz technique where THz pulse with electrical field component in a longitudinal direction is generated by focusing a radial polarization THz pulse [80] may be an interesting topic for the THz spin excitation. In the case of spin excitation, THz magnetic field in a longitudinal direction which is expected to be generated by focusing an azimuthal polarization THz pulse may be effective. Realization of such excitation enables application of THz magnetic pulse along the longitudinal direction which is one of the limitations with the ordinary THz pulses. Combining this with the spin precession excitation covered in this thesis, three-dimensional control of spins with THz pulses may become possible.

Appendix
Magnitude Estimation of the Spin Tipping

Estimation with the Experimental Result

The static Faraday rotation of the probe pulse at room temperature was measured with (001) $ErFeO_3$ single crystal. Since the Fe^{3+} spins take Γ_4 phase configuration in this temperature region, the macroscopic magnetization aligns along the thickness direction of the (001) sample. Therefore, the amount of the static Faraday rotation obtained at room temperature can be regarded proportional to the macroscopic magnetization itself.

The static Faraday rotation signal measured with the balanced detector was about 0.02 mV (the intensities of the two probe pulses were set so that each photodetector would yield ± 0.5 mV). At low temperatures, the time dependent Faraday signal immediately after excitation with 240 kV/cm was 0.4 μV. Therefore, the amplitude of the oscillation in c axis direction with respect to the macroscopic magnetization is $0.4\times10^{-6}/0.02\times10^{-3}$ =0.02. Since $\sin\theta = \theta$ when $\theta \ll 1$, the estimated tipped angle of the macroscopic magnetization is approximately 0.02 radian. In order to realize the complete spin reversal with THz pulse, improvement of two orders of magnitude is necesssary.

Estimation with Theoretical Calculation

Rough estimation of the expected spin tipping angle can be obtained in the following calculation. When a magnetic field H is applied to the spins, the spins rotate around the magnetic field with a frequency

$$\omega = \gamma H. \tag{7.1}$$

When a THz magnetic field with time duration of Δt is applied, the spins experience tipping

with a total angle of

$$\Delta\theta = \gamma H \Delta t. \tag{7.2}$$

Substitution of the values $\gamma = 1.76 \times 10^{11}$ rad$T^{-1}s^{-1}$, $H_{THz} = 0.08$ T (equivalent to $E_{THz} =$ 240 kV/cm), and $\Delta t = 0.5$ ps yields $\Delta\theta = 0.007$ rad. Although this is slightly smaller than the value obtained from the experiment, they are in the same order of magnitude.

Reference

[1] Yun-Shik Lee, *Principles of Terahertz Science and Technology*, Springer (2008).

[2] D. H. Auston, K. P. Cheung, and P. R. Smith, Appl. Phys. Lett. **45**, 284 (1984).

[3] D. J. Cook, and R. M. Hochstrasser, Opt. Lett. **25**, 1210 (2000).

[4] T. Bartel, P. Gaal, K. Reimann, M. Woerner, and T. Elsaesser, Opt. Lett. **30**, 2805 (2005).

[5] K. Y. Kim, J. H. Glownia, A. J. Taylor and G. Rodriguez, Opt. Exp. **15**, 4577 (2007).

[6] Y. Minami, T. Kurihara, K. Yamaguchi, M. Nakajima, and T. Suemoto, Appl. Phys. Lett. **102**, 041105 (2013).

[7] J. Hebling, G. Almási, I. Kozma, and J. Kuhl, Opt. Exp. **10**, 1161 (2002).

[8] J. Hebling, K. Yeh, M. C. Hoffmann, B. Bartal, and K. A. Nelson, J. Opt. Soc. Am. B **25**, B6 (2008).

[9] H. Hirori, A. Doi, F. Blanchard, and K. Tanaka, Appl. Phys. Lett. **98**, 091106 (2011).

[10] T. Kampfrath, K. Tanaka, and K. A. Nelson, Nat. Photon. **7**, 680 (2013).

[11] G. Lampel, Phys. Rev. Lett. **20**, 491 (1968).

[12] S. A. Wolf, D. D. Awschalom, R. A. Buhrman, J. M. Daughton, S. von Molanar, M. L. Roukes, A. Y. Chtchelkanova, and D. M. Treger, Science **294**, 1488 (2001).

[13] A. V. Kimel, A. Kirilyuk, P. A. Usachev, R. V. Pisarev, A. M. Balbashov, and Th. Rasing, Nature **435**, 655 (2005).

[14] P. S. Pershan, J. P. van Der Ziel, and L. D. Malmstrom, Phys. Rev. **143**, 574 (1966).

[15] T. Satoh, Y. Terui, R. Moriya, B. A. Ivanov, K. Ando, E. Saitoh, T. Shimura, and K. Kuroda, Nature Photon. **6**, 662 (2012).

[16] R. Akimoto, K. Ando, F. Sasaki, S. Kobayashi, and T. Tani, J. Appl. Phys. **84**, 6318 (1998).

[17] E. Rozkotová, P. Němec, N. Tesařová, P. Malý, V. Novák, K. Olejník, M. Cukr, and T. Jungwirth , Appl. Phys. Lett. **93**, 232505 (2008).

[18] T. Satoh, N. P. Duong, and M. Fiebig, Phys. Rev. B **74**, 012404 (2006).

[19] F. Hansteen, A. V. Kimel, A. Kirilyuk, and Th. Rasing, Phys. Rev. B **73**, 014421 (2005).

[20] J. A. de Jong, A. V. Kimel, R.V. Pisarev, A. Kirilyuk, and Th. Rasing, Phys. Rev. B **84**, 104421 (2011).

[21] J. A. de Jong, I. Razdolski, A. M. Kalashnikova, R. V. Pisarev, A. M. Balbashov, A. Kirilyuk, Th. Rasing, and A. V. Kimel, Phys. Rev. Lett. **108**, 157601 (2012).

[22] J. Nishitani, K. Kozuki, T. Nagashima, and M. Hangyo, Appl. Phys. Lett. **96**, 221906 (2010).

[23] R. Iida, T. Satoh, T. Shimura, K. Kuroda, B. A. Ivanov, Y. Tokunaga, and Y. Tokura, Phys. Rev. B **84**, 064402 (2011).

[24] J. Nishitani, T. Nagashima, and M. Hangyo, Phys. Rev. B **85**, 174439 (2012).

[25] A. V. Kimel, B. A. Ivanov, R. V. Pisarev, P. A. Usachev, R. V. Pisarev, A. M. Balbashov, and Th. Rasing, Nat. Phys. **5**, 727 (2009).

[26] A. V. Kimel, A. Kirilyuk, and Th. Rasing, Laser & Photon. Rev. **1**, 275 (2007).

[27] T. Higuchi, N. Kanda, H. Tamaru, and M. Kuwata-Gonokami, Phys. Rev. Lett. **106**, 047401 (2011).

[28] N. Kanda, T. Higuchi, H. Shimizu, K. Konishi, K. Yoshioka, and M. Kuwata-Gonokami, Nat. Commun. **2**, 362 (2011).

[29] J. A. Gupta, R. Knobel, N. Samarth, and D. D. Awschalom, Science **292**, 2458 (2001).

[30] A. V. Kimel, A. Kirilyuk, A. Tsvetkov, R. V. Pisarev, and Th. Rasing, Nature **429**, 850 (2004).

[31] M. Nakajima, A. Namai, S. Ohkoshi, and T. Suemoto, Opt. Express **18**, 18260 (2010).

[32] A. Namai, M. Yoshikiyo, K. Yamada, S. Sakurai, T. Goto, T. Yoshida, T. Miyazaki, M. Nakajima, T. Suemoto, H. Tokoro, and S. Ohokoshi, Nature Commun. **3**, 1035 (2012).

[33] T. Gilbert, IEEE Trans. Mag. **40**, 6 (2004).

[34] M. Born and E. Wolf, *The Principle of Optics*, Cambridge University Press, London (1999).

[35] K. Sato, *Hikari to jiki* [Light and magnetism], Asakura Shoten, Tokyo (2001).

[36] P. N. Argyres, Phys. Rev. **97**, 334 (1955).

[37] H. S. Bennett, and E. A. Stern, Phys. Rev. **137**, A 448 (1965).

[38] M. Marezio, J. P. Remeika, and P. D. Dernier, Acta. Crystallogr. B **26**, 2008 (1970).

[39] K. Momma, F. Izumi, J. Appl. Cryst. **44**, 1272 (2011).

[40] A. K. Zvezdin, and V. A. Kotov, *Modern Magnetooptics and Magnetooptical Materials, Institute of Physics Publishing*, Bristol and Philadelphia (1997).

[41] D. Treves, Phs. Rev. **125**, 1843 (1962).

[42] I. Dzyaloshinsky, J. Phys. Chem. Solids **4**, 241 (1958).

[43] T. Moriya, *Magnetism I*, Eds. G. T. Rado, and H. Suhl, 85, Academic Press, New York (1963).

[44] E. F. Bertaut, *Magnetism III*, Eds. G. T. Rado, and H. Suhl, 149, Academic Press, New York (1963).

[45] G. F. Herrmann, Phys. Rev. **133**, A1334 (1964).

[46] R. L. White, J. App. Phys. **40**, 1061 (1969).

[47] T. Yamaguchi, J. Phys. Chem. Solids. **35**, 479 (1974).

[48] H. Lütgemeier, H. G. Bohn, and M. Brajczewska, J. Magn. and Magn. Mat. **21**, 289 (1980).

[49] G. V. Kozlov, S. P. Lebedev, A. A. Mukhin, A. S. Prokhorov, I. V. Fedorov, A. M. Balbashov, and I. Y. Parsegov, IEEE Trans. Magn. **29**, 3443 (1993).

[50] C. H. Tsang, R. L. White, and R. M. White, J. Appl. Phys. **49**, 6063 (1978).

[51] N. Koshizuka, and K. Hayashi, J. Phys. Soc. Jpn. **57**, 4418 (1988).

[52] A. A. Mukhin, M. Biberacher, A. Pimenov, and A. Loidl, J. Mag. Reson. **170**, 8 (2004).

[53] T. Löffler, M. Kreß, M. Thomson, T. Hahn, N. Hasegawa, and H. Roskos, Semicond. Sci. Technol. **20**, S134 (2005).

[54] H. Shen, J. Xu, A. Wu, J. Yu, Y. Liu, and L. Luo, Cryst. Res. Technol. **42**, 943 (2007).

[55] S. M. Koohpayeh, J. S. Abell, K. K. Bamzai, A. I. Bevan, D. Fort, and A. J. Williams, J. Mag. Mag. Mater. **39**, 119 (2007).

[56] K. Ohmori, Annu. Rev. Phys. Chem. **60**, 487 (2009).

[57] T. Dekorsy, W. Kütt, T. Pfeifer, and H. Kurz, Europhys. Lett. **23**, 223 (1993).

[58] M. Hase, K. Mizoguchi, H. Harima, S. Nakashima, M. Tani, K. Sakai, and M. Hangyo, Appl. Phys. Lett. **69**, 2474 (1996).

[59] M. U. Wehner, M. H. Ulm, D. S. Chemla, and M. Wegener, Phys. Rev. Lett. **80**, 1992 (1998).

[60] A. P. Heberle, J. J. Baumberg, and K. Köhler, Phys. Rev. Lett. **75**, 2598 (1995).

[61] K. Yamaguchi, M. Nakajima, and T. Suemoto, Phys. Rev. Lett. **105**, 237201 (2010).

[62] M. Nakajima, K. Yamaguchi, and T. Suemoto, Acta. Phys. Polon. A **121**, 343 (2012).

[63] T. Kampfrath, A. Sell, G. Klatt, A. Pashkin, S. Mährlein, T. Dekorsy, M. Wolf, M. Fiebig, A. Leitenstorfer, and R. Huber, Nat. Photon. **5**, 31 (2011).

[64] K. Yamaguchi, T. Kurihara, Y. Minami, M. Nakajima, and T. Suemoto, Phys. Rev. Lett. **110**, 137204 (2013).

[65] H. Horner, and C. M. Varma, Phys. Rev. Lett. **20**, 845 (1968).

[66] S. M. Shapiro, J. D. Axe, and J. P. Remeika, Phys. Rev. B **10**, 2014 (1974).

[67] I. Mikami, J. Phys. Soc. Jpn. **34**, 338 (1973).

[68] V. N. Derkachenko, A. K. Zvezdin, A. M. Kadomtseva, N. M. Kovtun, V. M. Matveev, V. A. Timofeeva, and V. A. Khokhlov, Sov. Phys. Sol. Stat. **18**, 1978 (1976).

[69] K. P. Belov, A. K. Zvezdin, A. M. Kadomtseva, and I. B. Krynetskii, Sov. Phys. JETP **40**, 980 (1975).

[70] K. P. Belov, A. M. Kadomtseva, N. M. Kovtun, V. N. Derkachenko, V. N. Melov and V. A. Khokhlov, Phys. Status Solidi A **36**, 415 (1976).

[71] D. L. Wood, J. P. Remeika, and E. D. Kolb, J. Appl. Phys. **41**, 5315 (1970).

[72] L. Cohen, Proc. IEEE (Invited Paper) **77**, 941 (1989).

[73] H. Choi, and W. J. Williams, IEEE Trans. Acoustics, Speech, and Signal Processing **37**, 862 (1989).

[74] V. E. Gusev, and O. B. Wright, Phys. Rev. B **57**, 2878 (1998).

[75] A. Ellens, H. Andres, M. L. H. ter Heerdt, R. T. Wegh, A. Meijerink, and G. Blasse, Phys. Rev. B **55**, 180 (1997).

[76] S. C. Parida, S. K. Rakshit, and Ziley Singh, J. Sol. Stat. Chem. **181**, 101 (2008).

[77] C. Kittel, Phys. Rev. **110**, 1295 (1958).

[78] P. R. Griffiths, Appl. Spectrosc. **29**, 11 (1975).

[79] R. A. Cheville, and D. Grischkowsky, Opt. Lett. **20**, 1646 (1995).

[80] Y. Minami, T. Kurihara, K. Yamaguchi, M. Nakajima, and T. Suemoto, Appl. Phys. Lett. **102**, 151106 (2013).

Related Publications

1. K. Yamaguchi, M. Nakajima, T. Suemoto
   ”Coherent Control of Spin Precession Motion with Impulsive Magnetic Fields of Half-Cycle Terahertz Radiation”
   Physical Review Letters **105**, 237201-1 - 237201-4 (2010).

2. M. Nakajima, K. Yamaguchi, and T. Suemoto
   ”Ultrafast Coherent Control of Spin Precession Motion by Terahertz Magnetic Pulses”
   Acta Physica Polonica A **121**, 343-346 (2012).

3. K. Yamaguchi, T. Kurihara, Y. Minami, M. Nakajima, and T. Suemoto
   ”Terahertz Time-Domain Observation of Spin Reorientation in Orthoferrite $ErFe_3$ through Magnetic Free Induction Decay”
   Physical Review Letters **110**, 137204-1 - 137204-5 (2013).

Acknowledgement

I am deeply grateful to Professor T. Suemoto for his instructions and enormous support throughout the past 5 years.

I would also like to thank Dr. M. Nakajima (associate professor at Chiba University, research associate at Suemoto laboratory until March 2012), and Dr. H. Watanabe (research associate as of december 2013) for their supports and advices throughout the research.

I am particularly grateful to Professor T. Kato (Division of Condensed Matter Theory, ISSP, The University of Toyko) for his insightful comments during the theoretical discussions. I also appreciate Mr. T. Kitazawa (Materials Synthesis Section, ISSP, The University of Tokyo) for his support during the growth of the single crystal samples.

I would also like to show my appreciations to the members of Suemoto Laboratory: Dr. Y. Minami, Dr. R. Fukaya, Mr. H. Nakao, Mr. K. Terakawa, Mr. H. Ebihara, Mr. A. Asahara, Mr. S. Sakaki, Mr. T. Kurihara, Mr. S. Ishige, Mr. R. Takei, Mr. T. Kawasaki, Mr. M. Hashimoto, Mr. K. Nakamura, and Mr. M. Takeda.

Finally, I would like to thank my parents for their constant and enormous supports.